ผลเฉลยเชิงตัวเลขของปัญหา 4:1 คอนแทรกชันสำหรับการไหลวิสโคอิลาสติก ซึ่งมีผลกระทบจากการลื่นไถล

นางสาวนวลักษณ์ ทองจับ

วิทยานิพนธ์นี้เป็นส่วนหนึ่งของการศึกษาตามหลักสูตรปริญญาวิทยาศาสตรดุษฎีบัณฑิต
สาขาวิชาคณิตศาสตร์ประยุกต์และวิทยาการคณนา ภาควิชาคณิตศาสตร์และวิทยาการคอมพิวเตอร์
คณะวิทยาศาสตร์ จุฬาลงกรณ์มหาวิทยาลัย
ปีการศึกษา 2557

NUMERICAL SOLUTION OF 4:1 CONTRACTION PROBLEM FOR VISCOELASTRIC FLOW WITH SLIP EFFECT

Miss Nawalax Thongjub

A Dissertation Submitted in Partial Fulfillment of the Requirements
for the Degree of Doctor of Philosophy Program in Applied Mathematics and Computational Science
Department of Mathematics and Computer Science
Faculty of Science
Chulalongkorn University
Academic Year 2014

Thesis Title	NUMERICAL SOLUTION OF 4:1 CONTRACTION PROBLEM FOR VISCOELASTRIC FLOW WITH SLIP EFFECT
By	Miss Nawalax Thongjub
Field of Study	Applied Mathematics and Computational Science
Thesis Advisor	Assistant Professor Vimolrat Ngamaramvaranggul, Ph.D.
Thesis Co-Advisor	Bumroong Puangkird, Ph.D.

Accepted by the Faculty of Science, Chulalongkorn University in Partial Fulfillment of the Requirements for the Doctoral Degree

.....Dean of the Faculty of Science
(Professor Supot Hannongbua, Dr.rer.nat.)

THESIS COMMITTEE

.....Chairman
(Associate Professor Pornchai Satravaha, Ph.D.)

.....Thesis Advisor
(Assistant Professor Vimolrat Ngamaramvaranggul, Ph.D.)

.....Thesis Co-Advisor
(Bumroong Puangkird, Ph.D.)

.....Examiner
(Assistant Professor Khamron Mekchay, Ph.D.)

.....Examiner
(Assistant Professor Krung Sinapiromsaran, Ph.D.)

.....External Examiner
(Mahosut Punpocha, Ph.D.)

นวลักษณ์ ทองจับ : ผลเฉลยเชิงตัวเลขของปัญหา 4:1 คอนแทรกชันสำหรับการไหลวิสโคอิลาสติกซึ่งมีผลกระทบจากการลื่นไถล (NUMERICAL SOLUTION OF 4:1 CONTRACTION PROBLEM FOR VISCOELASTRIC FLOW WITH SLIP EFFECT) อ.ที่ปรึกษาวิทยานิพนธ์หลัก: ผศ. ดร.วิมลรัตน์ งามอร่ามวรางกูร, อ.ที่ปรึกษาวิทยานิพนธ์ร่วม: อ.ดร.บำรุง พ่วงเกิด, 146 หน้า.

วิทยานิพนธ์นี้นำเสนอผลกระทบการลื่นไถลของปัญหา 4:1 คอนแทรกชันและผิวอิสระภายใต้เทคนิคการไหลของความเร็วขับความดันป้อนกลับ สมการเนเวียร์สโตกส์ใช้เป็นตัวแบบสำหรับของไหลชนิดนิวโตเนียนและของไหลชนิดวิสโคอิลาสติกแต่สมการองค์ประกอบถูกประยุกต์ ใช้สำหรับของไหลชนิดออลดรอย-บีเท่านั้น การศึกษาของทั้งสองกรณีให้ความสนใจกับพฤติกรรมการไหลโดยเฉพาะสำหรับ ความดัน ความเร็ว ความเค้น และทางเดินสายกระแส ผลเฉลยเชิงตัวเลขหาได้โดยวิธีไฟไนต์เอเลเมนต์เซมิอิมพิซิทเทย์เลอร์กาเลอร์คินเพรซเซอร์คอร์เรคชันยิ่งไปกว่านั้น แผนการกู้คืนสู่สภาพเกรเดียนต์ความเร็วและแผนการสายกระแส-ต้านลมเปรตอฟ/กาเลอร์คินถูกเลือกมาเพื่อทำให้ผลเฉลยที่ลู่เข้ามีความเสถียรภายใต้การไหลอัดตัวไม่ได้ที่มีอุณหภูมิคงที่สำหรับของไหลชนิดนิวโตเนียนและของไหลชนิดออลดรอย-บีทั้งที่มีและไม่มีผลกระทบจากการลื่นไถล ผลเฉลยของการไหล 4:1 คอนแทรกชันถูกหาในระบบพิกัดเชิงระนาบสำหรับมุมที่มีรูปร่างแหลมและรูปร่างโค้งกลม ในขณะที่การไหลแบบสมมาตรรอบแกนถูกเลือกสำหรับการบวมตัวจากการอัดผ่านเกลียว เกณฑ์มาตรฐานที่ใช้ในการเปรียบเทียบถูกแสดงด้วยผลลัพธ์จากวิธีไฟไนต์เอเลเมนต์เซมิอิมพิซิทเทย์เลอร์กาเลอร์คินเพรซเซอร์คอร์เรคชันเปรียบเทียบกับผลเฉลยเชิงวิเคราะห์และผลเฉลยเชิงตัวเลขที่ได้จากวิธีอื่น การเปรียบเทียบแสดงให้เห็นว่าปัญหาการจำลองทั้งสองถูกประเมินอย่างมีประสิทธิภาพด้วยการทำให้คืนสภาพป้อนกลับ ในทิศทางเดียวกันผลลัพธ์ที่แม่นยำภายใต้ความเร็วที่มีการลื่นไถลขับเคลื่อนผลที่ได้ให้เข้าใกล้ปัญหาของความเป็นจริง

ภาควิชา	คณิตศาสตร์และวิทยาการคอมพิวเตอร์	ลายมือชื่อนิสิต .....
สาขาวิชา	คณิตศาสตร์ประยุกต์และวิทยาการคณนา	ลายมือชื่อ อ.ที่ปรึกษาหลัก .....
ปีการศึกษา	2557	ลายมือชื่อ อ.ที่ปรึกษาร่วม .....

5373925223 : MAJOR APPLIED MATHEMATICS AND COMPUTATIONAL SCIENCE

KEYWORDS: SLIP / 4:1 CONTRACTION / DIE-SWELL

NAWALAX THONGJUB: NUMERICAL SOLUTION OF 4:1 CONTRACTION PROBLEM FOR VISCOELASTRIC FLOW WITH SLIP EFFECT. ADVISOR: ASST. PROF. VIMOLRAT NGAMARAMVARANGGUL, Ph.D., CO-ADVISOR: BUMROONG PUANGKIRD, Ph.D., 146 pp.

This dissertation presents the slip effect of 4:1 contraction and free surface problems under feedback pressure-driven velocity flow technique. The Navier-Stokes equations are modeled for Newtonian and viscoelastic fluids but constitutive equation is only applied for Oldroyd-B flow. The studies of both cases are attributed to flow behaviors especially for pressure, velocity, stresses and streamline paths. The numerical solutions are obtained by a semi-implicit Taylor-Galerkin pressure-correction finite element method (STGFEM). In addition, the velocity gradient recovery and the streamline-upwind Petrov/Galerkin (SUPG) schemes are chosen to stabilize the converged solutions under the two dimentional isothermal incompressible flow. For Newtonian and Oldroyd-B fluids with and without the slip effect, the solutions of 4:1 contraction flow is executed in planar system for sharp and rounded corner shapes while axisymmetric flow is opted for extrudate swell. The benchmarks are displayed with results from STGFEM versus analytical and numerical solutions. The comparisons show that these two simulation problems are evaluated with efficiency of feedback treatment. At the same direction, the accuracy results under slip velocity drive the outcomes approaching to real problems.

Department:	Mathematics and Computer Science	Student's Signature	.....
Field of Study:	Applied Mathematics and Computational Science	Advisor's Signature	.....
Academic Year:	2014	Co-Advisor's Signature	.....

ACKNOWLEDGEMENTS

I first wish to express my extremely grateful acknowledge to my advisor, Assistant Professor Dr. Vimolrat Ngamaramvaranggul for her invaluable supervision, guidance, comments, suggestions, unfailing kindness, and her patience in reading drafts and rectifying the mistake of this dissertation.

I also extend my gratitude to the co-advisor, Dr. Bumroong Puangkird of the Department of Mechanical Engineering, Faculty of Engineering, King Mongkut's Institute of Technology Ladkrabang for his kindness, suggestions, correction, and provision of some software.

I would like to thank my thesis committees, Associate Professor Dr. Pornchai Satravaha, Assistant Professor Dr. Khamron Mekchay, Assistant Professor Dr. Krung Sinapiromsaran and my thesis external examiner, Dr. Mahosut Punpocha who is at the Department of Mathematics, Faculty of Applied Science, King Mongkut's University of Technology North Bangkok for carefully reading the manuscript and significant guidance to improve this dissertation.

Moreover, I would like to thank all lecturers of the Department of Mathematics and Computer Science, Faculty of Science, Chulalongkorn University, Professor P. Nithiarasu and Professor M.F. Webster who taught me valuable knowledge from Swansea University, UK, and Dr. Javad Banaai who is a process engineer of ENI Engineering E&P Ltd., Basingstoke, UK.

Additionally, the authors would like to thank the scholarship from National Science and Technology Development Agency (NSTDA), Thailand to support PhD degree and Advanced Virtual and Intelligence Computing (AVIC) at the Department of Mathematics and Computer Science, Faculty of Science, Chulalongkorn University to sustain the advanced computer machinery.

Finally, I would like to express the deepest appreciation to my parents for all their understanding and supporting throughout the period of this PhD study, and I would like to thank my friends and those whose names are not mentioned here but greatly encouraged me until this dissertation is completed.

CONTENTS

Page

Page

LIST OF TABLES

Page

LIST OF FIGURES

Page

Page

Page

CHAPTER 1
INTRODUCTION

In this research, the content covers rheology of fluid and the numerical methods in the applications of engineering and science. Rheology is the study of flow and deformation of matter under applied forces originally starting from liquid. For the problems of fluid in motion, the mathematical models are set to explain flow behaviors and the way how to solve simulation problems. Many paradigms have been introduced to solve these models including experiment, analytical and numerical methods [1]. From the former studies, the facts showed that many problems could not be solved by analytical method. Subsequently, the numerical styles are well known and useful to evaluate nonlinear differential form.

The computational program in this work executes fluid dynamic problem [2] that is basically calibrated from Newtonian model before the heuristic algorithm of viscoelastic type is created. In industrial process, the implement of an initial trial design is required to reduce the expense of production whilst the suitable computational model is rechecking the results and effects in the construction to describe the physical behavior. After that the model is modified to optimize computing time and accuracy. This trial design is approved to offer a high performance in the engineering processing.

For Newtonian fluid, the proportion between shear stress and the rate of deformation is linear and both values start at zero or another meaning of constant viscosity, such as water, which describes via Navier-Stoke equation. The nonlinear viscosity is called “non-Newtonian”, which is known as dilatant fluid and pseudoplastic fluid. Viscoelastic fluids, one of non-Newtonian types, are important for polymer processing. The constitutive equations have been implemented to explain the results from the experiments. These equations are used to describe flow behaviors of viscoelastic fluids such as Maxwell, Oldroyd-B and Phan-Thein Tanner models.

To illustrate the complex behavior of fluid, the rheological equations of state and material functions are discretised from the conservation of mass and momentum equations. The numerical method was developed for solving different solutions in science and engineering arias, such as viscoelastic flows. The difficulty is appeared while solving the nonlinear partial differential equations in the mathematical model of the conservation of mass and momentum equations including constitutive equation. These equations have to be described as Navier-Stokes equations which reflect second order nonlinear partial differential equation with viscoelastic model. The numerical solution can manage complex problems efficiently.

Many numerical methods are widely utilized such as finite difference method (FDM) [3], finite element method (FEM) [4-7], and finite volume method (FVM) [8-10] to get the least error approximate solution. Ngamaramvaranggul and Webster [11, 12] calculated the simulation model for the pressure-tooling wire-coating flows with Phan-Thien/Tanner fluid using the standard FEM under the stability of streamline-upwind Petrov/Galerkin (SUPG). Consequently, Puangkird et al. [13, 14] generalized transient computation of start-up pressure-driven for viscoelastic flow and then applied to compute in cross-slot devices with mixed finite volume/element method.

The strong elongation and violent shear stress at contraction position [15-17] play an important role in 4:1 contraction problem for viscoelastic fluid. Originally observation from the experiment [18, 19] of non-complicated fluid such as Boger fluid [20] was presented. The study included flow characteristics associated with abrupt changes in geometry also as lip-vortex mechanism of vortex enhancement in planar contraction flows [21]. To extend advanced fluid, the solution of 4:1 planar contraction for Oldroyd-B model [9] was evaluated via a semi-Lagrangian FVM. After the result of planar system has showed significant error then alternative axisymmetric system [10] was applied to correct this perturbation. Recently, the extensional flow of a polystyrene Boger fluid in the cylindrical coordinate system [22] through a 4:1 contraction was displayed. The development of numerical simulation for viscoelastic square contraction flows such as Oldroyd-B and PTT models [23-25] was proceeded while some solutions were clearly visualized and compared with other literatures. Not only the observation of contraction ratio effect [26, 27] was made but also correction

for improper inlet boundary condition was applied. The positive result of feedback pressure-driven velocity flow [28] was introduced to make solution more secure.

Another problem that was included in this thesis was die swell flow. In real problem, the steep shear stress occurs at die wall because of high velocity near die exit. Hence, the slip velocity at die wall has been added in order to reduce shear stress at singularity point. At the beginning when slip effect [29] was determined, Newtonian and viscoelastic fluids for two dimensional Cartesian coordinate system were examined. After the observation of experimental work [30], slip velocity was set as a function [31] of wall shear stress for capillary tube problem. Another definition was created by Phan-Thien [32] who combined three slip conditions to one slip equation that is consisted of critical and wall shear stresses by switching stick velocity to slip speed if critical shear stress was greater than the wall shear stress. In 2000, Ngamaramvaranggul and Webster [33] added the slip condition to calculate the free surface problems for pressure- and tube-tooling die. Recently, the slip effect of 4:1 contraction problem for Newtonian and Oldroyd-B fluids was determined in [34, 35] to reduce the stress values and vortex size.

The die-swell problem shows the complex deformation of free surface shape and physical properties. For the non-Newtonian flow pass the singular point at die wall, the radius increase in viscoelastic fluid is as representative as the swelling ratio (χ). The extrudate of Newtonian fluid has χ less than polymer melt since the polymeric material gains more relaxation and memory time. Not only the streamline prediction method was set in this issue to predict the swelling ratio but also the flowrate-driven boundary condition was adjusted to get more precise outcome by adjusting velocity of initial condition with a semi-implicit Taylor-Galerkin pressure-correction finite element method (STGFEM).

For the simulation model of industry process, the simple form of stick-slip flow [36] is observed before the complicated flows of die swell problem are concerned. After the flow passes from a stick entry part to a free exit section, the singularity of severe stress and steep velocity gradients region will appear. A singular finite element method [37] was introduced to compute the Stokes flow of stick-slip problem in the

neighborhood of the singular point and then the integrated singular basis function method [38] was reformed to improve the accuracy of the solution for the same problem including die-swell flow as well.

The singularity point of swelling extrusion position is rough and the free surface path will become shark skin [39] in case of high speed so this phenomenon is a noteworthy point in rheology and importance in polymer melt. The calculation of surface shape for analytical solution under creeping flow and ignored gravity condition in large surface tension is reported including melt fracture. An estimation of extrudate swell is included a dominant surface tension case for the extrudate processes. The observation for steep center of low order elements showed that the accuracy of solution is far away from real solution due to high values of the stress and strain near the singularity. To reduce this effect, the semi-radial singularity mapping theory [40] is applied along with various numerical works of the die-swell flow for Newtonian and viscoelastic fluid by Tanner [41].

A variety of numerical methods were presented to improve accuracy convergence and quality of solutions as same as singular function scheme. The singular boundary element method (SBEM) [42] is proposed to explore the approximate solution near singularity approaching the solution. Cuvelier et al. [43] proffered the singular expansion series to correct stress near singular point. Many finite element techniques are created for execute stick slip and die-swell flows, such as mesh refinement solutions, Galerkin [44] and collocation methods [45]. Consequently, a mixed FEM [6] is employed to resolve the problems of slit, circular, and annular dies for Newtonian and Maxwell fluids. Although illustration of finer mesh was emboldened to focus on elements at the singularity of die swell case, the solutions maintained space between analytical and approximate solutions.

To design die more efficiently and accurately, all factors affecting the extrudate shape must be monitored. A relation of velocity near solid wall versus swelling ratio for the free surface flow is noticed after numerical solution gave high swelling path. One reason to explain this situation is slip effect [29] and surface tension so a simple type of Newtonian case was the first to be determined. Then the slip condition for the

complex flows were considered next through a boundary element method [32] with alternative free-surface location technique in planar flows for viscoelastic fluids; Not only numerical study but also experiment is set to observe polyisobutylene-polybutene fluid [46] in axisymmetric isothermal flows. The advanced geometries are designed for pressure- and tube-tooling die processes [33] under high extensional viscosities of PTT flows. The calculations of flows are preserved free surface behaviors via STGFEM with slip effect technique. Simultaneously with this standard FEM, streamline-upwind Petrov/Galerkin (SUPG) [47] and local gradient recovery are applied to stabilize the converge solution.

To develop visualization on free surface shape more real, many studies were investigated in three dimensions (3D). The influence of heat [48] was present for three-dimensional non-isothermal extrusion flows. The unconstrained extrudate solution of Newtonian fluids at finite Reynolds number for three-dimensional planar and axisymmetric dies [49] was calculated via boundary and finite element methods. A simple shear flow in Wagner integral stress model [50] with a discrete spectrum of relaxation times and a single parameter damping function was determined in 3D for component of the experimental flow but the result was calculated in terms of the two-dimensional ordinary space. In this die swell case, the particles track was observed as spirals or helices in the planar entry free surface flow of molten polyethylenes.

In this work, Newtonian and Oldroyd-B fluids are modeled for die-swell and 4:1 contraction problems under STGFEM simultaneously with SUPG and local gradient recovery. The slip effect and feedback pressure-driven velocity flow are both conditions to modify solution getting real outcome. The benchmark of this algorithm and other literatures is expressed in a way that is clearly understood via figure and table presentations.

In Chapter II, the properties of basic rheology fluid is explored to predict the behavior of fluid flows through Navier-Stokes equation of Newtonian and the constitutive equations of viscoelastic fluids, such as Maxwell, Oldroyd-B, and Phan-Thien Tanner models. The basic viscometric flows are simple shear and elongation flows, which describe the properties of material.

Chapter III introduces numerical algorithm of semi-implicit Taylor-Galerkin pressure-correction finite element method (STGFEM), solvers of linear equations, streamline prediction method and some special techniques for solution stability. The STGFEM is used to discretise the nonlinear differential models comprising Navier-Stoke equation and Oldroyd-B model. The velocity gradient recovery as well as the streamline-upwind Petrov/Galerkin (SUPG) techniques are chosen to stabilize the converge solutions. The feedback of pressure-driven velocity flow is also taken to adjust the proper initial inlet boundary.

In Chapter IV, the slip effect scheme is considered in the problem of 4:1 planar contraction flow with sharp corner geometry in both Newtonian and Oldroyd-B fluids. The numerical solution of two dimensional planar isothermal incompressible flow is computed. Finally, the solutions of Oldroyd-B model with and without the slip effect are compared with other numerical solutions. The new numerical technique and called feedback pressure-driven velocity flow is added to approve accuracy and eliminate the problem of divergent solution in 4:1 planar contraction flow with rounded corner geometry in Newtonian and Oldroyd-B fluids.

Chapter V involves the free surface or die-swell problem under two dimensional axisymmetric isothermal incompressible flows. The streamline prediction method is set in this issue to predict the swelling ratio. Feedback pressure-driven velocity flow is taken to support the calculation of free surface path. Since fluid trail is shown complex deformation when it confronted with intermediate border between stick and slip boundaries, the diameter of extrudate for viscoelastic problem is varied when the property of liquid gets more flexibility. The manner of motion prognosticates its swelling ratio by calculation of a semi-implicit Taylor-Galerkin pressure-correction finite element method (STGFEM) simultaneously with treatment of pressure-driven velocity feedback to provide a precise solution of Newtonian and Oldroyd-B fluids. Moreover, the stability of approximated solutions is supported by local gradient recovery and the streamline-upwind Petrov/Galerkin techniques under two dimensional axisymmetric isothermal incompressible flow. The solution is recomputed by gradual increase of Weisenberg number (We) to the highest limit. In addition, the pressure-driven velocity flow method has been taken to solve the

intensive *We* before the final prediction of swelling ratio was compared with other values in literatures.

In Chapter VI, a number of researches and the numerical results are analyzed for suggestions in future works.

CHAPTER 2
NEWTONIAN AND NON-NEWTONIAN FLOWS

This chapter presents a brief explanation about rheology and the properties of fluid materials, found in the book of Tanner [41]. Rheology is a subject of flow and deformation behavior of materials. Especially for fluid in motion, the behavior of flow is considered from forces and momentum conduced to governing equations. One simple kinematics of continuum under linear relation between force and shear rate is Newtonian fluid, which has the property of a dynamic viscosity independently of motion. This kind of fluid is expressed in Navier-Stokes equations while non-Newtonian fluid has extra equation of shear and extensional properties in a form of constitutive model. Newtonian fluid has a constant viscosity relating to stress and rate of deformation while a substance in solid obeys the Hooke's law of a constant modulus of elasticity relating stress and magnitude of deformation. In case of Non-Newtonian fluids, there are various behaviors, which are depended on the material type, expressed variable proportionality between stress and deformation rate. An effect of viscosity when the fluid resistance decreased with an increasing rate of shear stress is called shear thinning and the fluid of this specific character is named pseudoplastic. This property is discovered in some complex solutions, such as blood, whipped cream, ketchup, and molten polymer. Another effect of shear viscosity happened when the viscosity increases with applied shear stress is named shear thickening substance and this material type is dilatant fluid. Some dilatant fluids are difficult to process in industrial factory because they are solid-in-liquid dispersion. Bingham fluids, like toothpaste and oil paints, resist movement to critical stress which exceeds the yield stress. In Figure 2.1, types of rheological behaviors show the relation between the time rate of deformation and shear stress.

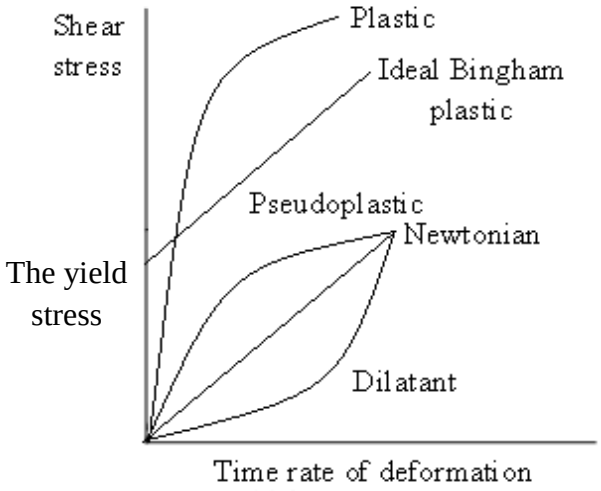

Figure 2.1 Types of rheological behavior

All fluids in motion satisfy Newton's second law, which states a mass moving with acceleration is proportional to resultant force. The resultant force (F) is a product of mass (m) and acceleration (*a*) as $\Sigma F = ma$. The shear stress (τ_{xy}) is a kind of force of friction when fluid is sheared and acting on a body in the fluid path. The shear stress is simple defined as the product of the shear rate ($\dot{\gamma}$) and the shear viscosity (μ_s). It can be expressed as,

$$\tau_{xy} = \mu_s \dot{\gamma} \tag{2.1}$$

For a Newtonian fluid, μ is a function of temperature and pressure, but for non-Newtonian fluid, μ is a function of the shear rate.

2.1 Basic Equations

In fluid behaviors, the basic equations of isothermal and incompressible flows are comprised by the conservation of mass, the conservation of momentum, and the constitutive equation. These equations are derived in differential equations as functions of space and time to describe flows and materials of fluids.

From the conservation of mass, the differential form is related between the density (ρ) and the velocity ($\mathbf{U}$) as the functions of position in space and time which is expressed as,

$$\frac{\partial \rho}{\partial \mathrm{t}} + \nabla.(\rho \mathbf{U}) = 0 \ . \tag{2.2}$$

For isothermal and incompressible flow, the density is constant, thus Equation (2.2) transforms to the continuity equation

$$\nabla \cdot \mathbf{U} = 0 . \tag{2.3}$$

From Newton's second law of motion, the conservation of linear momentum states that the external forces acting on the fluid mass body is equal to the change in the momentum. The external forces are made up of two distinct groups, surface and body forces. The Cauchy stress tensor ($\boldsymbol{\sigma}$) which is the surface force but the gravity force (g) which is the body force is discarded in this thesis. For incompressible fluids, the Cauchy stress is reduced to isotropic pressure (p) and the extra-stress tensor (**T**)

$$\boldsymbol{\sigma} = \mathbf{T} - \mathrm{p}\mathbf{I} . \tag{2.4}$$

For Newtonian fluids, the principle of the momentum conservation can be developed to the Navier-Stokes equations which are represented as,

$$\rho \frac{\partial \mathbf{U}}{\partial \mathrm{t}} = \mu \nabla^2 \mathbf{U} - \rho \mathbf{U} \cdot \nabla \mathbf{U} - \nabla \mathrm{p} . \tag{2.5}$$

From Equation (2.5), the momentum equation can be expressed in extra-stress tensor form which is related with the rate of deformation tensor (**D**) as,

$$\rho \frac{\partial \mathbf{U}}{\partial \mathrm{t}} = \nabla \cdot \mathbf{T} - \rho \mathbf{U} \cdot \nabla \mathbf{U} - \nabla \mathrm{p} \tag{2.6}$$

$$\mathbf{T} = 2\mu \mathbf{D} \tag{2.7}$$

$$\mathbf{D} = \frac{1}{2}(\nabla \mathbf{U} + \nabla \mathbf{U}^t) \tag{2.8}$$

These material variables are characterized to dimensionless variables by scaling appropriately non-dimensional variables which are $x^*, y^*, \mathbf{U}^*, p^*, \mathbf{T}^*, t^*, \nabla^*$, $\frac{D}{Dt^*}, \lambda_i^*$ and μ_i^* where L is a representative length, $\mathbf{V}$ is a representative velocity, and μ_0 is a representative viscosity.

$$x^* = \frac{1}{L}x,\ y^* = \frac{1}{L}y,\ \mathbf{U}^* = \frac{1}{\mathbf{V}}\mathbf{U},\ p^* = \frac{1}{\mu_0 \mathbf{V}}p,\ \mathbf{T}^* = \frac{L}{\mu_0 \mathbf{V}}\mathbf{T},$$

$$t^* = \frac{\mathbf{V}}{L}t,\ \nabla^* = L\nabla,\ \frac{D}{Dt^*} = \frac{L}{\mathbf{V}}\frac{D}{Dt},\ \mu_i^* = \frac{1}{\mu_0}\mu_i \qquad (2.9)$$

Equation (2.3) and (2.5) are transformed to dimensionless forms by using characteristic variables in Equation (2.9) and then * notation is discarded. Navier-Stokes equation and the continuity equation are written as,

$$\nabla.\mathbf{U} = 0 \qquad (2.10)$$

$$\mathrm{Re}\frac{\partial \mathbf{U}}{\partial t} = \nabla \cdot \mathbf{T} - \mathrm{Re}\,\mathbf{U} \cdot \nabla \mathbf{U} - \nabla p \qquad (2.11)$$

$$\mathrm{Re} = \frac{\rho \mathbf{V} L}{\mu_0} \qquad (2.12)$$

For Newtonian fluids, the physical constant which is made up from transformation is the nondimensional Reynolds number (Re). The Reynolds number is a ratio of the inertial to viscous force. In the most common physical circumstances the inertial forces dominate over motions or small viscosity as $\mathrm{Re} \to \infty$. When Re is very low, flows are called creeping flows.

For non-Newtonian fluids, the viscous properties of the viscoelastic fluids are introduced via the extra stress tensor where $\boldsymbol{\tau}$ is the polymer stress contribution:

$$\mathbf{T} = 2\mu\mathbf{D} + \boldsymbol{\tau} \qquad (2.13)$$

When the viscoelastic flows are expressed in the equations of nondimensional system, the dimensionless Weissenberg number (*We*) is obtained from scaling variables. The

Weissenberg number is the ratio of the relaxation time (λ_1) and a specific process time. *We* is similar to the Deborah number (*De*), which is the ratio of the relaxation time to the deformation **T** in Equation (2.14) and (2.15).

$$We = \frac{\lambda_1 \mathbf{V}}{\mathrm{L}} \tag{2.14}$$

$$De = \frac{\lambda_1}{\mathbf{T}} \tag{2.15}$$

2.2 Constitutive Equations

For fluid dynamics in physics and engineering, a constitutive equation or equation of state is a model of kinetic quantities especially stresses. This model shows the effect of force in term of stresses after being applied to strains so it is very well defined as deformations. The first constitutive equation was represented by Robert Hooke [51] who has created stress-strain relation known as Hooke's law. This law is dealt with the case of linear elastic materials.

2.2.1 The Maxwell Model

The constitutive equation of Maxwell model [52, 53], which is used to describe the behaviors of viscoelastic fluids, in differential expression is introduced in equation (2.16)**.** This equation is made up from the combination of Hooke's law for elasticity and Newton's law of viscosity [54].

$$\mathbf{T} + \frac{\mu_0}{\mathrm{G}} \cdot \frac{\partial \mathbf{T}}{\partial \mathrm{t}} = 2\mu_0 \mathbf{D} \tag{2.16}$$

where G is constant for the elastic modulus and $\frac{\mu_0}{\mathrm{G}}$ is represented by the characteristic time λ.

2.2.2 The Oldroyd-B Model

Since the Maxwell model does not obey the material principle, Oldroyd [55] has replaced the original time derivative by a convected derivative term. There are two convected alternatives known as the nonlinear lower convected and nonlinear upper convected forms as shown in Equations (2.18) and (2.20) respectively.

The nonlinear lower convected Maxwell model (LCM) is defined as,

$$\mathbf{T} + \lambda \overset{\Delta}{\mathbf{T}} = 2\mu_0 \mathbf{D} \tag{2.17}$$

where the lower convected derivative of the extra stress tensor ($\overset{\Delta}{\mathbf{T}}$) is expressed as,

$$\overset{\Delta}{\mathbf{T}} = \frac{\partial \mathbf{T}}{\partial \mathrm{t}} + \mathbf{U}\cdot\nabla\mathbf{T} + \mathbf{T}\cdot\nabla\mathbf{U} + (\mathbf{T}\cdot\nabla\mathbf{U})^t \tag{2.18}$$

The nonlinear upper convected Maxwell model (UCM) is defined as,

$$\mathbf{T} + \lambda \overset{\nabla}{\mathbf{T}} = 2\mu_0 \mathbf{D} \tag{2.19}$$

where the lower convected derivative of the extra stress tensor ($\overset{\nabla}{\mathbf{T}}$) is express as,

$$\overset{\nabla}{\mathbf{T}} = \frac{\partial \mathbf{T}}{\partial \mathrm{t}} + \mathbf{U}\cdot\nabla\mathbf{T} - \mathbf{T}\cdot\nabla\mathbf{U} - (\mathbf{T}\cdot\nabla\mathbf{U})^t \tag{2.20}$$

The general convected Oldroyd equation can be obtained from the upper derivative with the characteristic time (λ_i), $\mathrm{i} = 1,\ldots,7$. All quadratic terms are the products of $\mathbf{T}$, $\mathbf{D}$ and $\overset{\nabla}{\mathbf{D}}$ where $\overset{\nabla}{\mathbf{D}}$ is the upper convected derivative of the rate of deformation tensor.

$$\tau + \lambda_1 \overset{\nabla}{\mathbf{T}} + \frac{1}{2}\lambda_3(\mathbf{D}\cdot\mathbf{T} + \mathbf{T}\cdot\mathbf{D}) + \frac{1}{2}\lambda_5 \mathbf{T}\,{}^t\mathbf{D} + \frac{1}{2}\lambda_6(\mathbf{T}\cdot\mathbf{D})\mathbf{I}$$

$$= 2\mu_0\left(\mathbf{D} + \lambda_2 \overset{\nabla}{\mathbf{D}} + \lambda_4(\mathbf{D}\cdot\mathbf{D}) + \frac{1}{2}\lambda_7(\mathbf{D}\cdot\mathbf{D})\mathbf{I}\right)(\mathbf{T}\cdot\mathbf{D})\mathbf{I} \tag{2.21}$$

To reduce the complicated equation, some characteristic time variables in Equation (2.21) is possible to be discarded, thus Oldroyd-B model is defined as,

$$\mathbf{T} + \lambda_1 \overset{\nabla}{\mathbf{T}} = 2\mu_0(\mathbf{D} + \lambda_2 \overset{\nabla}{\mathbf{D}}) \tag{2.22}$$

and

$$\mu_0 = \mu_1 + \mu_2 \tag{2.23}$$

where μ_1 is elastic solute viscosity, μ_2 is Newtonian solvent viscosity.

The retardation time λ_2 is express as

$$\lambda_2 = \frac{\lambda_1 \mu_2}{\mu_1 + \mu_2} \tag{2.24}$$

The extra stress tensor in Equation (2.22) was split into viscous and elastic from the work of Paddon and Holstein [3] and Crochet and Keunings [6, 56], hence the Oldroyd-B model expression is defined as:

$$\mathbf{T} = 2\mu_2\mathbf{D} + \boldsymbol{\tau} \tag{2.25}$$

$$\boldsymbol{\tau} + \lambda_1 \overset{\nabla}{\boldsymbol{\tau}} = 2\mu_1\mathbf{D} \tag{2.26}$$

where $\overset{\nabla}{\boldsymbol{\tau}}$ is the upper convected derivative of the polymer stress contribution.

For isothermal flow, the 3-constant Oldroyd-B model must satisfy the constraint equation as below:

$$\lambda_1 \geq \lambda_2 \geq 0 \tag{2.27}$$

The decomposition of the extra stress tensor can be brought to elastic and Newtonian parts as shown in Equation (2.25) while Equation (2.26) only expresses a pure viscous term. Oldroyd-B model can be concerned as an extension of the upper convected Maxwell model and it will become the upper convected Maxwell model if the solvent viscosity is zero. In this thesis, Oldroyd-B model is the representation of constitutive form for 4:1 contraction and die-swell flows because the product of this model gives

the least error approximations in shear flow. The nondimensional system of Oldroyd-B model is expressed in equation (2.28).

$$We\frac{\partial \boldsymbol{\tau}}{\partial \mathrm{t}} = 2\mu_1\mathbf{D} - \boldsymbol{\tau} + We(\boldsymbol{\tau}\cdot\nabla\mathbf{U} + (\nabla\mathbf{U})^t\cdot\boldsymbol{\tau} - \mathbf{U}\cdot\nabla\boldsymbol{\tau}) \tag{2.28}$$

2.2.3 The Phan-Thien/Tanner (PTT) Model

Phan-Thien and Tanner [57, 58] have introduced the particular constitutive model from network theory for melting flows of polymeric material. The nonlinear constitutive Phan-Thien/Tanner model is well defined to explain flow behavior of viscoelastic fluid. It is the state of art to show the rate of creation and destruction for a framework of network junctions under softening or hardening behavior. The PTT model gives accurate narration of steady-state and transient properties.

The single relaxation time PTT constitutive equation is defined as,

$$f\boldsymbol{\tau} + \lambda_1 \overset{\square}{\boldsymbol{\tau}} = 2\mu_1\mathbf{D} \tag{2.29}$$

$$\overset{\square}{\boldsymbol{\tau}} = \overset{\nabla}{\boldsymbol{\tau}} + \xi(\mathbf{D}\cdot\boldsymbol{\tau} + \boldsymbol{\tau}\cdot\mathbf{D}) \tag{2.30}$$

The exponential term f in general form is expressed as

$$f = \exp[\frac{\varepsilon\lambda_1}{\mu_1}tr(\boldsymbol{\tau})] \tag{2.31}$$

where $\overset{\square}{\boldsymbol{\tau}}$ is the Gordon-Scholwalter convected derivative, ξ and ε are adjustable non-dimensional model material parameters where ξ falls within the range $0 \le \xi \le 2$. ξ and ε control shear and elongation behavior, respectively.

Taking a Taylor series approximation and truncating at first order terms to the exponential form f, a linear PTT model is illustrated as

$$f = 1 + \frac{\varepsilon\lambda_1}{\mu_1}tr(\boldsymbol{\tau}) \tag{2.32}$$

Using this approach and truncating at second order terms, a quadratic PTT model is identified as

$$f = 1 + \frac{\varepsilon\lambda_1}{\mu_1} tr(\boldsymbol{\tau}) + \frac{1}{2}\left(\frac{\varepsilon\lambda_1}{\mu_1} tr(\boldsymbol{\tau})\right)^2 \tag{2.33}$$

The quadratic PTT model is reduced to the Oldroyd-B model when ξ and ε are vanished.

2.3 Basic Flows

In liquid, the two common shear and extensional flows exhibit the relative movement for adjacent particles. In shear flows liquid elements flow over or past each other, while in extensional flow, adjacent elements flow towards or away from each other [59].

2.3.1 Simple Shear Flow

Considering simple shear flow, the fluid flows between two parallel plates. The top plate free to move under an applied force and the bottom plate is fixed (Stationary plate). The top plate is dragged at constant velocity **u** across the fluid. The shear rate across the layer is as shown in Figure 2.2.

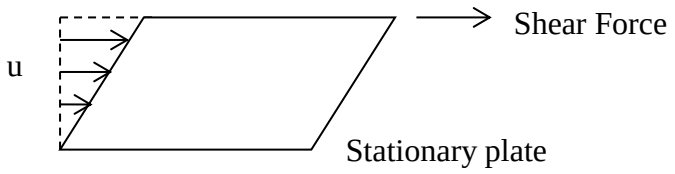

Figure 2.2 Particle motion in shear flow

The velocity components (u_x, u_y, u_z) within a Cartesian coordinate system are represented in simple viscometric shear flow as,

$$u_x = \dot{\gamma} y,\ u_y = u_z = 0 \tag{2.34}$$

The shear rate can be expressed in the velocity gradient as,

$$\dot{\gamma} = \frac{\mathrm{du_x}}{\mathrm{dy}} \tag{2.35}$$

The primary normal stress difference (N_1) and the second normal stress difference (N_2) can be used to describe the rotation of the fluid elements [60]. They are defined in the normal stresses $(\tau_{xx}, \tau_{yy}, \tau_{zz})$ or the primary and secondary normal stress function (ψ_1, ψ_2) as below,

$$N_1 = \tau_{xx} - \tau_{yy} = \dot{\gamma}^2 \psi_1(\dot{\gamma}) \tag{2.36}$$

$$N_2 = \tau_{yy} - \tau_{zz} = \dot{\gamma}^2 \psi_2(\dot{\gamma}) \tag{2.37}$$

$$\tau_{xy} = \mu_s \dot{\gamma} \tag{2.38}$$

For Oldroyd-B model, the shear viscosity and first normal stress can be expressed as function of the shear rate:

$$\mu_s(\dot{\gamma}) = \mu_0 \tag{2.39}$$

$$\psi_1(\dot{\gamma}) = 2\mu_0(\lambda_1 - \lambda_2)\dot{\gamma}^2 \tag{2.40}$$

Similarly, for exponential PTT model, $\mu_s(\dot{\gamma})$ and $\psi_1(\dot{\gamma})$ are

$$\mu_s(\dot{\gamma}) = \frac{\mu_0 \dot{\gamma}}{1 + \lambda_1^2 \dot{\gamma}^2 \xi(2-\xi)} \tag{2.41}$$

$$\psi_1(\dot{\gamma}) = \frac{2\mu_0 \lambda_1 \dot{\gamma}^2}{1 + \lambda_1^2 \dot{\gamma}^2 \xi(2-\xi)} \tag{2.42}$$

2.3.2 Extensional (Elongational) Flow

The important property of elastic fluid is extensional viscosity behavior, which is formulated from a term of stress depended on the strain (ε). Extensional flow [61, 62] is shear-free flow which is classified into three types: uniaxial, biaxial, and planar flows. The rate of extension ($\dot{\varepsilon}$) is described as the function of the velocity profiles.

Figure 2.3 Particle motion in uniaxial extensional flow

At the conservation of mass and axial symmetry, the extensional rate is the velocity distribution depending on flow direction and time even if all shear stress components are zero.

$$\dot{\varepsilon} = \frac{du_x}{dx} = -2\frac{du_y}{dy} = -2\frac{du_z}{dz} \tag{2.43}$$

$$\tau_{xy} = \tau_{xz} = \tau_{yz} = 0 \tag{2.44}$$

For an incompressible fluid, the stress difference is related with the extensional rate and the extensional viscosity (μ_e) can be expressed as,

$$\tau_{xx} - \tau_{yy} = \tau_{yy} - \tau_{zz} = \dot{\varepsilon}\mu_e(\dot{\varepsilon}) \tag{2.45}$$

Biaxial flow is deformed in two particular directions as illustrated in Figure 2.4. This flow is called stretching flow, which is represented as both a function of time and elongation rate.

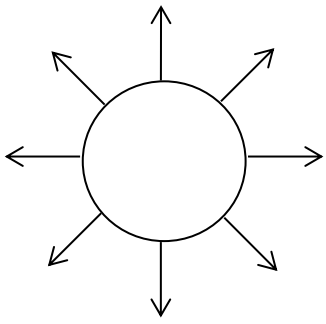

Figure 2.4 Particle motion in biaxial extensional flow

Walter showed the relation between uniaxial viscosity and biaxial viscosity as:

$$\mu_{eb}(\dot{\varepsilon}) = \mu_{e}(-2\dot{\varepsilon}) \tag{2.46}$$

The elongation rate for biaxial flow is:

$$\dot{\varepsilon} = \frac{u_x}{x} = \frac{u_y}{y} = -\frac{1}{2}\frac{u_z}{z} \tag{2.47}$$

The stress differences are given by:

$$\tau_{zz} - \tau_{xx} = \tau_{zz} - \tau_{yy} = \dot{\varepsilon}\mu_{eb}(\dot{\varepsilon}) \tag{2.48}$$

$$\tau_{xy} = \tau_{xz} = \tau_{yz} = 0 \tag{2.49}$$

Normally in planar extension flow, the liquid volume is distorted in two directions act against each other, stretch in one direction and extension in another direction as depicted in Figure 2.5.

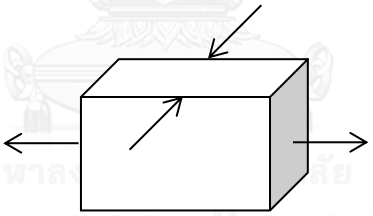

Figure 2.5 Particle motion in planar extensional flow

The elongation rate for planar extension flow is:

$$\dot{\varepsilon} = \frac{u_x}{x} = -\frac{u_z}{z} \quad \text{and } u_y = 0 \tag{2.50}$$

The stress difference is

$$\tau_{xx} - \tau_{zz} = \dot{\varepsilon}\mu_{ep}(\dot{\varepsilon}) \tag{2.51}$$

For Oldroyd-B model, the extensional viscosity can be expressed in the following function of the extensional rate.

$$\mu_e(\dot{\varepsilon}) = 2\mu_0 \frac{(1-2\lambda_2\dot{\varepsilon})}{(1-2\lambda_1\dot{\varepsilon})} + \mu_0 \frac{(1+\lambda_2\dot{\varepsilon})}{(1+\lambda_1\dot{\varepsilon})} \tag{2.52}$$

Correspondingly, for exponential PTT model, the extensional viscosity is represented as:

$$\mu_e(\dot{\varepsilon}) = \frac{2\mu_0}{1-2\lambda_1\dot{\varepsilon}(1-\xi)} + \frac{\mu_0}{1+\lambda_1\dot{\varepsilon}(1-\xi)} \tag{2.53}$$

2.3.3 The Second and Third Invariants of the Rate of Strain Tensor

Considering inelastic homogeneous isotropic fluid behavior under isothermal non-Newtonian flow, the extra stress of a Reiner-Rivin fluid [63, 64] is defined as a function of deformation tensor within an incompressible body. It is expressed as,

$$\mathbf{T} = 2\mu(\dot{\gamma}, \dot{\varepsilon})\mathbf{D} \tag{2.54}$$

where the shear rate of simple shear flow is

$$\dot{\gamma} = 2\sqrt{\mathrm{II_d}} \tag{2.55}$$

and the elongation rate for elongation flow is

$$\dot{\varepsilon} = 3\frac{\mathrm{III_d}}{\mathrm{II_d}} \quad . \tag{2.56}$$

The second invariant ($\mathrm{II_d}$) of the rate of strain tensor **D** in a Cartesian coordinate system is

$$\mathrm{II_d} = \frac{1}{2}tr(\mathbf{D}^2) = \frac{1}{2}\left\{\left(\frac{\partial \mathrm{u_x}}{\partial \mathrm{x}}\right)^2 + \left(\frac{\partial \mathrm{u_y}}{\partial \mathrm{x}}\right)^2 + \frac{1}{2}\left(\frac{\partial \mathrm{u_x}}{\partial \mathrm{y}} + \frac{\partial \mathrm{u_y}}{\partial \mathrm{x}}\right)^2\right\} \tag{2.57}$$

The third invariant ($\mathrm{III_d}$) of the rate of strain tensor **D** is

$$\mathrm{III_d} = \det(\mathbf{D}) = -\mathrm{II_d} \tag{2.58}$$

Similarly, in an axisymmetric coordinate system $\mathrm{II_d}$ and $\mathrm{III_d}$ are described as:

$$II_d = \frac{1}{2} tr(\mathbf{D}^2) = \frac{1}{2}\left\{\left(\frac{\partial u_r}{\partial r}\right)^2 + \left(\frac{\partial u_z}{\partial z}\right)^2 + \left(\frac{u_r}{r}\right)^2 + \frac{1}{2}\left(\frac{\partial u_r}{\partial z} + \frac{\partial u_z}{\partial r}\right)^2\right\} \quad (2.59)$$

and

$$III_d = \det(\mathbf{D}) = \frac{u_r}{r}\left\{\frac{\partial u_r}{\partial r}\frac{\partial u_z}{\partial z} - \frac{1}{4}\left(\frac{\partial u_r}{\partial z} + \frac{\partial u_z}{\partial r}\right)^2\right\} \quad . \quad (2.60)$$

2.4 Stream Function

The streamlines represent the trajectories of particles in a steady flow via stream function. The flow velocity component can be defined as the derivatives of the scalar stream function. In case of fluid dynamics, the difference between the stream function values at any two points gives the volumetric flux across the line between A and P as shown in Figure 2.6.

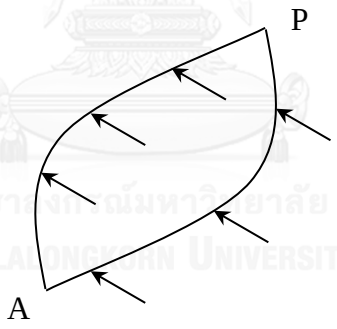

Figure 2.6 Flow direction in stream function

For two dimensional incompressible flows, Lamb [65] and Batchelor [66] have defined the stream function $\psi(x, y)$ in the Cartesian coordinate system (x, y). The stream function $\psi(x, y)$ is expressed as,

$$\psi = \int_A^P (udy - vdx) \quad (2.61)$$

$$\frac{\partial u_x}{\partial x} + \frac{\partial u_y}{\partial y} = 0 \tag{2.62}$$

$$u_x = \frac{\partial \psi}{\partial y} \quad \text{and} \quad u_y = -\frac{\partial \psi}{\partial x} \tag{2.63}$$

The derivation of stream function in form of Poisson equation is

$$\frac{\partial^2 \psi}{\partial x^2} + \frac{\partial^2 \psi}{\partial y^2} = \frac{\partial u_y}{\partial x} - \frac{\partial u_x}{\partial y} = f_s \tag{2.64}$$

For cylindrical coordinate system (r, z), the stream function $\psi(r, z)$ is expressed as

$$u_r = \frac{1}{r}\frac{\partial \psi}{\partial z} \quad \text{and} \quad u_z = -\frac{1}{r}\frac{\partial \psi}{\partial r} \tag{2.65}$$

Transformation to the Poisson equation is

$$\frac{\partial^2 \psi}{\partial r^2} + \frac{\partial^2 \psi}{\partial z^2} = -r\frac{\partial u_z}{\partial r} + r\frac{\partial u_r}{\partial z} - u_z \tag{2.66}$$

CHAPTER 3
NUMERICAL METHODS

In science and engineering arias at recent years, a great deal of interest has been concentrated on invention and application. To develop the applied area, the simulations for many problems are set up under real conditions in order to reduce cost and time. For fluid model, the mathematical equations of the conservation of mass and momentum including constitutive equations are formulated from velocity, stress, pressure, and temperature especially for stress, which describe the physical behavior flow fluently. Instead of solving analytic solution of viscoelastic problem through that it is extremely hard to find either of complex integral or differential form of constitutive equations but this problem is eliminated via numerical methods. The aim of computational methods is the existing outcome that is observed from the accuracy, stability and convergence of the approximate solution so all numerical techniques are developed in order to encounter more complex problems.

There are various useful methods such as finite difference method (FDM), finite element method (FEM), and finite volume method (FVM) to calculate the nonlinear partial differential equation. One of productive early numerical scheme is FDM, which is a virtual apparatus to simulate flow phenomena. After trial and error with a lot of problems, the concept of FDM make us know that this numerical style cannot handle nonlinear nature of the governing system for differential forms that involve complicated shapes because this formulation is complex. Instate of basic FDM, FVM played an important role to resolve the complex flow situations in order to increase accuracy. For example flow, a semi-Lagrangian FVM [9, 10] is applied to estimate the abrupt contraction problems for non-Newtonian fluid on a Cartesian and an axisymmetric flows. Similarly, FEM can eliminate more errors that are suffered with reduction accuracy in the convoluted flows. A lot of simulations that have been solved by FEM are as following problems. In stick-slip flow of Oldroyd-B fluid, FEM is adopted to calculate final solution before step up to predict swelling ratio by added free surface method to adjust the streamline path so the updated flow become die-

swell problem [33, 67]. This technique is efficient to calculate flow characteristics at high Weisenberg numbers for Phan-Thien/Tanner fluid under the complex geometry of pressure-tooling wire-coating die via employment of the same standard FEM and streamline-upwind Petrov/Galerkin (SUPG) [12]. The advanced geometry of 4:1 contraction flow is computed with a cell-vertex hybrid finite volume/element method [8] for highly elastic solutions of Oldroyd-B and Phan-Thien/Tanner (PTT) fluids with rounded and sharp corner contraction figures. And then the technique of alternate subcell [68, 69] is added to interpolate cooperative stress of Oldroyd-B fluid via FV/FE methods for cavity and contraction flows. After that, the sufficient various schemes are investigated to consider constitutive models and rheological properties in cross-slot devices though FV/FE pressure correction method [14].

In this chapter, the numerical techniques utilized efficiently to eliminate complicated problems. Hence, the governing equations in 4:1 contraction domains and die-swell flow are discretised by a semi-implicit Taylor-Galerkin pressure-correction finite element method (STGFEM). These equations are formulated to a system of linear equation before the approximate solution is calculated by Jacobi iterative method and Cholesky decomposition scheme. The velocity gradient recovery and the streamline-upwind Petrov/Galerkin (SUPG) techniques are operated to stabilize the converge solutions. For slip case, Phan-Thien slip rule is a tool for finding appropriate slip velocity in case of 4:1 contraction problem [34] while feedback of pressure-driven velocity flow [28] is chosen to sustain the computation of free surface flow that includes theoretical prediction and numerical adjustment for die-swell paths.

3.1 Finite Element Method

The finite element method (FEM) [4, 5, 7] is a powerful developed technique for finding numerical solutions of complex problem in computation fluid dynamics. This method converts the governing flow equations (partial differential flow equations including velocity, pressure, stress, thermal, density, Young's modulus, Poisson's ratio, etc.) into a set of algebraic equations. For ease of structure, whole problem domain is subdivided in small parts called finite elements. All tiny straight lines are

connected nodes to numerous simple elements over many sub-domains with suitable initial and boundary conditions to minimize error approximate function. FEM can encounter the complex flow situations when a complicated domain is generated to a large degree of freedom.

This section describes the trial function approximation methods by a discrete model and it must be continuous over some region in space. The discrete model is built up with a set of this function for a finite number of points in the domain, as well as piecewise approximations of the function over a finite number of sub-domains, which are known as "finite elements". The solution is calculated over locally estimated shape function of each element so the steps are taken to obtain a finite element approximation in terms of the primary variables of the governing equation system, which involves the application of a classical trial solution method.

The finite element method is characterized by a variational formulation that discretization strategies are as follows:

1. Generate finite element meshes from a finite number of **n** points within the solution domain. The mesh is popular constructed in triangular or rectangular elements for two dimensions, and tetrahedral or hexahedral elements for three dimensions. In this research all meshes are considered in triangular elements for two dimensions as shown in Figure 3.1.

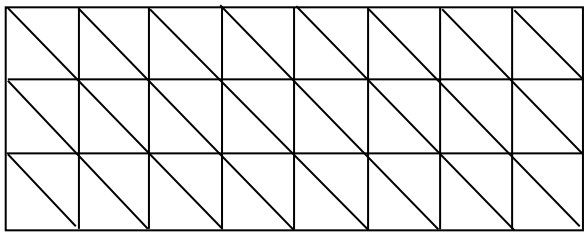

Figure 3.1 Triangular elements in two dimensions

2. Interpolate a trial solution for the primary variables $\tilde{\mathbf{U}}(x)$.

3. Use a variational or Galerkin weighted residual method. The process is constructed an integral of the inner product of the residual and the weight functions when integral is set to zero. In simple terms, it is a procedure that minimizes the error of approximation by fitting trial functions into the PDE. The residual is the error caused by the trial functions, and the weight functions are polynomial approximation functions that project the residual. This process eliminates all the spatial derivatives from the PDE thus a set of algebraic equations at steady state is constructed to approximate locally otherwise it can be a set of ordinary differential equations for transient problems.

An example of this expression of the trial solution ($\tilde{\mathbf{U}}(x)$) of the velocity variable u, as a finite sum of trial functions is:

$$\tilde{\mathbf{U}}(x) = \sum_{i=1}^{n} N_{\phi}^{i}(x)\mathbf{U}^{i} \tag{3.1}$$

where $N_{\phi}^{i}(x)$ is trial-basis function (also called interpolation shape functions). The summation extending over the entire mesh of **n** nodes (i=1,...,**n**). The unknown nodal values of the variables **U** are the parameters $\mathbf{U}^{i}$.

For this method, the trial functions N_{ϕ}^{i} are employed to approximate the global trial function $\tilde{\mathbf{U}}(x)$, which exists within a finite space (a "trial space"). The trial functions N_{ϕ}^{i} vanish outside their elements. It is noted that the number of nodes used in the integration is equal to the number of weighting functions N_{ϕ}.

$$N_{\phi}^{i}(x) = 0, \text{ if x is outside of element } e \tag{3.2}$$

Also, for the velocity function **U**(x) to be constant:

$$\sum N_{\phi}^{i}(x) = 1 \tag{3.3}$$

3.1.1 Weighted Residual Methods

The methods of weighted residuals are methods for solving global differential equations to minimize the calculated error. The solutions $\mathbf{U}(x)$ of the differential equations are supposed to be precise approximated by a finite sum of test functions ϕ_i. Baker [70] and Burnett [71] have illustrated common implementations, which are the Galerkin, the collocation, the sub-domain, the least-square and the least-square collocation methods. The weighted residual Galerkin method is selected in this work.

The residual approach will be shown in the two-dimensional boundary value problem for the Poisson equation within a Cartesian (x,y) coordinate system.

$$\frac{\partial^2 u}{\partial x^2} + \frac{\partial^2 u}{\partial y^2} + f = 0 \quad \text{within } \Omega \tag{3.4}$$

$$u = 0 \quad \text{on } \Gamma \tag{3.5}$$

where Γ is the boundary of the open domain Ω and f is a given function. The residual $R(u)$ of equation (3.4) is

$$R(u) = \frac{\partial^2 u}{\partial x^2} + \frac{\partial^2 u}{\partial y^2} + f \tag{3.6}.$$

After replacing the exact solution into the right-hand side of equation (3.6), the residual function is set to equalize to zero throughout the entire domain. The residual of an approximate trial-solution is non-zero. And then the Galerkin weighted residual method is applied to each element residual as following.

$$\sum_{e=1}^{N_e} \int_{\Omega_e} \phi(x) R(u) d\Omega = 0 \tag{3.7}$$

$$\Omega = \bigcup_{e=1}^{N_e} \Omega_e \tag{3.8}$$

where N_e is the total number of elements in the domain

ϕ is the weighted test function within a space of test functions.

Equation 3.8 is transformed to a set of linear algebraic system of equations and then it is solved by a variety of approaches. The result of the weighted residual that each of the coefficient weight is correspond with test function will minimize the error between the sum of the test functions and actual solution in a chosen norm.

$$E(x) = \mathbf{U}(x) - \tilde{\mathbf{U}}(x) \tag{3.9}$$

where $E(x)$ is the magnitude of analytical error between the finite element approximate solution $\tilde{\mathbf{U}}(x)$ and exact solution $\mathbf{U}(x)$.

3.1.2 Mapping Finite Elements

A global system of equations is generated from the element equations through a transformation of coordinates from the sub domains at local nodes to the domain at global nodes. This transformation includes appropriate orientation adjustments as applied in relation to the reference coordinate system. In the FEM, the discretization for a planar domain is modeled by a set of appropriate non-overlapping sub-domains (finite elements) interconnected at points called nodes. The common finite elements are triangle [44, 72-74] or quadrilateral [75-78] sub-divisions that are proved equally effective for finite element analysis. The conditions [70] of sub-divisions exist as below:

1. The number of sub-regions Ω_i within the domain is finite $\left(i = 1,2,3,..., N_e \right)$.

2. For two sub-regions Ω_1 and Ω_2, there is a common edge or vertex, $(\Omega_1 = \Omega_2)$ or $(\Omega_1 \cap \Omega_2 = \phi)$.

3. Under the combination of all sub-regions (elements) at entire boundary regions, the total area is the whole domain.

Triangular elements are constructed from linear representations of pressure and quadratic representations of velocity and stress as illustrated in Figure 3.2. For a

barycentric coordinate system (ξ, η), each elements shape function is linear ψ for pressure and quadratic ϕ for velocity and stress.

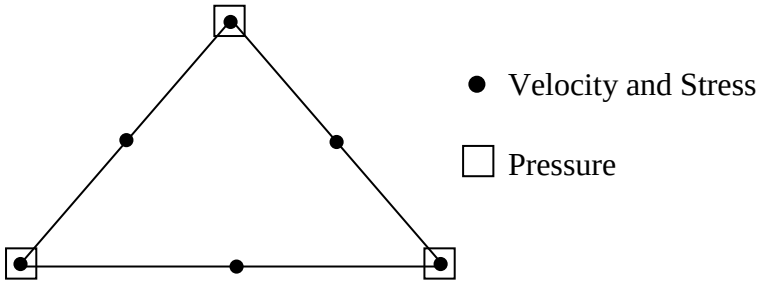

Figure 3.2 Linear and quadratic representations

For the 3 node element shown in Figure 3.3 the shape functions are given as

$$N_1^e(\xi,\eta) = 1-\xi-\eta \tag{3.10}$$

$$N_2^e(\xi,\eta) = \xi$$

$$N_3^e(\xi,\eta) = \eta$$

For the 6 node element shown in Figure 3.3 the shape functions are given as

$$N_1^e(\xi,\eta) = (1-\xi-\eta)(1-2\xi-2\eta) \tag{3.11}$$

$$N_2^e(\xi,\eta) = \xi(2\xi-1)$$

$$N_3^e(\xi,\eta) = \eta(2\eta-1)$$

$$N_4^e(\xi,\eta) = 4\xi(1-\xi-\eta)$$

$$N_5^e(\xi,\eta) = 4\xi\eta$$

$$N_6^e(\xi,\eta) = 4\eta(1-\xi-\eta)$$

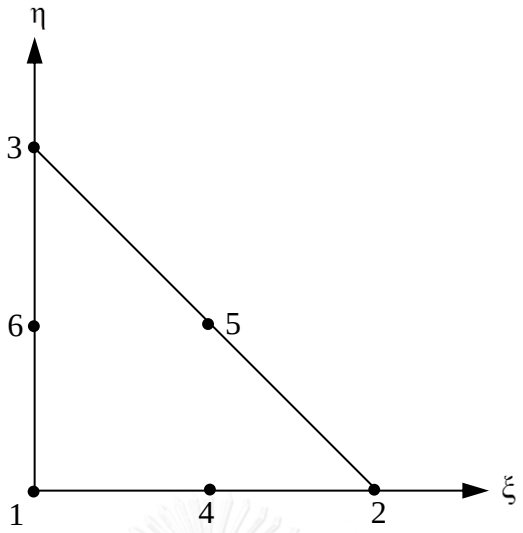

Figure 3.3 Right triangle element

5. The integration techniques are implemented after all proper meshes are constructed. A suitable coordinate system, barycentric coordinates, is chosen in order to evaluate the integrals of each sub-region in the finite element discretization as shown in Figure 3.4.

Each coordinate has magnitude one at its nodal position, and begins (magnitude zero) perpendicular to the surface regions boundary element opposite its corresponding node.

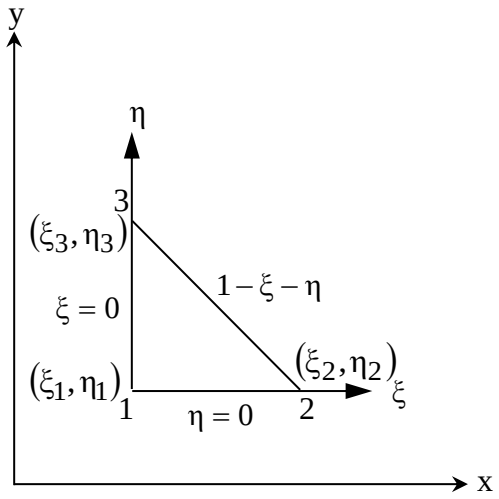

Figure 3.4 Barycentric coordinates (ξ, η)

The exact integral [43, 70] of a barycentric coordinate system for n-dimensions is

$$\int_{\Omega} \xi_1^{\mathbf{n}_1} \xi_2^{\mathbf{n}_2} \xi_3^{\mathbf{n}_3} d\Omega = \mathrm{Det}^n \frac{\mathbf{n}_1!\mathbf{n}_2!\mathbf{n}_3!}{(\mathbf{n}+\mathbf{n}_1+\mathbf{n}_2+\mathbf{n}_3)!} \tag{3.12}$$

where Det^n is the determinant of the coefficient matrix, ξ_i is coordinate system, and $\mathbf{n}_i$ (i=1,...,4) are positive integers.

For two dimensions, the determinant Det^n is equivalent to twice elements area. To predict the integration, the quadrature rule is considered for all polynomial form integrands. For the two-dimensional case, the Guass-Legendre quadrature formula for double integrals case is

$$\int_{-1}^{+1}\int_{-1}^{+1} f(x,y)d\Omega = \sum_{i=1}^{N_q}\sum_{j=1}^{N_q} W_i W_j f(x_i, y_j) \tag{3.13}$$

where W_i, W_j are weight coefficients and $f(x_i,y_i)$ is a function defined over an element.

The integrals of equation (3.13) is evaluated by converting to the coordinate system (ξ, η) [42] so equation (3.13) becomes

$$\int_{\Omega} f(x,y)d\Omega = \int_{\Omega^e} f(\xi(\eta)d\Omega^e \tag{3.14}$$

where $f(\xi, \eta)$ is a function sampled at the sampling point (ξ_i, η_i).

Figure 3.4 illustrates the nodes 1,2 and 3 as:

$$(\xi_1, \eta_1) = (0,0) \tag{3.15}$$

$$(\xi_2, \eta_2) = (1,0)$$

$$(\xi_3, \eta_3) = (0,1)$$

For velocity profiles, it can be written in the coordinate system (ξ, η) as:

$$\frac{\partial u}{\partial \xi} = \frac{\partial u}{\partial x} \cdot \frac{\partial x}{\partial \xi} + \frac{\partial u}{\partial y} \cdot \frac{\partial y}{\partial \xi} \tag{3.16}$$

$$\frac{\partial u}{\partial \eta} = \frac{\partial u}{\partial x} \cdot \frac{\partial x}{\partial \eta} + \frac{\partial u}{\partial y} \cdot \frac{\partial y}{\partial \eta}$$

Equation (3.16) is transformed in matrix form as:

$$\begin{bmatrix} \frac{\partial u}{\partial \xi} \\ \frac{\partial u}{\partial \eta} \end{bmatrix} = \begin{bmatrix} \frac{\partial x}{\partial \xi} & \frac{\partial y}{\partial \xi} \\ \frac{\partial x}{\partial \eta} & \frac{\partial y}{\partial \eta} \end{bmatrix} \begin{bmatrix} \frac{\partial u}{\partial x} \\ \frac{\partial u}{\partial y} \end{bmatrix} \tag{3.17}$$

The Jacobian matrix J of this transformation is

$$J = \begin{bmatrix} \frac{\partial x}{\partial \xi} & \frac{\partial y}{\partial \xi} \\ \frac{\partial x}{\partial \eta} & \frac{\partial y}{\partial \eta} \end{bmatrix} \tag{3.18}$$

$$J = \begin{bmatrix} x_2^{(e)} - x_1^{(e)} & y_2^{(e)} - y_1^{(e)} \\ x_3^{(e)} - x_1^{(e)} & y_3^{(e)} - y_1^{(e)} \end{bmatrix} \tag{3.19}$$

where $(x_1^{(e)}, y_1^{(e)})$, $(x_2^{(e)}, y_2^{(e)})$ and $(x_3^{(e)}, y_3^{(e)})$ are the (x,y) coordinates of the nodal points 1, 2 and 3 respectively.

The area in Cartesian coordinate system (x,y) is converted to the coordinate system (ξ, η). For elemental area of the sub-region, $d\Omega^{(e)} = dxdy$ is changed into $d\Omega' = d\xi d\eta$.

$$d\Omega^{(e)} = \det(J) d\xi d\eta \tag{3.20}$$

Equation (3.14) is expressed in the integral solution:

$$\int_{\Omega} f(x, y) d\Omega = \int_{\Omega'} f(\xi, \eta) \det(J) d\Omega' \tag{3.21}$$

3.2 Semi-implicit Taylor-Galerkin Pressure-Correction Finite Element Method (STGFEM)

To solve convection equations conveniently, the perfect union of factional time steps and FEM is applied to split non-dimensional equations. The generalised Navier-Stokes momentum equation (2.11) in addition to the continuity equation (2.10) and Oldroyd-B constitutive equation

$$We\frac{\partial \boldsymbol{\tau}}{\partial \mathrm{t}} = 2\mu_1\mathbf{D} - \boldsymbol{\tau} + We(\boldsymbol{\tau}\cdot\nabla\mathbf{U} + (\nabla\mathbf{U})^t\cdot\boldsymbol{\tau} - \mathbf{U}\cdot\nabla\boldsymbol{\tau}) \tag{3.22}$$

are classified into three steps per time step by means of semi-implicit time-stepping procedure as below. This cumulated scheme is known as semi-implicit Taylor-Galerkin pressure-correction finite element method (STGFEM) [11, 79].

This Taylor-Galerkin algorithm is a fractional step method by Taylor series expansion in time. The semi-discretization is applied in the temporal domain. Consequently, a pressure-correction procedure [13] is employed to compute pressure and then it is inserted back to correct velocity in second-order accuracy. A Galerkin finite element method is employed to accomplish this discretization. The flow domain is discretised into a triangular mesh. Each element provides piecewise continuous linear and quadratic interpolation functions for pressure and velocity respectively. The three fractional steps per time step of the Taylor-Galerkin algorithm [67] are:

Step 1a:

$$\frac{2\,\mathrm{Re}}{\Delta \mathrm{t}}(\mathbf{U}^{\mathrm{n}+\frac{1}{2}} - \mathbf{U}^{\mathrm{n}}) = \left[\nabla\cdot\left(\boldsymbol{\tau} + 2\mu_2\mathbf{D}\right) - \mathrm{Re}\,\mathbf{U}\cdot\nabla\mathbf{U} - \nabla\mathrm{p}\right]^{\mathrm{n}} + \nabla\cdot\mu_2(\mathbf{D}^{\mathrm{n}+\frac{1}{2}} - \mathbf{D}^{\mathrm{n}}) \tag{3.23}$$

$$\frac{2We}{\Delta \mathrm{t}}(\boldsymbol{\tau}^{\mathrm{n}+\frac{1}{2}} - \boldsymbol{\tau}^{\mathrm{n}}) = \left[2\mu_1\mathbf{D} - \boldsymbol{\tau} + We\,(\boldsymbol{\tau}\cdot\nabla\mathbf{U} + (\nabla\mathbf{U})^t\cdot\boldsymbol{\tau} - \mathbf{U}\cdot\nabla\boldsymbol{\tau})\right]^{\mathrm{n}} \tag{3.24}$$

where n is the time step index over the interval [n,n+1]. In step 1a, the velocity ($\mathbf{U}^{n}$) and stress ($\boldsymbol{\tau}^{n}$) components at time step n are used to compute for the velocity ($\mathbf{U}^{n+\frac{1}{2}}$) and stress ($\boldsymbol{\tau}^{n+\frac{1}{2}}$) values at the half time step ($n+\frac{1}{2}$).

Step 1b:

$$\frac{\mathrm{Re}}{\Delta t}(\mathbf{U}^{*}-\mathbf{U}^{n})$$

$$=\left[\nabla\cdot(2\mu_2\mathbf{D})-\nabla p\right]^{n}+\left[\nabla\cdot\boldsymbol{\tau}-\mathrm{Re}\,\mathbf{U}\cdot\nabla\mathbf{U}\right]^{n+\frac{1}{2}}+\nabla\cdot\mu_2(\mathbf{D}^{*}-\mathbf{D}^{n}) \qquad (3.25)$$

$$\frac{We}{\Delta t}(\boldsymbol{\tau}^{n+1}-\boldsymbol{\tau}^{n})=\left[2\mu_1\mathbf{D}-\boldsymbol{\tau}+We\,(\boldsymbol{\tau}\cdot\nabla\mathbf{U}+(\nabla\mathbf{U})^{t}\cdot\boldsymbol{\tau}-\mathbf{U}\cdot\nabla\boldsymbol{\tau})\right]^{n+\frac{1}{2}} \qquad (3.26)$$

where * is indicative of the intermediate time step. In step 1b, the velocity ($\mathbf{U}^{*}$) at the intermediate time is solved by data gathered at time step n and ($n+\frac{1}{2}$) while the stress components ($\boldsymbol{\tau}^{n+1}$) at the full time step is calculated by accumulated data at step n and ($n+\frac{1}{2}$).

The two step predictor-corrector procedure gives the initial velocity and pressure fields. The non-divergence-free $\mathbf{U}^{n+\frac{1}{2}}$ and $\mathbf{U}^{*}$ fields, corresponding to mass matrix governing equations, are solved by Jacobi iterative method. The same method is used to calculate the stress equation.

Step 2:

$$\nabla^2(p^{n+1}-p^{n})=\frac{2\,\mathrm{Re}}{\Delta t}\nabla\mathbf{U}^{*} \qquad (3.27)$$

The pressure difference ($p^{n+1} - p^n$) over the full time step interval [n,n+1] is solved by using $\mathbf{U}^*$ via a Poisson equation. The pressure component is calculated by a direct Choleski decomposition method.

Step 3:

$$\frac{2\,\mathrm{Re}}{\Delta t}(\mathbf{U}^{n+1} - \mathbf{U}^*) = -(p^{n+1} - p^n) \tag{3.28}$$

Using $\mathbf{U}^*$ and pressure difference ($p^{n+1} - p^n$), the non-divergent velocity field $\mathbf{U}^{n+1}$ is determined by Jacobi iteration. Galerkin weighting is adapted for all constitutive equations by assuming the general SUPG form as discussed below.

Velocity and stress interpolation is accomplished by quadratic basis functions ϕ_j with six-noded triangular elements while pressure interpolation is accomplished via linear basis functions ψ_k over three-noded triangular elements.

$$\left(\tau_{rrj}, \tau_{rzj}, \tau_{zzj}, \tau_{\theta\theta j}\right)^n = \left(\tau_{1j}, \tau_{2j}, \tau_{3j}, \tau_{4j}\right)^n \phi_j \tag{3.29}$$

$$\left(u_{rj}, u_{zj}\right)^n = \left(u_{rj}, u_{zj}\right)^n \phi_j \tag{3.30}$$

$$\left(p_k\right)^n = \left(p_k\right)^n \psi_k \tag{3.31}$$

where index j is associated with vertex and mid-side nodes, whilst k is related only to vertex nodes.

After using equations (3.29)-(3.31), over domain Ω with non-overlapping finite element sub-regions, the fully discrete forms of steps 1-3 become:

Step 1a:

$$\left[\frac{2\,\mathrm{Re}}{\Delta t}\mathbf{M} + \frac{1}{2}\mu_2\mathbf{S}\right](\mathbf{U}^{n+\frac{1}{2}} - \mathbf{U}^n) = \left\{-\left[\mu_2\mathbf{S} + \mathrm{Re}\,\mathbf{N}(\mathbf{U})\right]\mathbf{U} - \mathbf{B}\boldsymbol{\tau}\right\}^n + \mathbf{L}^t p^n \tag{3.32}$$

$$\frac{2We}{\Delta t}\mathbf{M}(\boldsymbol{\tau}^{n+\frac{1}{2}}-\boldsymbol{\tau}^{n})$$

$$=\left[2\mu_1\mathbf{M}(\mathbf{L}+\mathbf{L}^t)-\{\mathbf{M}+We\mathbf{N}(\mathbf{U})\}\boldsymbol{\tau}+We\left\{\mathbf{N}_1(\boldsymbol{\tau})\mathbf{L}+(\mathbf{N}_1(\boldsymbol{\tau})\mathbf{L})^t\right\}\right]^n \quad (3.33)$$

Step 1b:

$$\left[\frac{\mathrm{Re}}{\Delta t}\mathbf{M}+\frac{1}{2}\mu_2\mathbf{S}\right](\mathbf{U}^*-\mathbf{U}^n)=\{-[\mu_2\mathbf{S}+\mathrm{Re}\,\mathbf{N}(\mathbf{U})]\mathbf{U}-\mathbf{B}\boldsymbol{\tau}\}^{n+\frac{1}{2}}+\mathbf{L}^t p^n \quad (3.34)$$

$$\frac{We}{\Delta t}\mathbf{M}(\boldsymbol{\tau}^{n+1}-\boldsymbol{\tau}^{n})$$

$$=\left[2\mu_1\mathbf{M}(\mathbf{L}+\mathbf{L}^t)-\{\mathbf{M}+We\mathbf{N}(\mathbf{U})\}\boldsymbol{\tau}+We\left\{\mathbf{N}_1(\boldsymbol{\tau})\mathbf{L}+(\mathbf{N}_1(\boldsymbol{\tau})\mathbf{L})^t\right\}\right]^{n+\frac{1}{2}} \quad (3.35)$$

Step 2:

$$\frac{\Delta t}{2\,\mathrm{Re}}\mathbf{K}(p^{n+1}-p^n)=-\mathbf{L}\mathbf{U}^* \quad (3.36)$$

Step 3:

$$\frac{2\,\mathrm{Re}}{\Delta t}\mathbf{M}(\mathbf{U}^{n+1}-\mathbf{U}^*)=\mathbf{L}^t(p^{n+1}-p^n) \quad (3.37)$$

where variables at time t^n are velocity ($\mathbf{U}^n$), stress ($\boldsymbol{\tau}^n$) and pressure (p^n), $\mathbf{U}^*$ is an intermediate non-solenoidal nodal velocity vector, **M** is mass matrix, **S** is momentum diffusive matrix, **K** is pressure stiffness matrix, **N** is advection matrix and **L** is divergence/pressure gradient matrix.

In matrix notation, the variables are

$$\mathbf{M}_{ij}=\int_{\Omega}\phi_i\phi_j d\Omega$$

$$\mathbf{N}(\mathbf{U})_{ij}=\int_{\Omega}\phi_i\phi_l\mathbf{U}_l\nabla\phi_j d\Omega$$

$$\mathbf{N}_1(\boldsymbol{\tau})_{ij} = \int_{\Omega} \phi_i \phi_l \boldsymbol{\tau}_l \phi_j d\Omega$$

$$\mathbf{K}_{mn} = \int_{\Omega} \nabla \psi_m \nabla \psi_n d\Omega$$

$$\mathbf{L} = (\mathbf{L}_1, \mathbf{L}_2)$$

$$(\mathbf{L}_1)_{in} = \int_{\Omega} \psi_n \frac{\partial \phi_i}{\partial r} d\Omega$$

$$(\mathbf{L}_2)_{in} = \int_{\Omega} \psi_n \frac{\partial \phi_i}{\partial z} d\Omega$$

$$\mathbf{S} = \begin{bmatrix} S_{11} & S_{12} \\ S_{12}{}^t & S_{22} \end{bmatrix}$$

$$(S_{11})_{ij} = \int_{\Omega} \left\{ 2 \frac{\partial \phi_i}{\partial r} \frac{\partial \phi_j}{\partial r} + \frac{\partial \phi_i}{\partial z} \frac{\partial \phi_j}{\partial z} + \frac{\phi_i \phi_j}{r^2} \right\} d\Omega$$

$$(S_{12})_{ij} = \int_{\Omega} \frac{\partial \phi_i}{\partial r} \frac{\partial \phi_j}{\partial z} d\Omega$$

$$(S_{22})_{ij} = \int_{\Omega} \left\{ \frac{\partial \phi_i}{\partial r} \frac{\partial \phi_j}{\partial r} + 2 \frac{\partial \phi_i}{\partial z} \frac{\partial \phi_j}{\partial z} \right\} d\Omega$$

$$\mathbf{B} = \begin{bmatrix} B_1 - B_3 & B_2 & 0 & B_3 \\ 0 & B_1 & B_2 & 0 \end{bmatrix}$$

$$(B_1)_{ij} = \int_{\Omega} \phi_i \frac{\partial \phi_j}{\partial r} d\Omega$$

$$(B_2)_{ij} = \int_{\Omega} \phi_i \frac{\partial \phi_j}{\partial z} d\Omega$$

$$(B_3)_{ij} = \int_{\Omega} \frac{\phi_i \phi_j}{r} d\Omega$$

where $d\Omega = rdrdz$, i, j, $l = 1,2,3$, m, $n = 1,2$

The partial differential equations (3.32)-(3.37) are discretised with FDM and FEM. The left for time derivative term is expanded by Taylor series and the right for spatial component is adopt weight residual of Galerkin finite element method so the equations of steps (1)-(3) are converted to the system of linear equations. The geometrical region of flow is designed to a network of small triangular elements in order to get the precise solution before approximate solution is solved with Jacobi iterative method for steps 1 and 3, and Cholesky decomposition for step 2.

3.3 Solving System of Linear Equations

In computational fluid dynamic, linear equation system is generated from discretization of the Navier-Stokes equation describing incompressible fluid flow. For finding the root of equation system, direct method and iterative method are employed. The direct methods utilize a finite sequence of operations to solve solution and these methods would deliver an exact solution such as Gaussian elimination and Cholesky decomposition. In contrast, iterative methods, which are useful to solve nonlinear equations, start initial guess set to generate approximated solution such as Jacobi and Gauss-Seidel iteration methods. In addition, iterative methods are effective for linear problems involving a large number of variables, where direct methods maybe use a large memory that is the cause to waste computer time and storage.

The general form of the linear equations is

$$\mathbf{A}\mathrm{X} = \mathrm{B} \tag{3.39}$$

where $\mathbf{A}$ is a global coefficient matrix, X is the global solution vector and B is the right hand side constant vector composing of an equal number of components to that of the velocity multiple vector.

3.3.1 Jacobi Iteration

A Jacobi iterative scheme [80] is employed to solve velocity and stress solution of governing and constitutive equations. The sequence of solution vector $X^{(k)}$ for the matrix equation can be generated as:

$$\mathbf{D}X^{(k+1)} = (\mathbf{D}\text{-}w\mathbf{A})X^{(k)} + w\mathrm{B} \tag{3.40}$$

where w is a positive relaxation factor and **D** is a chosen diagonal matrix.

Taking into account limits on both sides of (3.40), convergence of step 1 and 3 for X yields the matrix equation solution for that particular iteration is

$$\mathbf{D}X = (\mathbf{D}\text{-}w\mathbf{A})X + w\mathrm{B} \tag{3.41}$$

When $w = 1$, this scheme is called the conventional Jacobi scheme appears. For $w > 1$, extrapolated Jacobi iteration is appeared. The iteration is governed by the iteration matrix ($\mathrm{I}\text{-}w\mathbf{D}^{-1}\ \mathbf{A}$) and this method is symmetrisable. The iteration is possibly convergent when the spectral radius of the iteration matrix is less than unity. This condition is satisfied if the diagonal matrix **D** is the row sum modulus of **A**:

$$d_{ii} = \sum_{j=1}^{A_e} \left| A_{ij} \right| \tag{3.42}$$

3.3.2 Choleski Decomposition

Choleski decomposition [80] is direct method for solving linear equation system. First, a symmetric positive-definite matrix is decomposed into a lower triangular matrix and matrix transpose of the lower triangular matrix. The decomposition for the pressure difference in step 2 is

$$\mathbf{L}\mathbf{L}^{\mathrm{T}} = \mathbf{A} \tag{3.43}$$

where **A** is the positive definite banded symmetric matrix that relates to the stiffness **K** in equation (3.36) and **L** is a real non-singular lower triangular matrix.

Finding the solution of the equation set **A**X=B, it can be solved for X by the forward substitution and for Y by the backward substitution as equations (3.44) and (3.45), respectively.

$$\mathbf{L}Y = B \tag{3.44}$$

$$\mathbf{L}^T X = Y \tag{3.45}$$

3.4 Gradient Recovery

The gradient recovery is a prominent scheme for improving the velocity gradient fields to fit the outcome more precisely with experiment especially for solving highly elastic constitutive model. Normally, the calculation without gradient recovery is inaccurate since elastic stress values are high while the velocity values are low and both effects disturb the stability and accuracy. Many global and local techniques [81, 82] can be captured smooth ∇u each time step in the finite element discretization. The gradient approximations are generated at the element level and the continuous values are cooperative with all variables such as velocity, pressure, and stress.

Gradient recovery scheme is operated over nodal gradient values per element. Hence, direct averaging provides unique values around that the quadratic continuous interpolation is based. The local direct method is based on the average of the nodal finite element gradient components from triangular elements and the velocity gradient component is produced at each local element. The advantages are local compact properties and abstaining from large matrix storage. For example this gradient recovery scheme is selected by Matallah et al. [83]. For each quadratic triangular element, Levine [84, 85] has shown that the average of gradient values give superconvergent values at the mid-side node for quadratic interpolation. The global method is suitable for a set of nodal gradient values to complete the system that the weight residual formation based on the rate of deformation tenser (**D**) with a quadratic interpolation.

Velocity gradient is expressed as:

$$G_k^e(x,t) = \frac{\partial u^h(x,t)}{\partial x_k} \tag{3.46}$$

where $k = 1,2$.

$u^h(x,t)$ is the approximate velocity vector $u(x,t)$ by finite element interpolation on each element:

$$u^h(x,t) = \sum_{j=1}^{n} \phi_j(x) u_j(t) \tag{3.47}$$

where n is the number of nodes per element.

The velocity gradient is the combination of equations (3.46) and (3.47) as:

$$G_k^{e,h}(x,t) = \sum_{j=1}^{n} \frac{\partial \phi(x)}{\partial x_k} u_j(t) \tag{3.48}$$

3.5 Streamline-Upwind/Petrov-Galerkin Method (SUPG)

In case of no creeping flow, the convective term in the momentum equation affects the Galerkin method by producing some severe problems such as oscillations, singular matrices and the losses of the stability emerge in discretization. For viscoelastic flow, the convection term is dominant at high *We* but stability is low so this problem must be treated.

The Petrov–Galerkin method is employed to obtain approximate solutions of partial differential equations that contain convection terms. First, a one-dimensional advection-diffusion finite element method [86] was implemented and then two-dimensional space [87] was considered. After phenomenon of oscillations from the discretization was appeared obviously, the streamline-upwind Petrov-Galerkin (SUPG) method [75, 76] was introduced to attain accuracy in viscoelastic flows. Upwind approach is generated finite difference and central difference methods. It is

crucial in protecting oscillations of the solution by node-to-node. For first order accuracy, the finite difference method is used to approximate differences of solution values at the upstream and central nodes in the convection term as known as upwind differencing while second order accuracy is given the central differencing techniques. As a key tool to achieve high accuracy, upwind technique is approved for stabilization of the finite element method. In order to approach the convection term under viscoelastic flow, some SUPG constraints [73] has generated. The streamline-upwind/Petrov-Galerkin method will treat consistency to uniform in mesh sizes while the convection acceleration is still operate over Galerkin methods.

The streamline upwinding weighting function (ϕ_i^{SUPG}) is construction from combination of the scalar multiplicative element dependent factor of the advective operator with the Galerkin trial function, as equation (3.49) that ϕ_i^{SUPG} or weighting function is added every term in the differential equation.

$$\phi_i^{SUPG} = \phi_i + \alpha^h \mathbf{U} \cdot \nabla \phi_i \tag{3.49}$$

where α^h is the specification of the spatially dependent scalar parameter.

The SUPG scheme is applied to combination with gradient recovery technique to enhance stability and accuracy of the converge solution.

3.6 Free Surface Location

In industry processing, die-swell is a common phenomenon of polymer extrusion as shown in Figure 3.5. When the polymer melt is forced through a die at the entrance, it swells back as former shape and become solid after exiting the die. It is known as die-swell or extrudate swell so the radius of extrudate is significant.

The swelling ratio (χ) can be represented in term of the proportion between jet radius (R_j) and tube radius (R), or in the expression as:

$$\chi = \frac{R_j}{R} \tag{3.50}$$

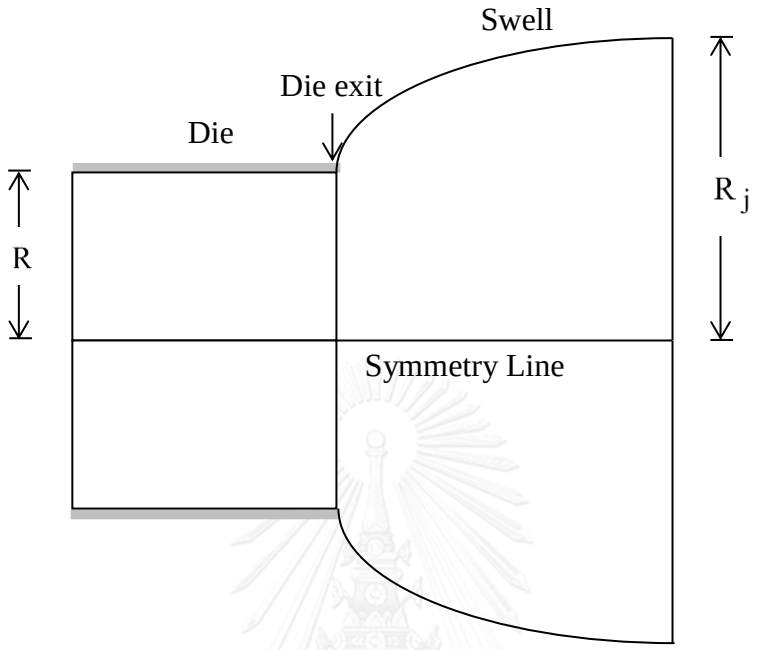

Figure 3.5 Die-swell flow

3.6.1 Streamline Prediction Method

Streamline prediction method is a way to find free surface path that is corresponded to the boundary conditions [88] as equations (3.51)–(3.53). The free surface location of die-swell flow is evaluated from these three conditions by means of streamline prediction method.

$$u_r n_r + u_z n_z = 0 \tag{3.51}$$

$$t_r n_r + t_z n_z = S\left(\frac{1}{\rho_1} + \frac{1}{\rho_2}\right) \tag{3.52}$$

$$t_r n_z - t_z n_r = 0 \tag{3.53}$$

where u_r is radial velocity, u_z is axial velocity, (n_r, n_z) is component of the unit normal to the free surface, (t_r, t_z) is component of the surface force normal to the surface, (ρ_1, ρ_2) is principal radii of curvature and *S* is surface tension coefficient.

The distance (R) from the axis of die symmetry to free surface path is computed by composite Simpson's rule as shown in Figure 3.6 or three-point Newton-Cotes quadrature rule as equations (3.54-3.56).

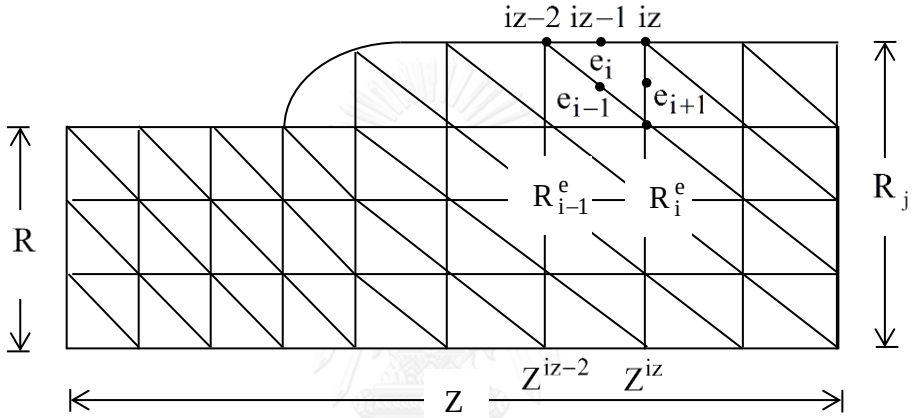

Figure 3.6 Die-swell geometry

$$R_j = R + \int_{z=0}^{\infty} \frac{u_r(z)}{u_z(z)} dz \tag{3.54}$$

where R is die radius.

$$R^{(e)}(z) = R^{(e_{i-1})} + \int_z \frac{u_r^{e_i}(z)}{u_z^{e_i}(z)} dz \tag{3.55}$$

$$\int_z \frac{u_r^{e_i}(z)}{u_z^{e_i}(z)} dz = \frac{h}{6}\left[\frac{u_r^{e_i}(iz-2)}{u_z^{e_i}(iz-2)} + 4\frac{u_r^{e_i}(iz-1)}{u_z^{e_i}(iz-1)} + \frac{u_r^{e_i}(iz)}{u_z^{e_i}(iz)}\right] \tag{3.56}$$

$$h = z^{iz} - z^{iz-2}$$

where h is the length of finite element and e_i is i^{th} element.

3.6.2 Theoretical Prediction

The analytical estimation for elastic fluid under instantaneous elastic strain recovery has been defined by Tanner [89]. The theoretical predictions for adjusting free surface of die-swell can be calculated by

$$\chi = 0.13 + \left(1 + 0.5S_r^2\right)^{\frac{1}{6}}. \tag{3.57}$$

The recoverable shear

$$S_r = \left(\frac{N_1}{2\tau_{rz}}\right)_w \tag{3.58}$$

where N_1 is the first normal stress difference, τ_{rz} is the shear stress and $(\ )_w$ is the evaluated value at the die wall.

For a Poiseuille entry flow and an Oldroyd-B model:

$$N_1 = \tau_{zz} - \tau_{rr} = 2\lambda_1\mu_1\dot{\gamma}^2 \tag{3.59}$$

$$N_2 = \tau_{rr} - \tau_{\theta\theta} = 0 \tag{3.60}$$

$$\tau_{rz} = (\mu_1 - \mu_2)\dot{\gamma}, \tag{3.61}$$

so that

$$S_r = \frac{\lambda_1\mu_1\dot{\gamma}_w}{\mu_1 + \mu_2} = \beta We \tag{3.62}$$

$$\beta = \frac{\mu_1}{\mu_1 + \mu_2} \tag{3.63}$$

$$We = \lambda_1\dot{\gamma}_w \tag{3.64}$$

where $\dot{\gamma}_w$ is shear rate at the die wall.

Tanner [41] has presented the swelling ratio R of Newtonian fluid that are $\chi = 1.190 \pm 0.002$ and $\chi = 1.127 \pm 0.003$ within planar and axisymmetric coordinate systems, respectively.

3.7 Surface Solution Reprojection

In order to satisfy the zero normal velocity, the adjustment of the free surface path is set to correspond with three boundary conditions and the nodal points after the die exit at free surface are adjusted. Hence, the velocity solution at each nodal coordinate must be projected onto the new position. A way how to find the new surface position for each element is demonstrated in Figure 3.7. Two sampling points (r_1, z_1) and (r_2, z_2) is considered at the mid-side and vertex node positions respectively.

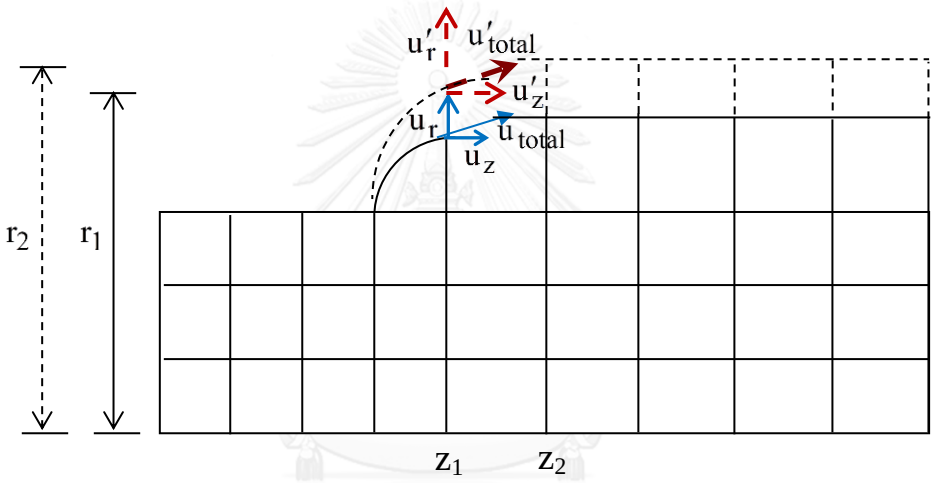

Figure 3.7 Free surface adjustment

The velocity magnitude (u_{total}) on an element is

$$u_{total} = \sqrt{u_r^2 + u_z^2} \tag{3.65}$$

For the estimation of new free surface position, the angle α between the boundary and the horizontal z is

$$\alpha = \tan^{-1}\left(\frac{r_2 - r_1}{z_2 - z_1}\right) \tag{3.66}$$

The updated u'_r and u'_z velocity components are derived through the projection**:**

$$u'_r = u_{total}\sin(\alpha) \tag{3.67}$$

$$u'_z = u_{total}\cos(\alpha) \tag{3.68}$$

3.8 Error Norm

To consider convergence of the finite element solution, the termination of a numerical program is determined from an error norm with the following criteria.

The L_2 relative error norm or relative square-norm is

$$\frac{\sqrt{\sum_{i=1}^{N}\left(\mathbf{X}_i^{n+1}-\mathbf{X}_i^{n}\right)^2}}{\sqrt{\sum_{i=1}^{N}\left(\mathbf{X}_i^{n+1}\right)^2}} \tag{3.69}$$

L_2 is possible as a root mean square measure between successive time steps. N is number of node. $\mathbf{X}_i^{n+1}$ and $\mathbf{X}_i^{n}$ are the solution value for time step n+1 and n, respectively.

The L_∞ relative error norm or relative infinity-norm is

$$\frac{\left\|\mathbf{X}^{n+1}-\mathbf{X}^{n}\right\|_\infty}{\left\|\mathbf{X}^{n+1}\right\|_\infty} \tag{3.70}$$

L_∞ is the maximum relative difference between the time increments. $\mathbf{X}^{n+1}$ and $\mathbf{X}^{n}$ are the solution for time step n+1 and n. For this computation, $L_2 \le \varepsilon$ and $L_\infty \le \varepsilon$, where ε is the degree of error that is a small value.

3.9 Feedback of Pressure-Driven Velocity Flow

To force pressure and velocity at inlet with suitable boundary, the feedback concept is stipulated for picking upstream solution at the same vertical nodes in order to return values back in entry border. For example how to choose nodes of Figure 3.8, the possible column can be nodes in C2, C3, C4 and C5 so if we choose C3 then the values of pressure and velocity of nodes 9, 10, 11 and 12 will be the initial condition for nodes 1, 2, 3 and 4, respectively. The differential time step at the beginning is set bigger than the later calculation since the computation of large different time step makes solution jump to converge but it might be over leap to diverge immediately so this is the reason to gradually reduce the differential time step by 10-1 after the error of outcome was stepped down at the same rate of 0.1. Every cycle of adjustment for the time step occurred simultaneously with the feedback of the pressure-driven velocity flow [35] to drive the solution in good agreement with the experimental and analytical results. The flowchart of this procedure is described in Figure 3.9, which can be executed rapidly for abrupt contraction problem to save time and assure convergent solution so the application of FPDVF adjusts the entrance boundary condition precisely especially for pressure and velocity even if the first round of calculation shoots the result far away.

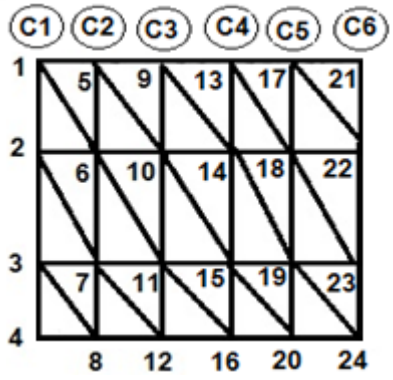

Figure 3.8 Mesh geometry with node number, FPDVF.

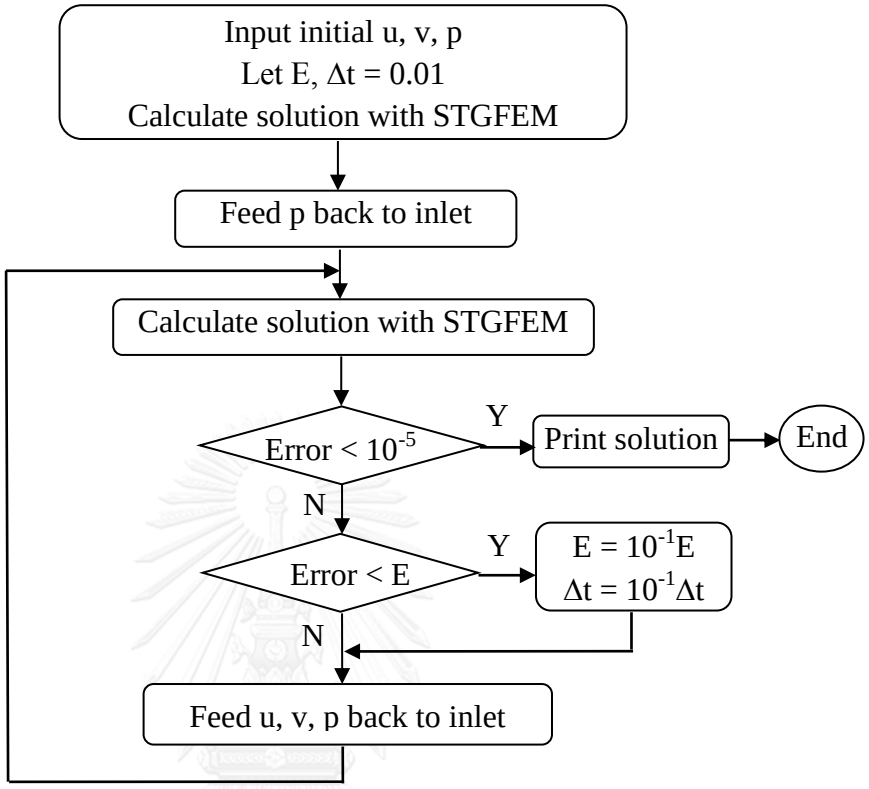

Figure 3.9 FPDVF algorithm

3.10 Phan-Thien Slip Rule

To reduce shear stress at sharp corner point, Phan-Thien [32] has introduced the slip velocity at solid wall by setting and expressing the particle speed as a function of wall shear stress to make solution more accurate and closer to the experimental outcome. The slip velocity will be calculated if some values of wall shear stress are greater than a constant critical shear value. This desired function is of the form

$$u_{slip} = u_{mean}\left[1 - \exp\left(-\alpha \frac{\tau_w}{\tau_{crit}}\right)\right] \tag{3.71}$$

where u_{slip} is the slip velocity, u_{mean} is the mean velocity flowrate for no-slip case, α is the constant slip coefficient, τ_w is the wall shear stress and τ_{crit} is the critical shear stress.

For convenience to calculate the shear stress (τ_{xy}) of Oldroyd-B fluid, Johnson and Segalman [90] have applied shear stress as a function of shear viscosity (η) and shear rate ($\dot{\gamma}$) on the basis of the kinematic theory of macro-molecules.

$$\tau_{xy} = \frac{\eta_1 \dot{\gamma}}{1 + a(2-a)(\lambda_1 \dot{\gamma})^2} + \eta_2 \dot{\gamma} \tag{3.72}$$

where η_1 and η_2 are viscosity coefficients and a is a scalar parameter between $(0,2)$.

CHAPTER 4
4:1 CONTRACTION FLOW

This research mainly concerns on the application of slip effect for Newtonian fluid and Oldroyd-B constitutive model in 4:1 contraction flows. The finite element method is applied for solving the Newtonian fluid through the abrupt 4:1 contraction channel of rounded corner geometries. After the computation of STGFEM for each time step was completed, the feedback of pressure-driven velocity flow is forced to modify the inlet boundary.

The kinematic behavior of flow is observed from streamline path, shear stress value and vortex size with a models of Navier-Stokes equations in two-dimensional planar isothermal incompressible creeping flow with no-slip condition. After the problem encountered with oscillation and solution diverges to infinity, the treatment of drag pressure is brought to keep outcome going to the right way. Then pressure driven condition at inlet boundary is enforced each time step to achieve the accurate result and made the outcome more secure. The solution was first calculated with the method of semi-implicit Taylor-Galerkin pressure-correction scheme before the treatment of streamline-Upwind/Petrov-Galerkin and velocity gradient recovery are employed to confirm the stability. The comparison of velocity for each mesh patterns before and after treatment of drag velocity is displayed via line and colour contour visualizations. Finally the presentation of line contours for streamline is depicted to reflect the vortex size and the influence of shear stress in 4:1 contraction domains is analyzed and corrected by adding the slip function on the boundary of channel wall.

The 4:1 contraction flow is a well know problem to discover kinematic behavior of viscoelastic flows whilst flow path has sudden change in the kind of this geometry especially for two-dimensional system. There are strong elongation and violent shear stress at contraction position. The severe stresses were noticed in experimental work [91] by measuring the rheological properties of viscoelastic fluids past an abrupt 2:1 contraction from rheogoniometer, which gave the less significant results when compared with numerical prediction of power-law model. Another trial record [92] of

pressure drop and normal stresses for low Reynolds numbers in capillary and slit method was investigated but this experimental data was insufficient to calculate normal stresses due to establishment of error. In addition, one analyzing test [19] for Boger fluids to inspect the behavior of pressure-flow rate was illustrated with various contraction geometries. Those preparatory experiments did not yield any important trend. In order to reduce cost and time for trial and error, the numerical simulation by getting input of characteristic parameters from experiment was set for both Newtonian and non-Newtonian fluids [20]. The circular contraction flow with adequate constitutive equation was predicted possibly in the direction of good basic flow property measurements.

To avoid complex analytic solution, the simulation in the mathematical model for the nonlinear partial differential equations that derived from conservation of mass and momentum are set up to eliminate hard solving problem so the numerical techniques and employed to calculate approximate solution. There are a variety of numerical methods such as finite element method (FEM), finite volume method (FVM) and finite difference method (FDM). A 4:1 planar contraction of Oldroyd-B fluid for creeping and inertial flows [9] has been solved with semi-Lagrangian FVM and it [10] had recalculated for new axisymmetric flow but the grids were fixed in Eulerian methods. The technique of a cell-vertex hybrid finite volume/element method [8] is suitable to compute highly elastic solutions for Oldroyd-B model and Phan-Thien/Tanner (PTT) fluid [93]. The complex flow via PTT model was included to extend the limit of Weissenberg number for both rounded and sharp corner contraction figures. Many scientists interested in viscoelastic flow past planar abrupt contractions. The significance of contraction ratios [26] and Deborah numbers concept was explored for a function of flow characteristics.

There are a number of problems that were widely solved by FEM in addition to this thesis. The stick-slip flow [67] of Oldroyd-B model was adopted with the same standard FEM and free surface effect was added to develop this flow to become die-swell problem; furthermore, swelling ratio is varied as a function of relaxation time. Such a case of this short die is a simple example that is taken from full dies, that are pressure- [12] and tube- [94] tooling wire-coating dies, in the small section before die

exit. These complete long dies show the complex geometries when the finite mesh is generated so the computation is more complicated. A new scheme to improve solution of Oldroyd-B problem via sub-cell finite element approximation [68] was applied by means of discretization technique in order to interpolate cooperative stress and flow field through finite volume/finite element method for cavity and contraction flows. This scheme was still maintaining stability and second-third order accuracy. After the solutions for time which are independent of viscoelastic problems were revealed, many enthusiastic researchers turned their attention to flow movement with time to make the visualization more realistic. The transient solution [69] for polymeric liquid flow in 4:1 planar rounded corner with a hybrid finite element/finite volume scheme was considered in flowrate control, transient flowrate control, and force-driven control. Afterwards, the investigation [14] of rheological properties for various schemes is considered in cross-slot devices though FV/FE pressure correction method.

Since the difference between experiment and numerical solution for fluid flows through hard wall is significant so the study of fluid particle speed on solid surface is determined by means of slip effect. In order to approve the solution of Newtonian and viscoelastic flow on free surface [29], slip condition is introduced to adjust velocity at die wall. The result after adding the conditions of slip velocity gives well value that can get along with the experiment [30], focusing on surface melt fracture of HDPE and LLDPE. Previously, two slip cases were considered. One was supported strongly with analysis solution by setting slip velocity [31] for capillary tubes as a function of wall shear stress and two is Phan-Thien slip rule [32] which manifests the same concept of slip velocity. However, slip velocity still notices obviously when the critical shear stress is less than wall shear stress.

The annular tube-tooling and pressure-tooling wire-coating flows [33] of the Newtonian fluid were considered with free surface effect that causes flow swell to cover wire and the effects of slip at die-walls to mitigate stress singularities at die exit. The positive result of feedback pressure-driven velocity flow [34] has been presented for the Newtonian fluid through the abrupt 4:1 contraction flow of rounded corner geometry.

In this research, the slip effect and treatment schemes are considered in the problem of 4:1 sharp contraction for Newtonian and Oldroyd-B fluids under the two-dimensional planar isothermal incompressible flow and formed the mathematical model of Navier-Stokes and Oldroyd-B equations. The velocity gradient recovery and the streamline-upwind Petrov/Galerkin (SUPG) techniques are chosen to stabilize the converge solutions without the slip condition. The converge solution after drag velocity at inlet boundary is rectified and revealed that pressure forces velocity drive as parabolic motion and makes solution smoothly stable. Finally, the solutions are considered with and without the slip condition by means of Phan-Thien slip rule, which is a relation between shear stress and velocity at wall. The stress value and vortex size of slip condition were compared with Johnson and Segalman model [90]. After the slip function is added to reduce the shear stress at the channel wall. The appropriated slip velocity which is considered at the wall between sharp corner and rounded corner are compared to summarize the effects of the slip condition.

4.1 Governing Equations

An incompressible laminar flow of the Newtonian liquid passes through a 4:1 contraction that entails the solution of the mass conservation under non-gravity and the motion is preserved in Navier-Stokes equations. The non-dimensional system is normalized to benchmark with other literatures as a result of a standard form. The continuity and kinematic equations are equations (2.10) and (2.28), respectively. In this research, creeping motion is determined as $\mathrm{Re} = 0$.

4.2 Numerical Scheme

The nonlinear differential equations are normally solved by numerical method as same as this problem, which is manipulated by basic FEM. The momentum equation (2.10) and the stress equation (2.28) of Oldroyd-B model is computed by STGFEM that is a scheme for providing the nonlinear equation into three time stages and each stage is discretised to system of linear equations. To extend this work, the slip velocity is evaluated with Phan-Thien slip rule for 4:1 contraction problem. The result

of Newtonian fluid in rounded corner shape is retreated by feedback of pressure-driven velocity flow.

4.2.1 Semi-implicit Taylor-Galerkin Pressure-Correction Finite Element Method

The fractional steps are provided to split non-dimensional equation (2.10), (2.11) and (2.28) for three stages per time step so it was predicting velocity first before the calculation of pressure and then the pressure was the feedback to recalculate the correct velocity. Finally, the FEM is employed to separate the continuous equations via a system of linear equations. As such, this convenient technique is known as semi-implicit Taylor-Galerkin pressure-correction finite element method as shown below.

To divide partial differential equations (2.10), (2.11) and (2.28) with FDM and FEM, The derivative term of time is generated by the Taylor series and the weight residual of Galerkin finite element method is applied in the spatial phases to classify the equations as stages (3.32)-(3.37) and then transform to the system of linear equations. Steps 1 and 3 are solved with Jacobi iterative whilst step 2 is approximated by Cholesky decomposition algorithm.

4.2.2 Feedback of Pressure-Driven Velocity Flow of 4:1 Contraction Flow

Feedback concept, which is a way to make solution and jump into the outcome immediately, is taken to avoid the diverged solution. This technique forces pressure and velocity at inlet boundary be suitable for initial condition. The numerical solutions are considered at the same vertical nodes in order to bring trial values back to the entry nodes. In Figure 4.1, the neighborhood columns of entry column (C1) are between in columns 2 (C2) and column 5 (C5). If C3 is selected, the values of pressure and velocity in this column will be set for the initial condition at C1. Every loop of time step reduces 0.1 step by step until the difference of the boundary condition is satisfied.

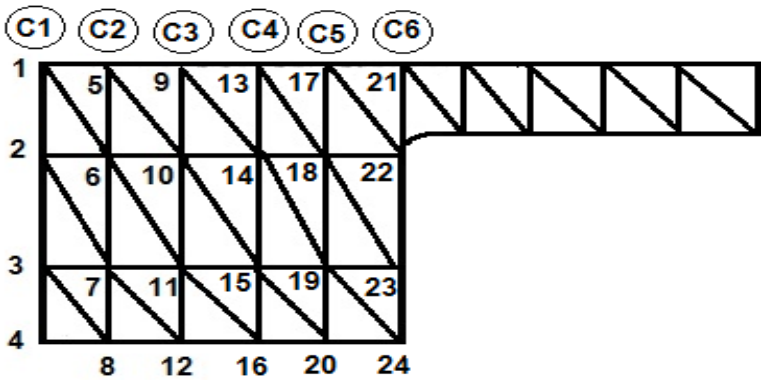

Figure 4.1 Mesh geometry with node number, 4:1 contraction flow

4.2.3 Phan-Thien Slip Rule

To fit the slip velocity, Phan-Thien [32] has demonstrated the concept of slip velocity as a function of wall shear stress that is close to experimental solution. This scheme is helpful to reduces shear stress for abrupt contraction, and consequently the slip velocity will be calculated when the wall shear stresses are greater than a critical shear stress.

4.3 Problem Specification

For the consideration of slip condition on channel wall, two patterns of 4:1 contraction geometries are considered under sharp and rounded corners. The acute corner or sharp form is shown in Figure 4.2 – Figure 4.4 while the rounded geometry is presented in Figure 4.5 and Figure 4.6. On the consideration of shear effect, the Poiseuille flow is set at entrance within planar coordinate system and the feedback of pressure-driven velocity flow is taken to stabilize the approximated solution of the Newtonian and Oldroyd-B fluids.

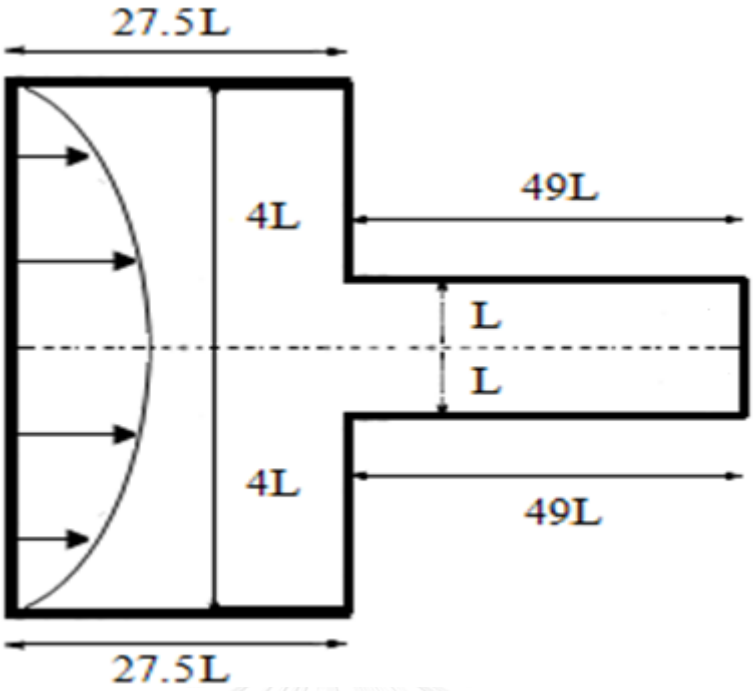

Figure 4.2 4:1 shape contraction flow

4.3.1 Sharp Corner of 4:1 Contraction Problem

There is a benchmark of slip and no slip cases in the same geometrical domain for 4:1 contraction flow that is normally appeared in industrial processes so the major body is picked in the model of sharp corner shape. Since the top and bottom parts are identical, the bottom portion as show in Figure 4.3 is selected to display all solutions. The geometry of the half channel width L at entry and exit sections are 27.5L and 49L respectively.

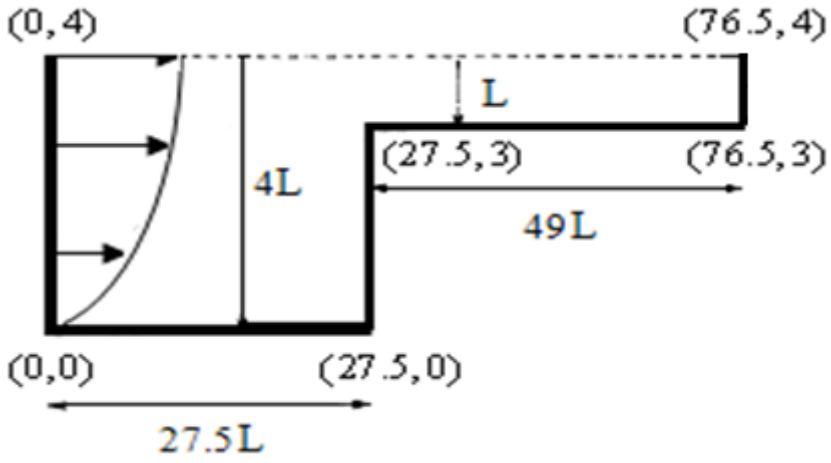

Figure 4.3 Schematic diagram of 4:1 shape contraction flow

The inlet length is imposed to Poiseuille flow and fluid passes in channel, which is long enough to complete developing flow so the downstream exit length is still retaining parabolic flow pattern. At the channel wall, the slip condition is applied to gain intensive result close to real problem.

At inlet fully developed flow, the velocity in x direction, which is denoted u_x is varied with distance y that is null at the symmetrical line while normal and shear stresses are function of partial derivative of u hence the initial conditions for entrance boundary are imposed by Equation (4.1).

$$u_x(y) = \frac{3}{128}(16 - y^2) \text{ and } u_y = 0 \qquad (4.1)$$

$$\tau_{xx} = 2We\mu_1\left(\frac{\partial u_x}{\partial y}\right)^2, \tau_{yy} = 0, \text{ and } \tau_{xy} = \frac{\partial u_x}{\partial y}$$

To inspect the severe stress at impact wall, the sharp corner contraction mesh1-mesh4 are considered. These are created in four delicate order grids of very coarse, coarse, medium and fine meshes which were used by Aboubacar et al. [8] as illustrated in Table 4.1 and Figure 4.4. All meshes are bias and the tiny elements (h_{min}) are placed next to the singularity.

Table 4.1 Mesh characteristics of sharp corner geometries

Mesh	Element	Nodes	Degree of freedom	h_{min}
mesh1	980	2105	11088	0.025
mesh2	1140	2427	12779	0.023
mesh3	2987	6220	32717	0.006
mesh4	5140	10575	55593	0.004

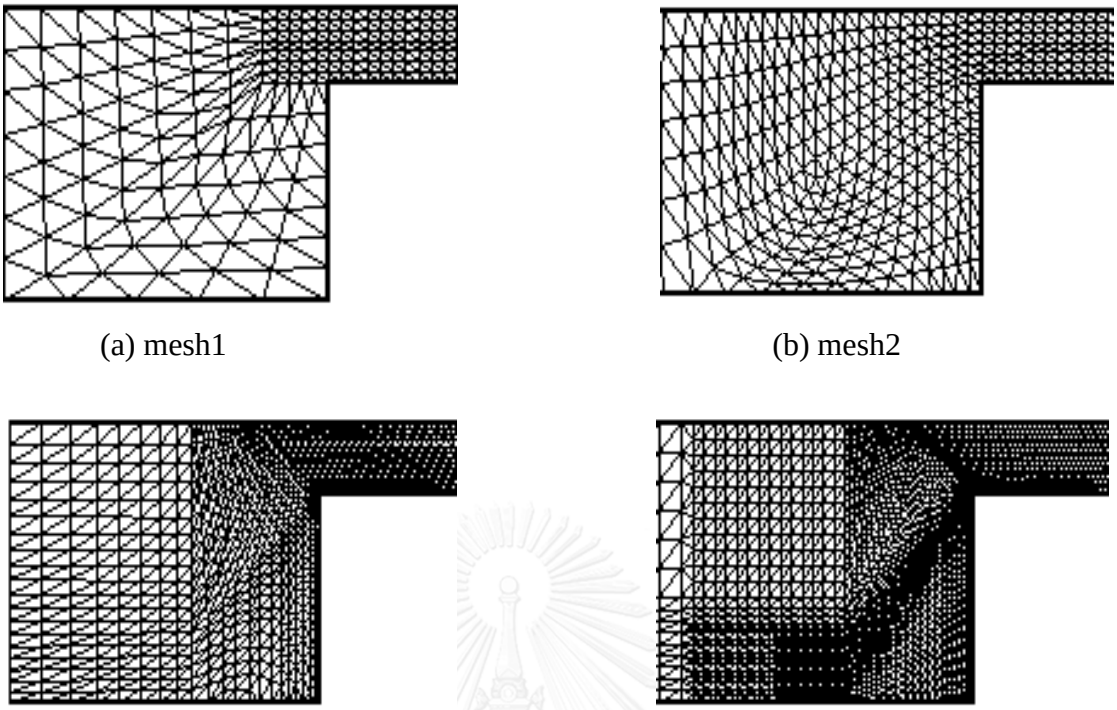

(a) mesh1 (b) mesh2

(c) mesh3 (d) mesh4

Figure 4.4 Sharp mesh pattern of 4:1 contraction flow

4.3.2 Rounded Corner of 4:1 Contraction Problem

In industrial process especially for 4:1 contraction problems when fluid passes through a part of abrupt contraction, the flow character shows that its behavior of shear stress is so violent at the sharp corner points that the geometrical domain of this problem was reduced from acute angle to rounded corner as shown in Figure 4.5. The downstream half channel width of planar 4:1 contraction at entry and exit sections are 27.5L and 49L, respectively. At inlet entry, velocity flow is specified to parabolic motion in channel length which is long enough to develop as Poiseuille flow.

The rounded geometry is designed in curve segment at contraction angle to decrease the severe stress [8, 93] and vortex size while mesh patterns are created for three different styles as shown in Figure. 4.6 for coarse, medium, and fine meshes that are called mesh5, mesh6 and mesh7 respectively. The mesh form of all types as declared

in Table 4.2 is generated into bias triangular element and the tiny elements (h_{min}) are set up near rounded corner.

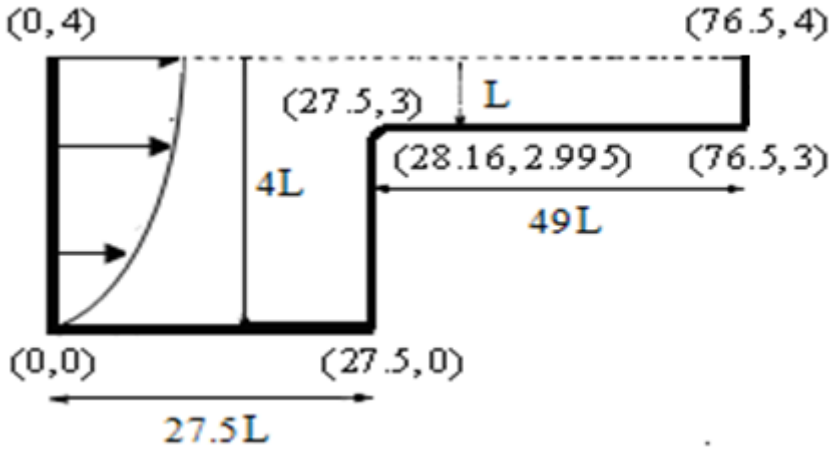

Figure 4.5 Schematic diagram of 4:1 rounded contraction flow

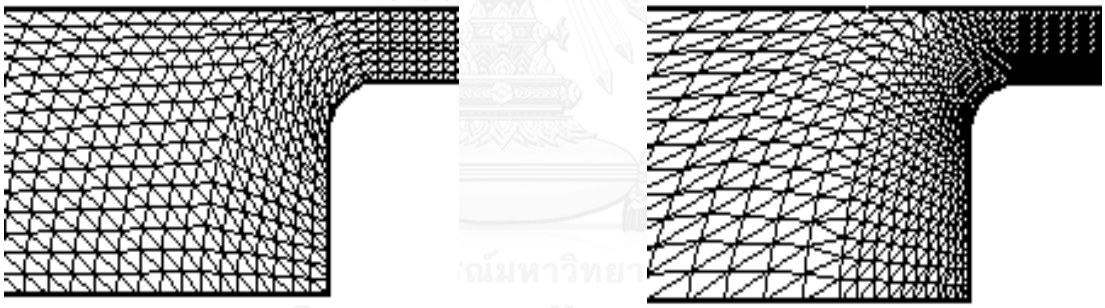

(a) mesh5 (b) mesh6

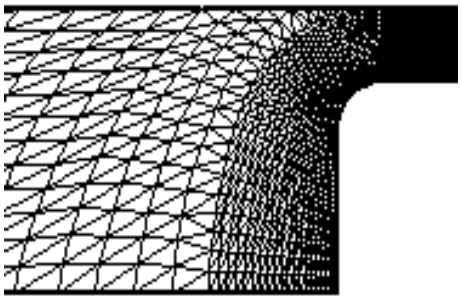

(c) mesh7

Figure 4.6 Mesh pattern of 4:1 rounded corner

Table 4.2 Mesh characteristics of rounded corner geometries

Mesh	**Element**	**Nodes**	**Degree of freedom**	h_{min}
mesh5	1626	3433	18069	0.017
mesh6	2693	5652	29740	0.010
mesh7	4751	9790	51470	0.006

4.4 Results of 4:1 Sharp Contraction Flow

The results of sharp corner meshes are considered and the best mesh is selected to run for final solution in order to reduce duplicate outcome. After optimal mesh was taken, it was brought to run in both Newtonian and viscoelastic fluids under the condition of no slip and slip effect. The slip coefficients for each liquid are determined to adjust the flow pattern as displayed below.

4.4.1 Slip Effect of Newtonian Fluid

The peak values on top downstream wall with no slip of normal stress τ_{xx} and τ_{yy}, shear stress τ_{xy} and shear rate $\dot{\gamma}$ in Table 4.3 and Figure 4.7 grow upon higher sensitivity of grid and it is noticed that the peak of all values can be classified in two groups of resemblance. The results of mesh1 and mesh2 are similar as well as mesh3 and mesh4 but the outcome of second group is prominent.

In order to choose a suitable mesh to get the final solution, the dominant mesh will be selected, that is mesh3 or mesh4. For this case mesh3 is the best choice to prompt display even if mesh4 is fine net structure because the result of mesh3 can be run easier and faster to get converge solution than mesh4 whilst both grids give the little difference so the minor error can be negligible.

Table 4.3 The peak values of Newtonian fluid on top downstream wall with no slip

Mesh	τ_{xx}	τ_{xy}	τ_{yy}	$\dot{\gamma}$
mesh1	9.046	4.523	0.335	4.832
mesh2	9.014	4.507	0.330	4.753
mesh3	12.488	6.244	0.328	6.597
mesh4	15.998	8.000	0.325	8.660

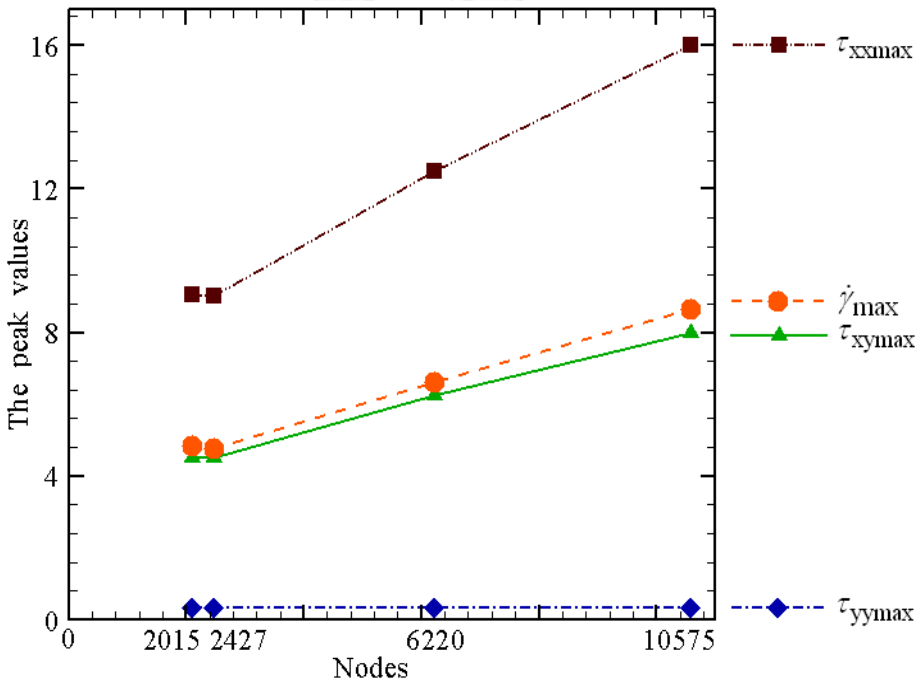

Figure 4.7 The peak values of sharp corner meshes

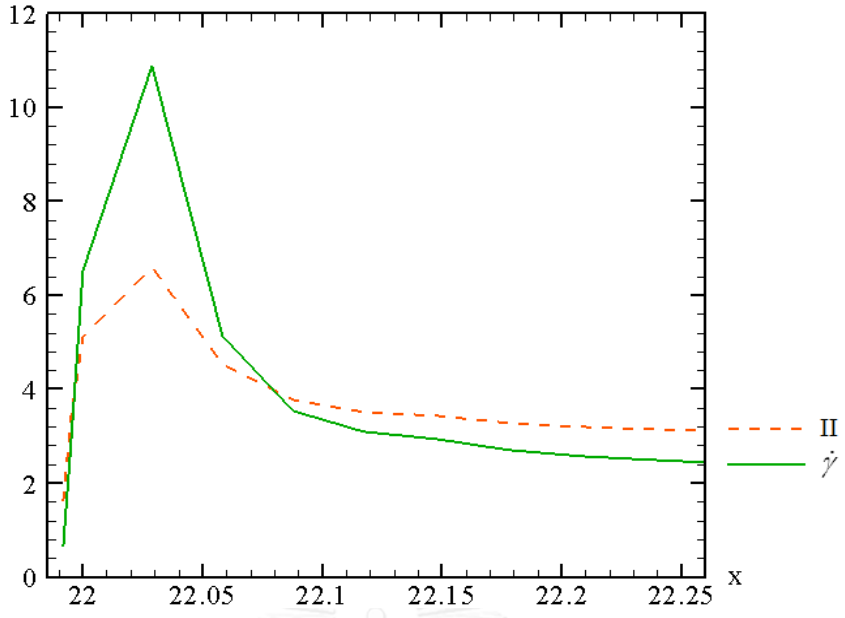

Figure 4.8 II and $\dot{\gamma}$ along top downstream wall with no slip of Newtonian fluid

The similar behavior of second invariant (II) and shear rate ($\dot{\gamma}$) of Newtonian fluid for mesh3 are displayed in Figure 4.8. Both curves for II and $\dot{\gamma}$ look like a left-skewed distribution and the peaks are 10.881 and 6.597 for II and $\dot{\gamma}$, respectively. From the previous work, it was found that all apexes go to singularity in case of high *We* and these values are quite far from physical phenomena so it is the reason why slip condition is determined to reduce the zenith as seen in Figure 4.9.

For choosing the optimum value of α and the critical II (II_{crit}), mesh3 is used to execute the slip effect for Newtonian fluid by running α from 0.1 to 1 as illustrated in Figure 4.9. First round of calculation to find minimum α of fixing $II_{crit} = 2.3$ for α at 0.3, 0.5, and 1 is observed that oscillations appear clearly but $\alpha = 0.1$ is ascertained properly the value of lowest peak $\dot{\gamma}$. This selection of minimum $\dot{\gamma}$ is supported by Figure 4.10 which displays a correlation between $\dot{\gamma}$ and α. Second round of computation to find the location of the critical II by setting $\alpha = 0.1$ and adjusting II from 0 to 10 is operated before relation of $\dot{\gamma}$ versus II_{crit} presents that the lowest II_{crit} points to 2.3 in Figure 4.11.

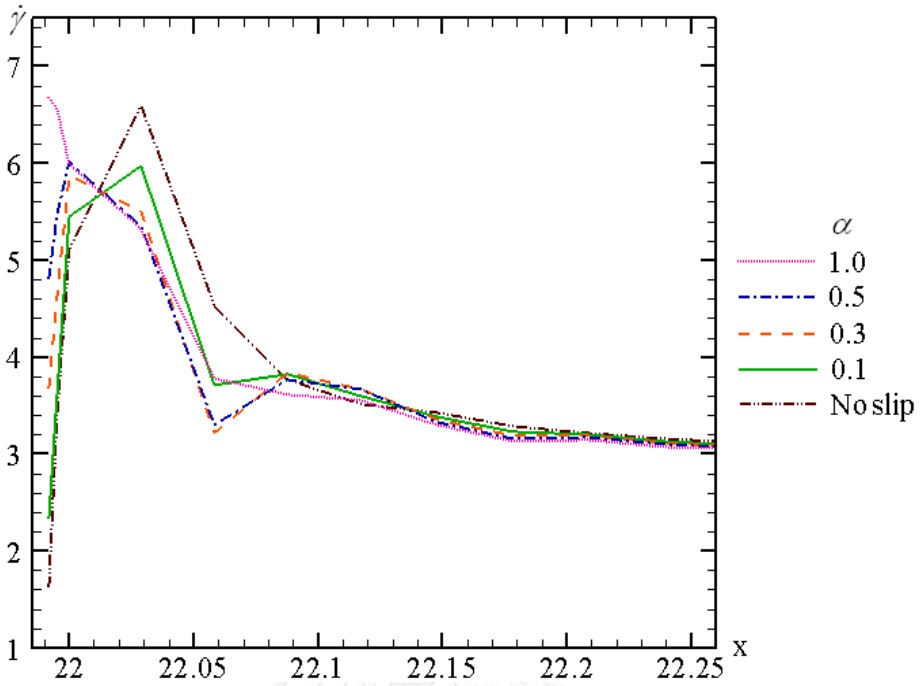

Figure 4.9 $\dot{\gamma}$ of various α along top downstream wall of Newtonian fluid at $\mathrm{II} = 2.3$

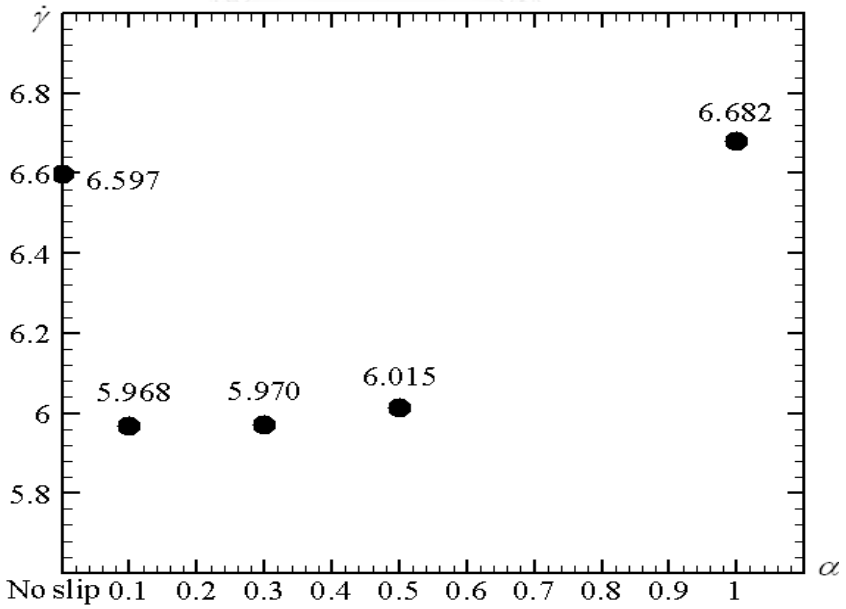

Figure 4.10 The peak of $\dot{\gamma}$ versus α on top downstream wall of Newtonian fluid at $\mathrm{II} = 2.3$

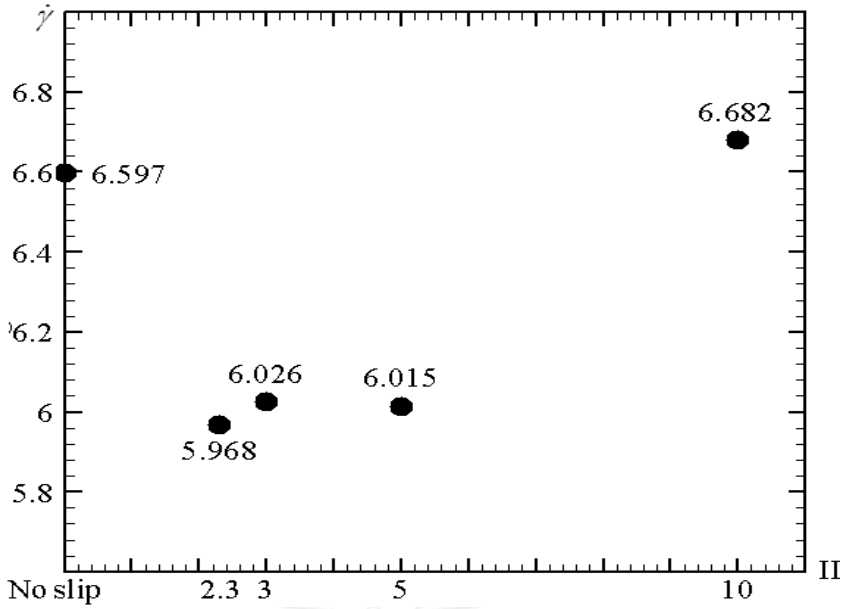

Figure 4.11 The peak of $\dot{\gamma}$ versus $\mathrm{II}_{\mathrm{crit}}$ on top down-stream wall of Newtonian fluid at $\alpha = 0.1$

Figure 4.12 shows streamline (S) line contour for no slip in Figure 4.12(a) and slip effect at $\alpha = 0.1,\ \mathrm{II} = 2.3$ in Figure 4.12(b). Graphs of both cases look similar but the vortex at the corner of no slip is bigger than that of its counterpart in the slip case.

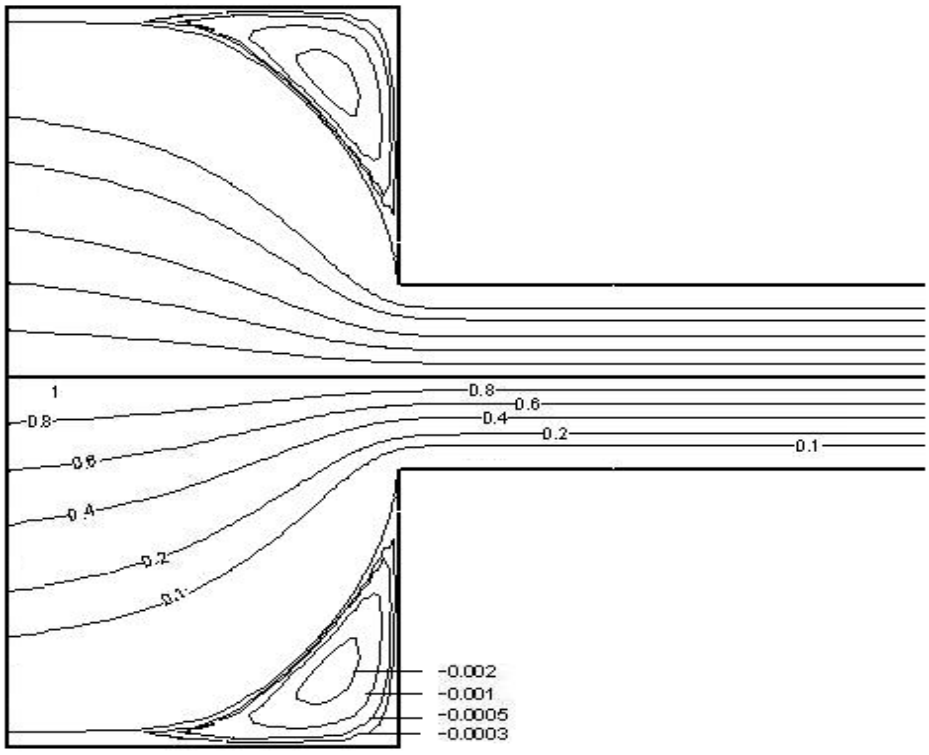

(a) No slip

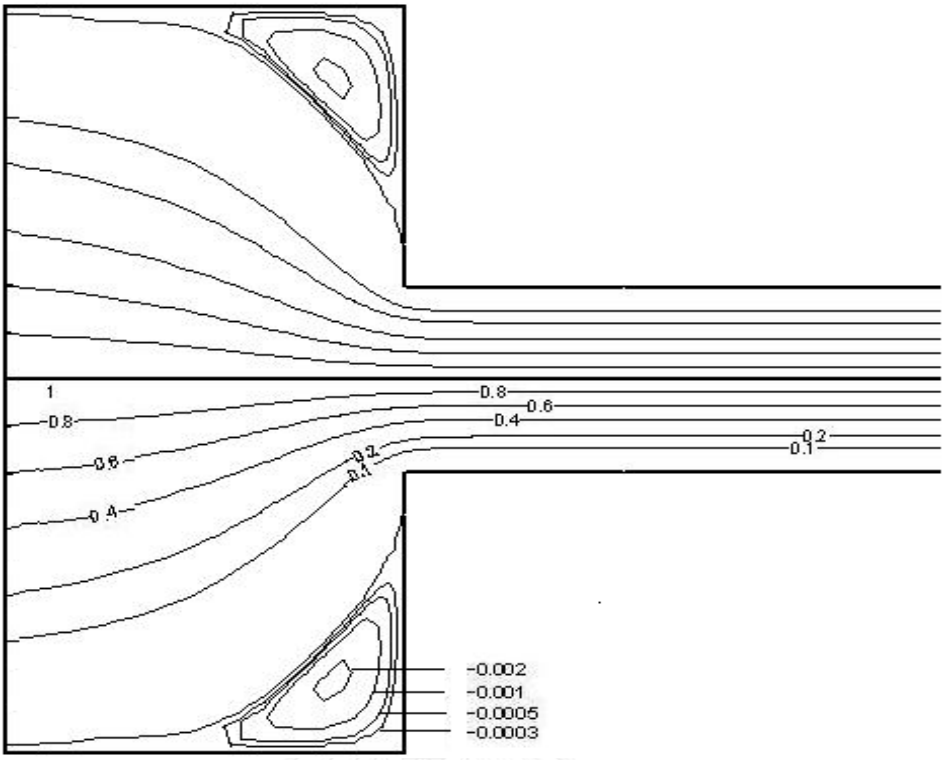

(b) slip at $\alpha = 0.1$ and $\text{II} = 2.3$

Figure 4.12 S line contour of Newtonian fluid

4.4.2 Slip Effect of Oldroyd-B fluid

Comparing the stress values τ_{xx}, τ_{xy} and τ_{yy} of sharp meshes without slip, the stress values of mesh1 and mesh2 are significantly different from mesh3 and mesh4 as illustrated in Table 4.4-4.6. On the observation of the aforementioned tables, it makes clear that the stress outcome of mesh3 is slightly deviated from mesh4.

Table 4.4 The peak value of τ_{xx} along the downstream wall with sharp-corner meshes without slip

We	0.25	0.5	0.75
mesh1	7.973	13.514	19.502
mesh2	8.462	13.920	20.346
mesh3	19.943	29.455	34.042
mesh4	20.142	30.515	35.959

Table 4.5 The peak value of τ_{xy} along the downstream wall with sharp-corner meshes without slip

We	0.25	0.5	0.75
mesh1	5.531	6.101	6.899
mesh2	5.686	6.432	7.516
mesh3	10.411	12.888	14.505
mesh4	12.164	13.980	14.516

Table 4.6 The peak value of τ_{yy} along the downstream wall with sharp-corner meshes without slip

We	0.25	0.5	0.75
mesh1	2.373	2.267	2.451
mesh2	2.682	2.310	2.798
mesh3	5.329	5.569	6.116
mesh4	7.264	7.919	8.189

For all meshes in Table 4.7, the viscoelastic fluids are considered for various values of *We*. The peak values on top downstream wall with no slip of normal stress $\dot{\gamma}$ grow upon high *We* and it is shown that the peak of $\dot{\gamma}$ for all meshes have thrived with the same trend. The results of mesh1 and mesh2 are similar as well as mesh3 and mesh4 but the outcome of second group is prominent. Since the tendency of behavior for all *We* has the same direction, all sharp meshes are presented only $We = 1.0$ for all stresses (τ_{xx}, τ_{xy}, τ_{yy}) with the same condition in Table 4.8. Mesh3 is chosen to run for the final solution for the same reasons stated earlier.

Table 4.7 The peak values of $\dot{\gamma}$ on top downstream wall with no slip of Oldroyd-B fluid

Mesh	0.25	0.5	0.75	1
mesh1	4.873	5.130	5.323	5.717
mesh2	4.929	5.061	5.153	5.510
mesh3	7.534	8.550	8.828	9.209
mesh4	8.833	9.380	9.504	10.234

Table 4.8 The peak values of τ_{xx} , τ_{xy} and τ_{yy} on the top downstream wall with no slip of Oldroyd-B fluid at $We = 1.0$

Mesh	τ_{xx}	τ_{xy}	τ_{yy}
mesh1	21.458	7.236	2.507
mesh2	22.512	8.047	3.018
mesh3	36.571	15.496	6.427
mesh4	37.670	15.068	8.772

To select critical II from Figure 4.13, the optimum α for $We = 0.25$ is considered before calculation of high We. All α values are varied from 0.1 to 1 by first given $\text{II} = 14$ because the shear rate is high enough to switch some stick velocities to move freely. For choosing proper α by minimizing shear rate, the same procedure of Newtonian case is operated as seen in Figure 4.14 so the minimum shear rate is 7.530 at $\alpha = 0.1$ that is under the value of no slip condition while the other value of α has exceeded over the value of slip case. Other α values are rejected except $\alpha = 0.1$ since the slip velocity decreases shear rate. By adjusting critical II, the range of II is started at 5 to 14 since the off range cannot be calculated for $\alpha = 0.1$ but the range II that is shown in Figure 4.15 and the least value shear rate for $\text{II} = 6$ is 7.175; therefore, the suitable coefficient slip is 0.1.

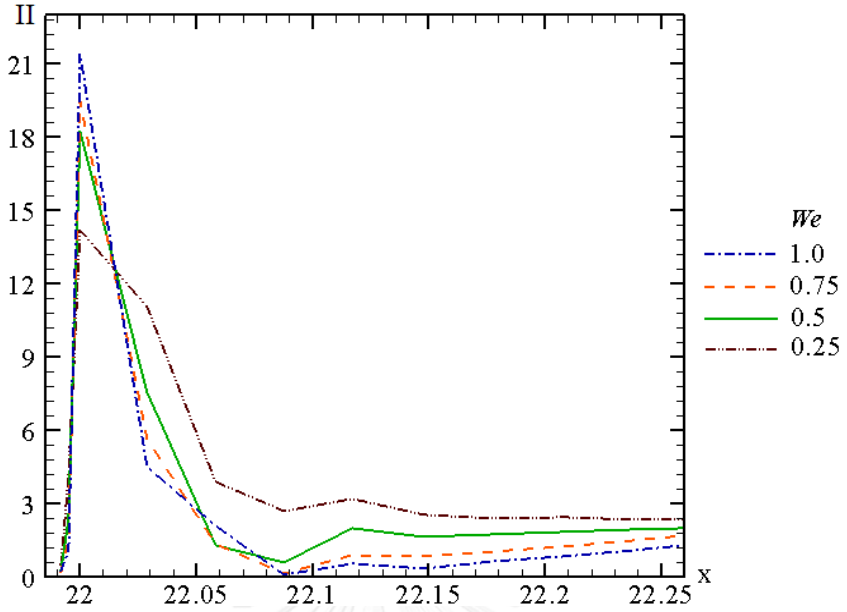

Figure 4.13 II on the top downstream wall without slip of Oldroyd-B fluid

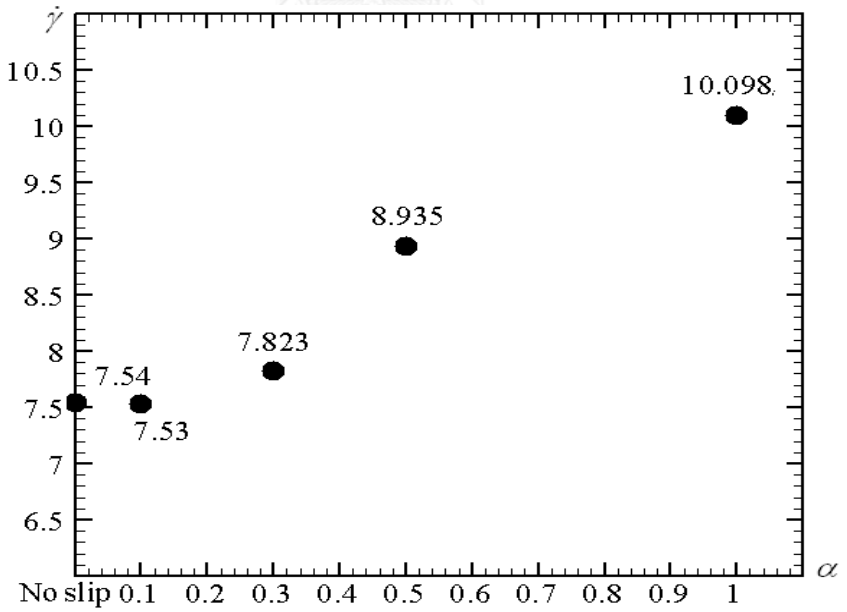

Figure 4.14 The peak of $\dot{\gamma}$ versus α on top downstream wall of Oldroyd-B fluid at $\mathrm{II} = 14$, $We = 0.25$

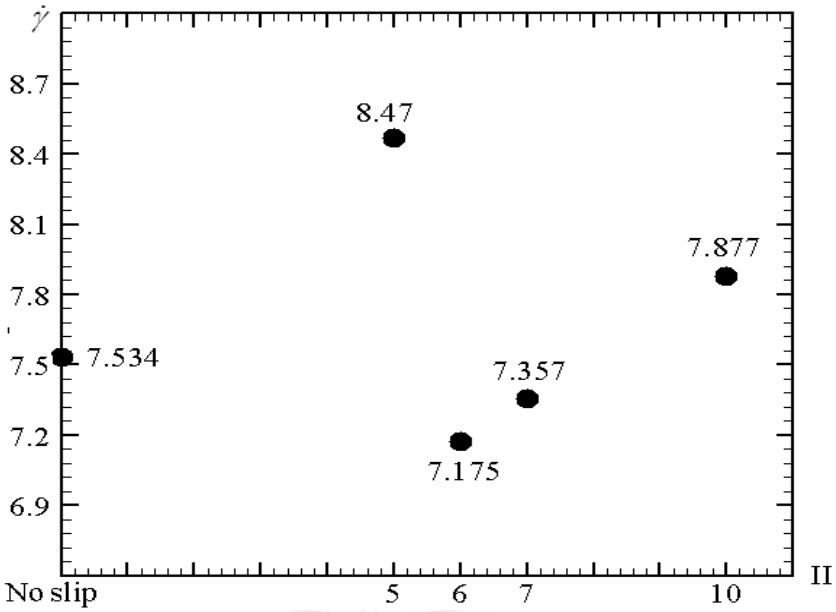

Figure 4.15 The peak of $\dot{\gamma}$ versus $\mathrm{II}_{\mathrm{crit}}$ on top downstream wall of Oldroyd-B fluid at $We = 0.25$

The shear stress τ_{xy} and shear rate $\dot{\gamma}$ are considered for 4 sharp-corner meshes with $We = 0.25$ and $\mathrm{Re} = 0$ at $\mathrm{y} = 3$ as seen in Figure 4.16(a) and 4.16(b), respectively. Under no slip effect, the solution of mesh3 (6220 nodes) and mesh4 (10575 nodes) have slight deviation but there are significant differences with mesh1 (2105 nodes) and mesh2 (2427 nodes) because of delicate node.

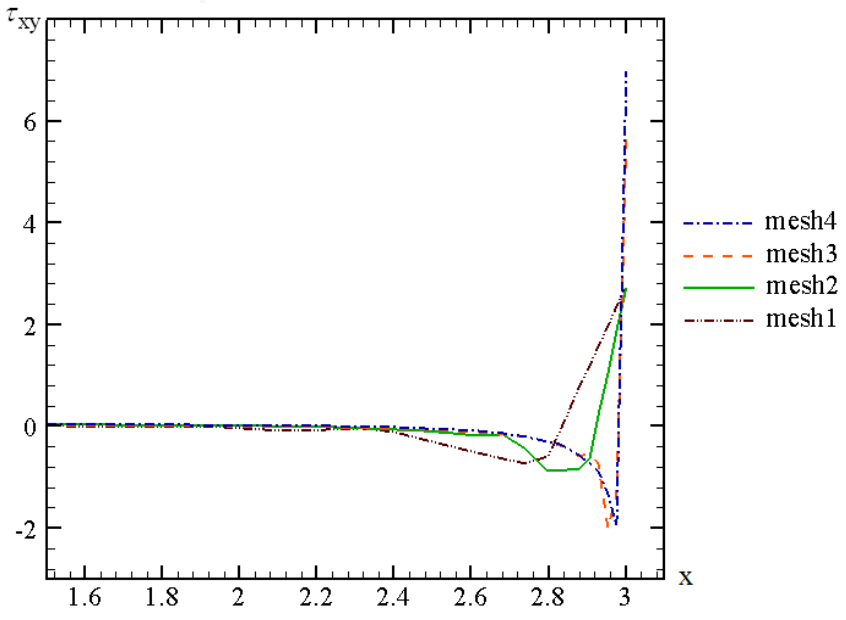

(a) τ_{xy}

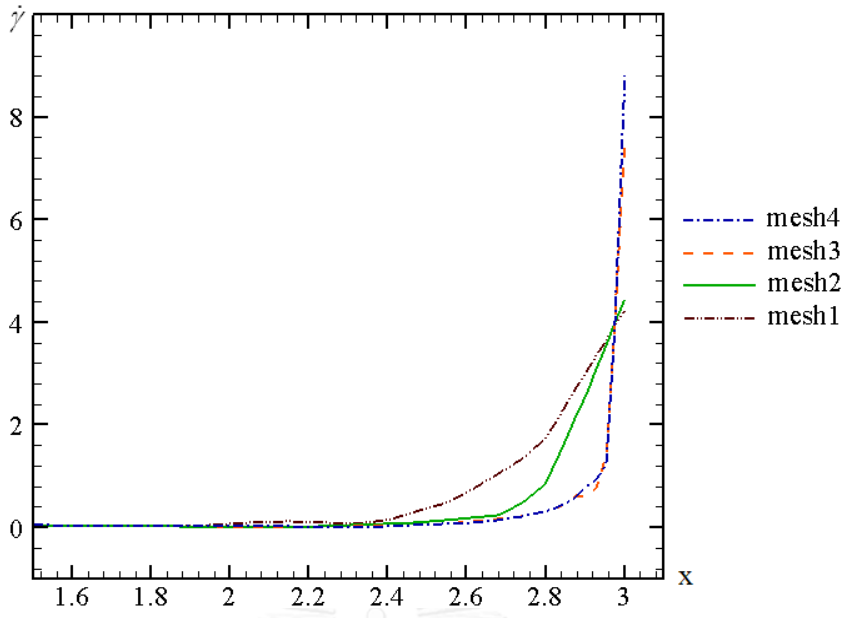

(b) $\dot{\gamma}$

Figure 4.16 Sharp-corner meshes without slip at $y = 3$, $We = 0.25$ and $\mathrm{Re} = 0$

For slip case as shown in Figures 4.17(a) and 4.17(b), mesh3 and mesh4 are almost the same maximum values but mesh1 and mesh2 are shot far from mesh3. After mesh3 is taken to apply in slip condition, the maximum shear stress and shear rate are reduced effectively at channel wall and small difference is deviant from mesh4 so the pattern of mesh3, which the smallest element is nearly as tiny as mesh4, is used to calculate the problem for sharp corner mesh.

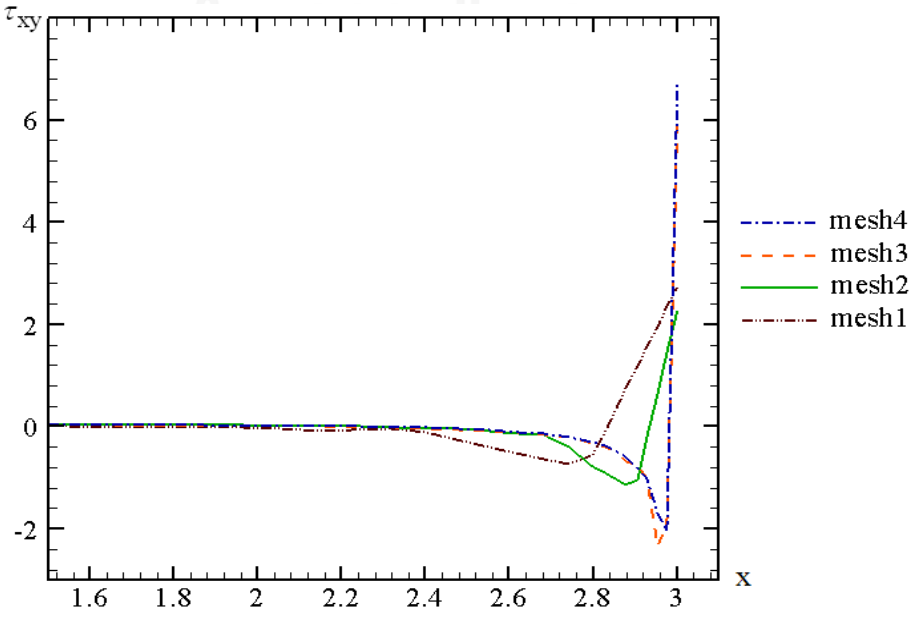

(a) τ_{xy}

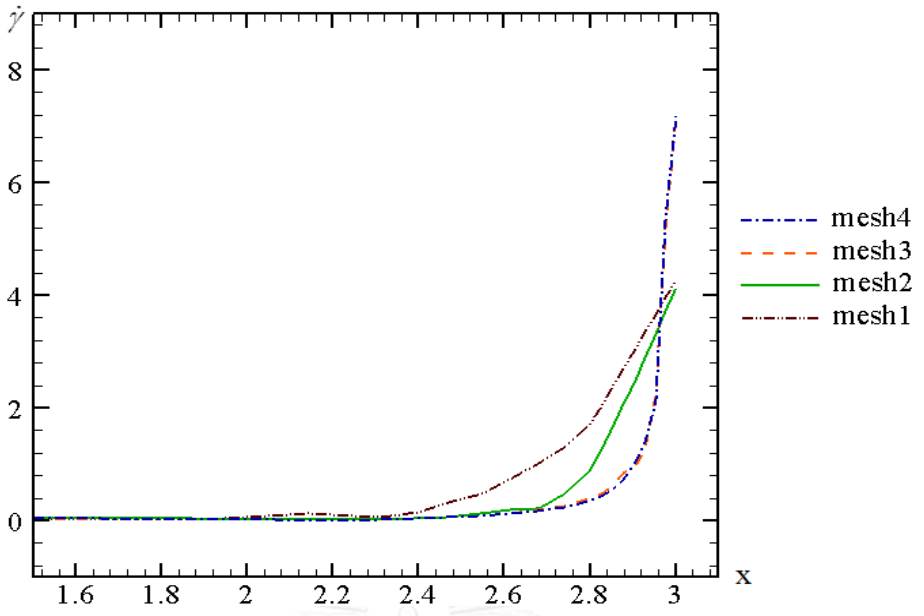

(b) $\dot{\gamma}$

Figure 4.17 Sharp-corner meshes with slip at $y = 3$, $We = 0.25$ and $\mathrm{Re} = 0$

To choose the critical II when $We = 0.5$, the values of II is started at 18 whilst the value of α is varied between 0 and 1. From Figure 4.18, $\alpha = 0.1$ is an optimum value because the other values of α give the higher peak of shear rate so $\dot{\gamma} = 8.506$ is selected to calculate slip velocity as well as Figure 4.20. Similarly, the lowest shear rates of $We = 0.5$ and $We = 0.75$ are chosen to be optimum critical II as depicted in Figure 4.19 and Figure 4.21.

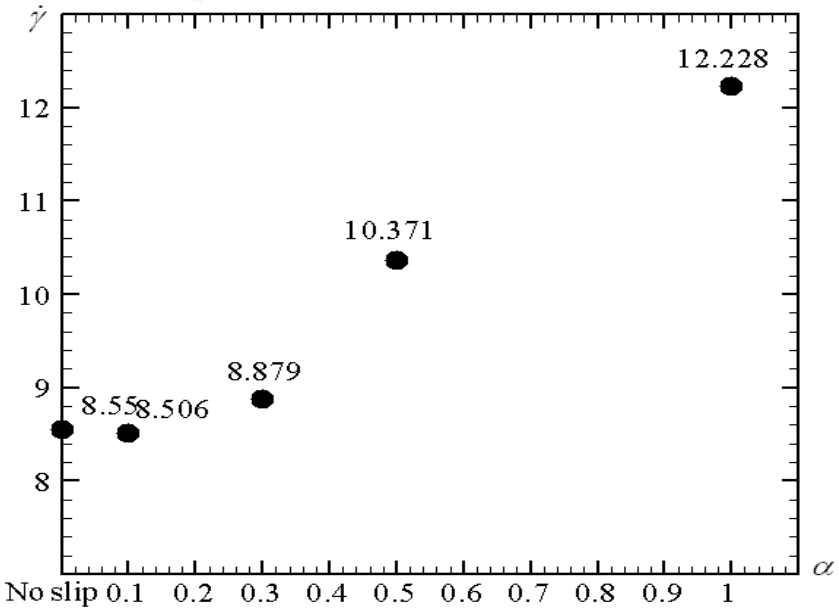

Figure 4.18 The peak of $\dot{\gamma}$ versus α on top downstream wall of Oldroyd-B fluid at $\mathrm{II} = 18$, $We = 0.5$

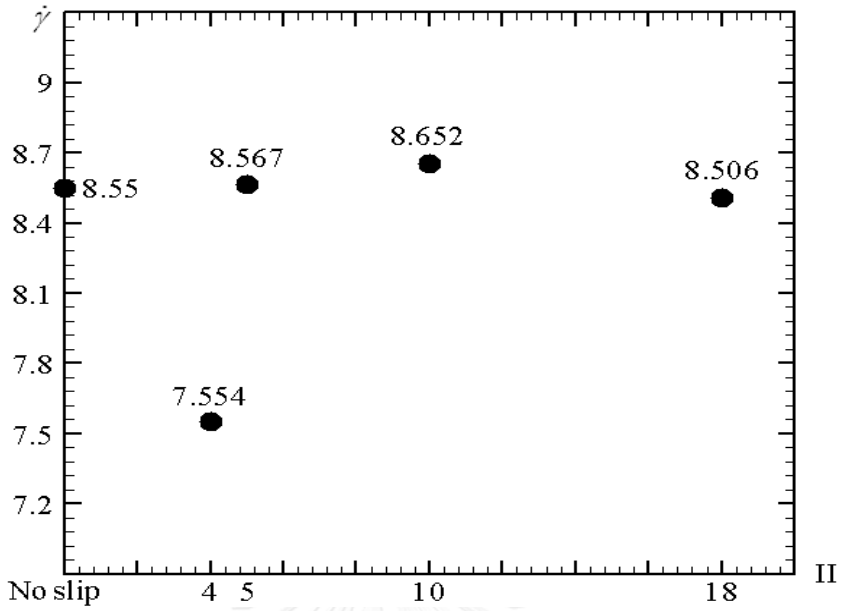

Figure 4.19 The peak $\dot{\gamma}$ of II at $\alpha = 0.1$ along downstream wall at $y = 3$, $We = 0.5$ and $Re = 0$

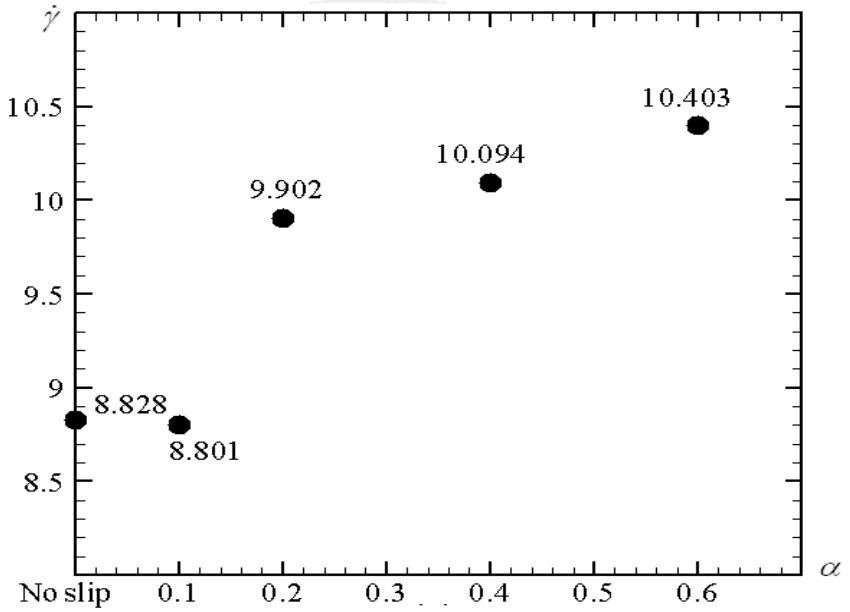

Figure 4.20 The peak of $\dot{\gamma}$ versus α on top downstream wall of Oldroyd-B fluid at $II = 19$, $We = 0.75$

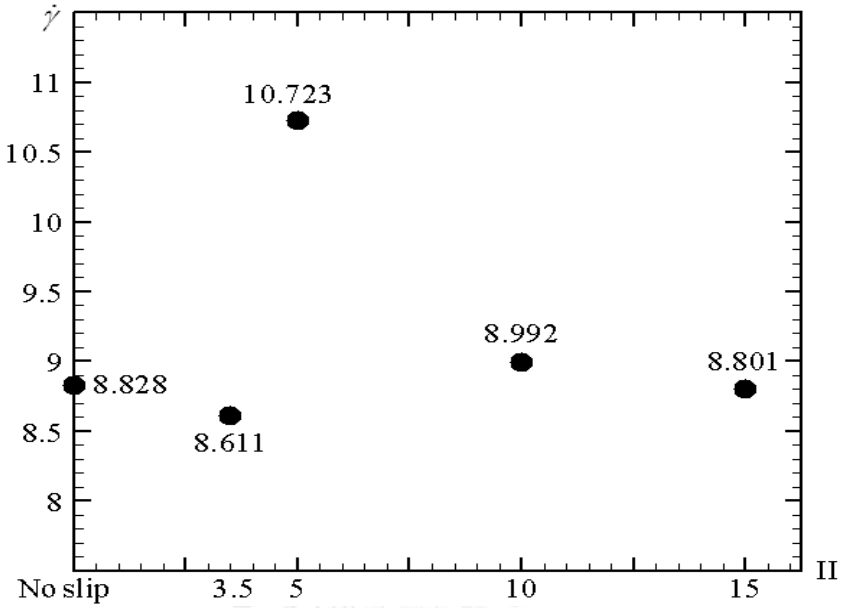

Figure 4.21 The peak $\dot{\gamma}$ of II at $\alpha = 0.1$ along downstream wall at $y = 3$, $We = 0.75$ and $\mathrm{Re} = 0$

The line contours of downstream solutions with slip effect for $We = 0.75$ in Figure 4.22 are explained in term of streamline, velocity, pressure and stresses.

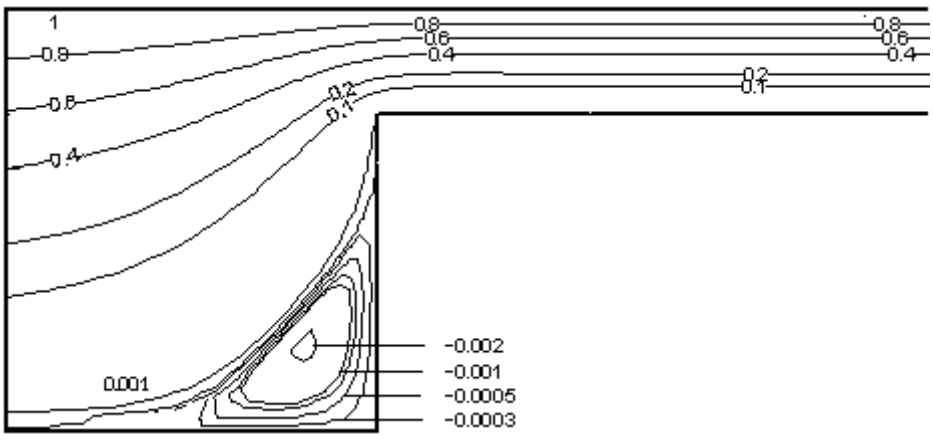

(a) S

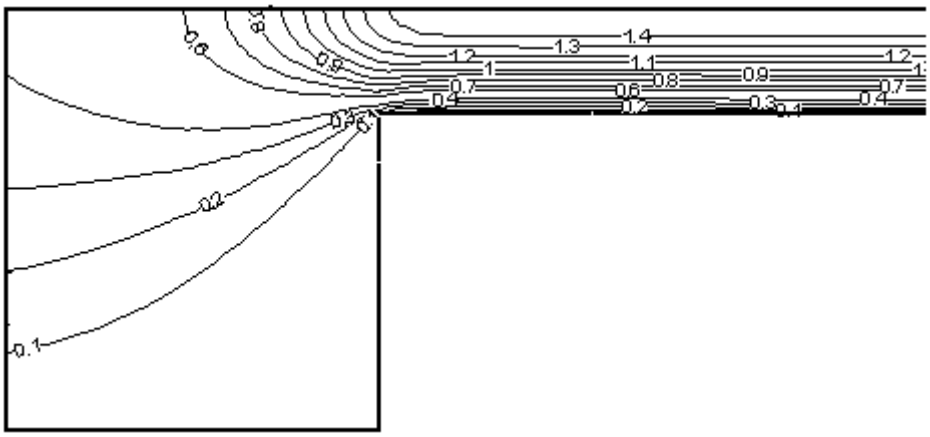
0.6
0.8
0.9
1.2
1.3
1.4
1
1.1
0.7
0.8
0.9
0.4
0.6
0.2
0.3
0.4
0.2
0.1

(b) u_x

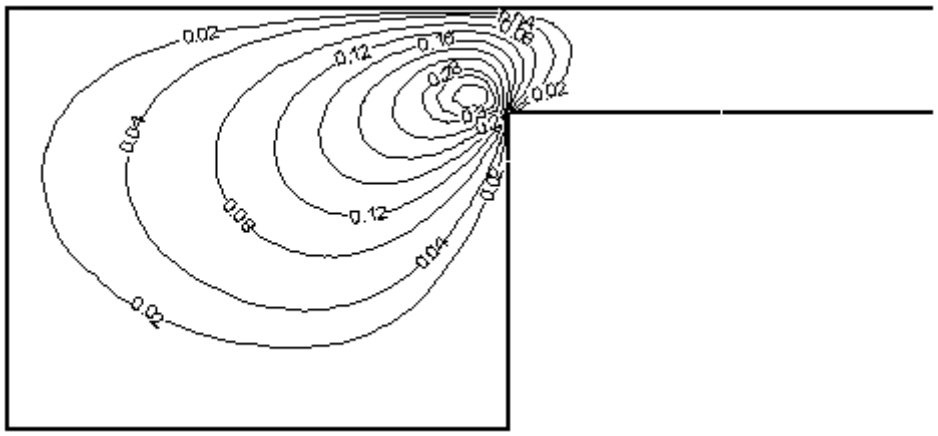
0.02
0.12
0.16
0.08
0.04
0.02
0.12
0.04
0.02

(c) u_y

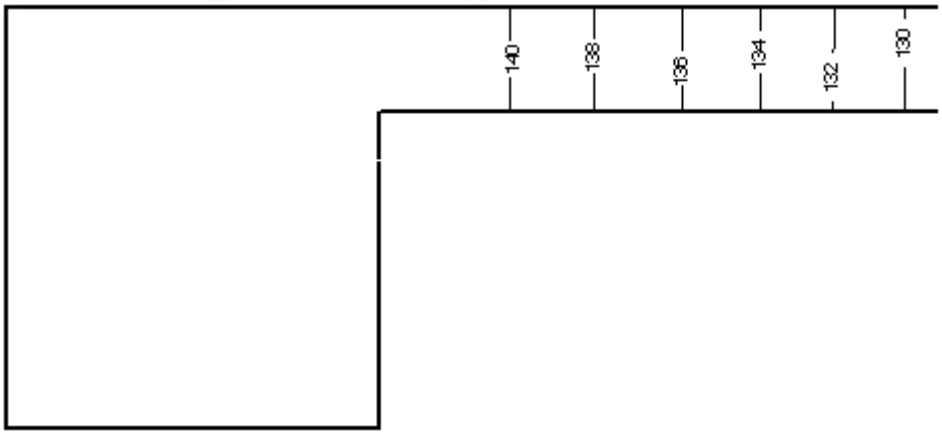
140
138
136
134
132
130

(d) p

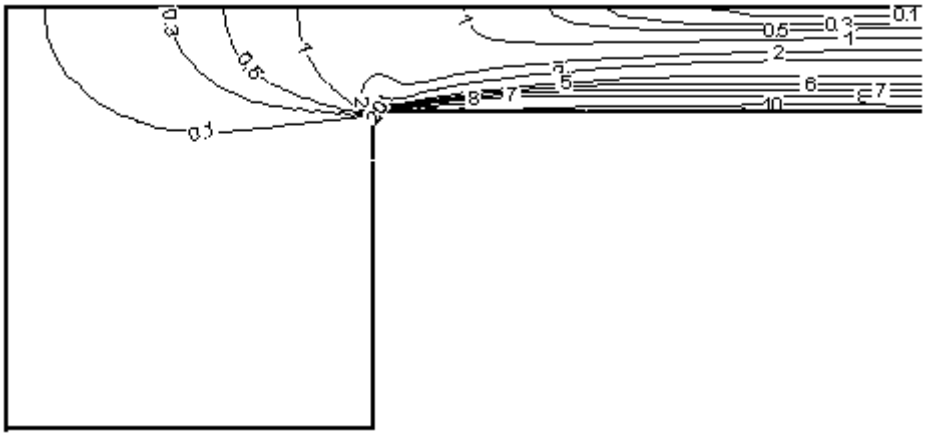

(e) τ_{xx}

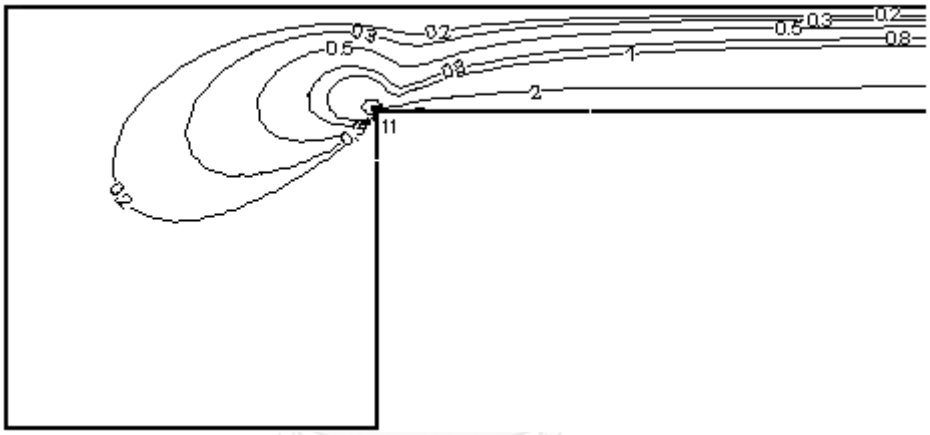

(f) τ_{xy}

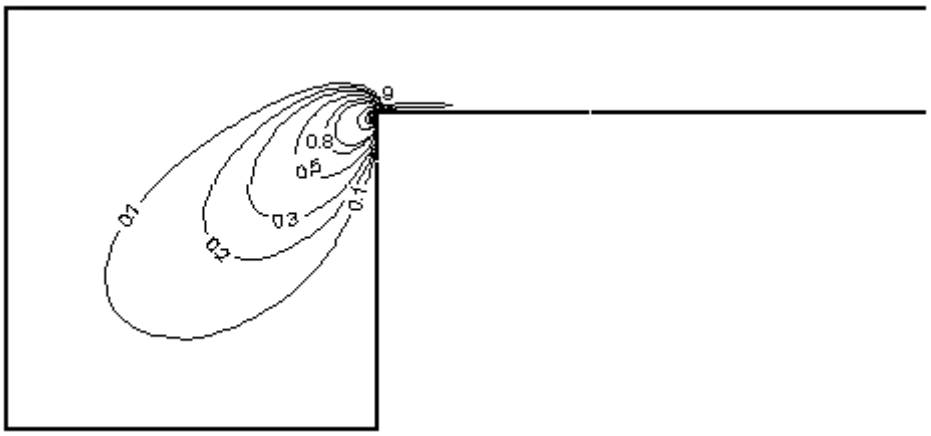

(g) τ_{yy}

Figure 4.22 Line contour of mesh3 with slip along downstream wall at $y = 3 : \alpha = 0.1$, $II = 3.5$, $We = 0.75$ and $Re = 0$

Table 4.9 The lowest shear rate for proper α and suitable II of Oldroyd-B fluid

We	0	0.25	0.5	0.75	1
α	0.1	0.1	0.1	0.1	0.1
$\mathrm{II}_{\mathrm{crit}}$	2.3	6	4	3.5	3.3
$\dot{\gamma}$	5.968	7.175	7.554	8.611	8.801

Similarly, the lowest shear rates of $We = 1.0$ is selected in same algorithm for fitting critical II as shown in Table 4.9. Summarizing the highest τ_{xx} and the maximum shear rate values of the optimum slip velocity in Table 4.10 are less than the maximum values of no slip condition. The maximum value of τ_{xx} is reduced from 19.943 to 13.494 and the peak of $\dot{\gamma}$ is reduced from 7.534 to 7.175 at $We = 0.25$. Similar to the trend of the slip influence for *We* at 0.5, 0.75 and 1, the maximum of $\dot{\gamma}$ and τ_{xx} without slip falls below that for the case with slip. Highly reducing the stress value is clearly investigated, refer to Table 4.10.

Table 4.10 The peak value of $\dot{\gamma}$ and τ_{xx} on the top downstream wall

We	$\dot{\gamma}$		τ_{xx}	
	no Slip	Slip	no Slip	Slip
0.25	7.534	7.175	19.943	13.494
0.5	8.550	7.554	29.455	20.586
0.75	8.828	8.611	34.042	30.975
1	9.253	8.721	36.571	34.557

Figure 4.23 shows the comparison of two restrictions under condition of no-slip and slip along bottom downstream wall with J&S (Johnson-Segalman) theory by relating τ_{xy} and $\dot{\gamma}$ at $We = 0.25$ and $We = 1.0$. This plot is indicative of the fact that the shear

stress of both cases agree in trend along the resistance but slip limitation is closer to J&S though the value of prediction is slightly undershoot.

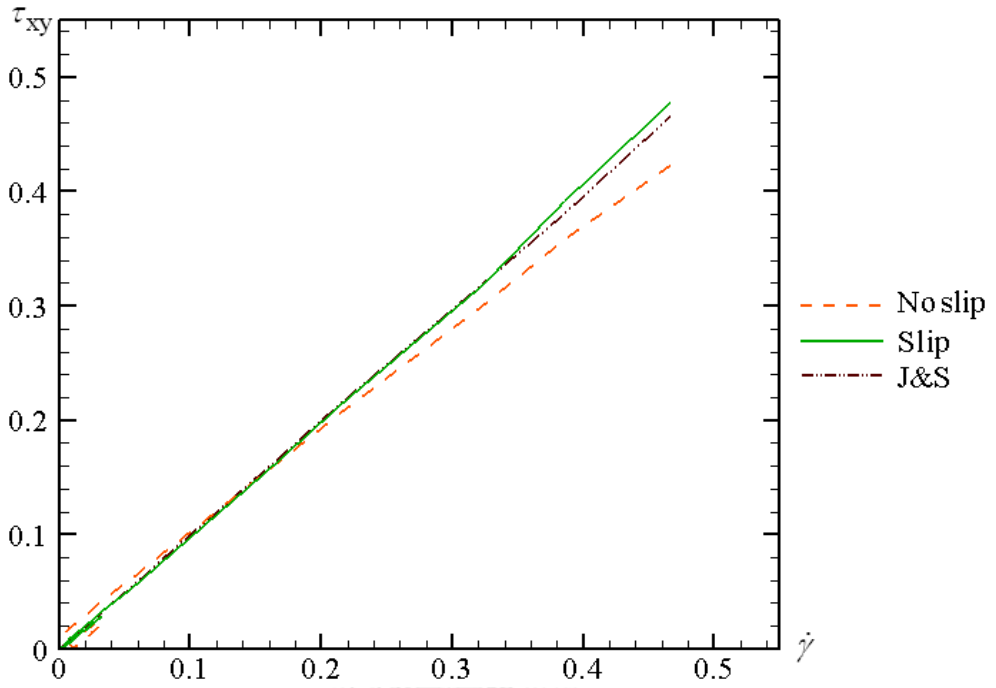

(a) $We = 0.25$

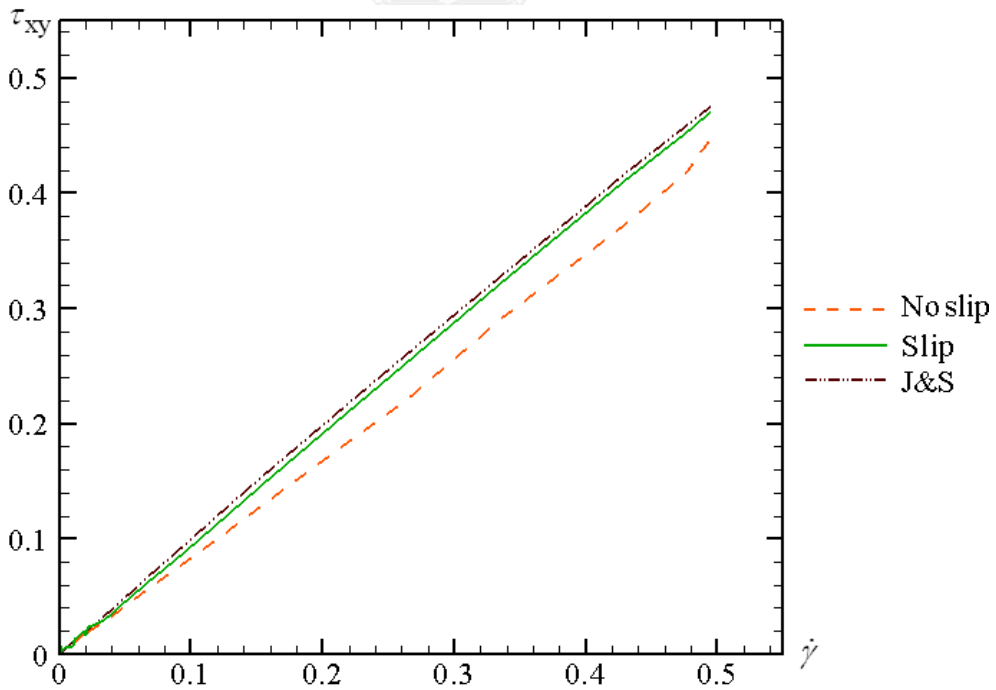

(b) $We = 1.0$

Figure 4.23 The comparison of τ_{xy} versus $\dot{\gamma}$ with J&S on top downstream wall of Oldroyd-B fluid

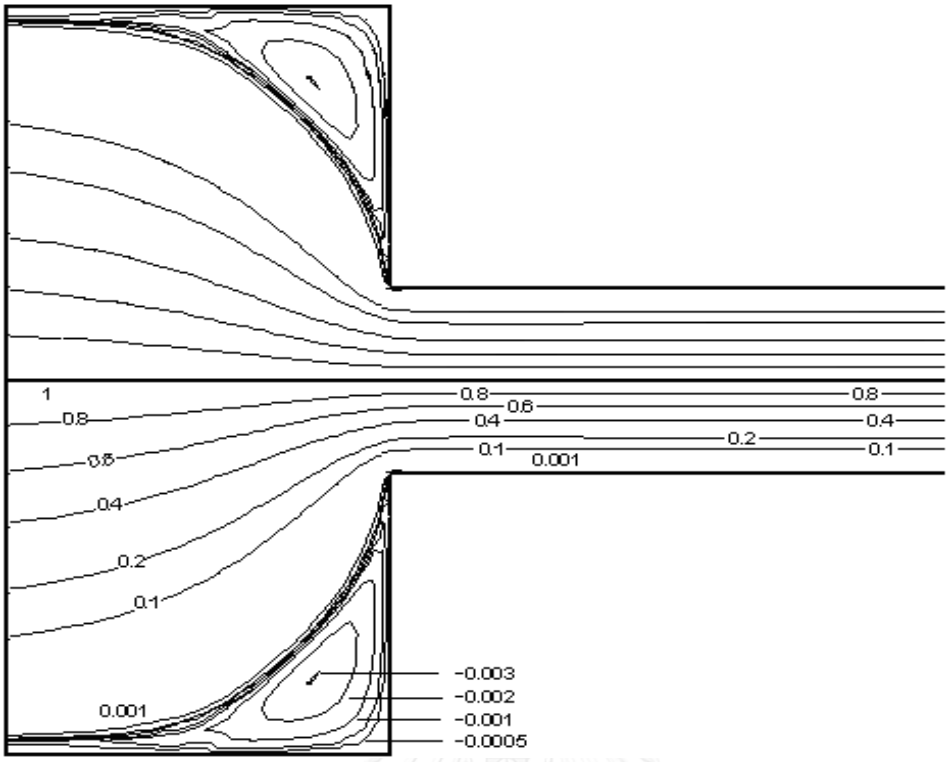

(a) No slip

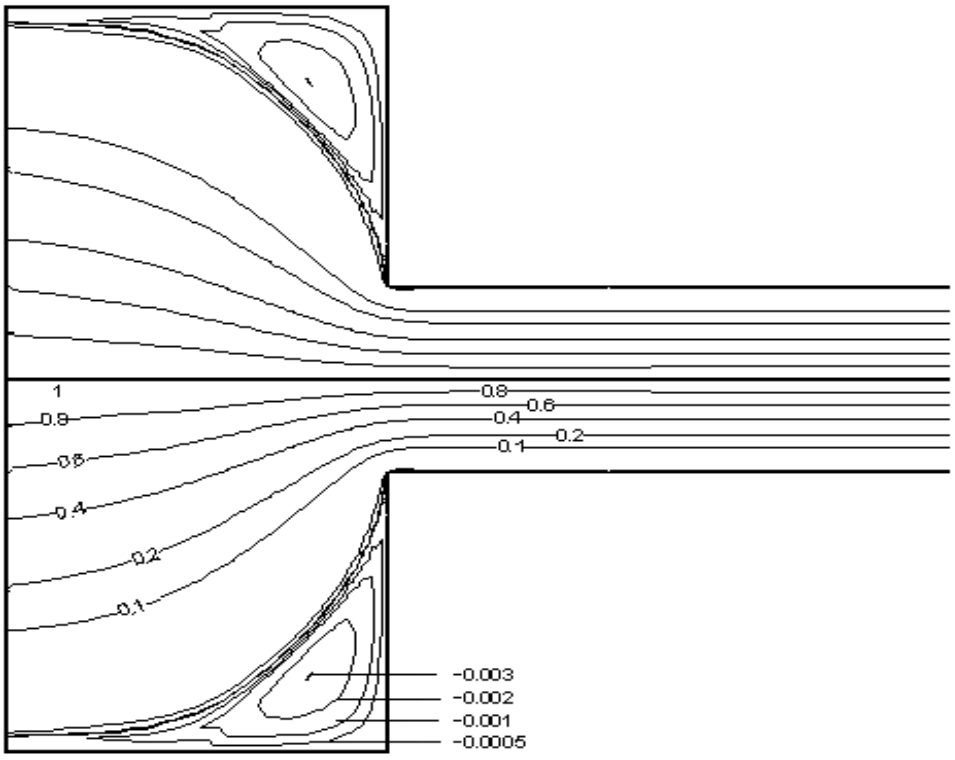

(b) slip at $\alpha = 0.1$ and $\mathrm{II} = 3.3$

Figure 4.24 S line contour of Oldroyd-B at $We = 1.0$

For the streamline comparison with no slip of Figure 4.24(a) and with slip of Figure 4.24(b), the serious vortex is still noticed easily for no slip case so this observation can get along well with Oldroyd-B behaviour.

As stated above (the reason for using $We = 1.0$ for final solution), Figure 4.25 depicts the line contour of slip condition for $\alpha = 0.1$ in line with the following explanation: Figure 4.25(a) shows the maximum value of velocity u_x at symmetry line, Figure 4.25(b) displays the maxima value of velocity u_y near the location of sharp corner contraction position, Figure 4.25(c) represents line contour of maximum pressure inlet boundary, the maximum τ_{xx}, τ_{xy} and τ_{yy} can be seen in Figures 4.25(d)-4.25(f) are 34.042, 14.505, and 7.116, respectively.

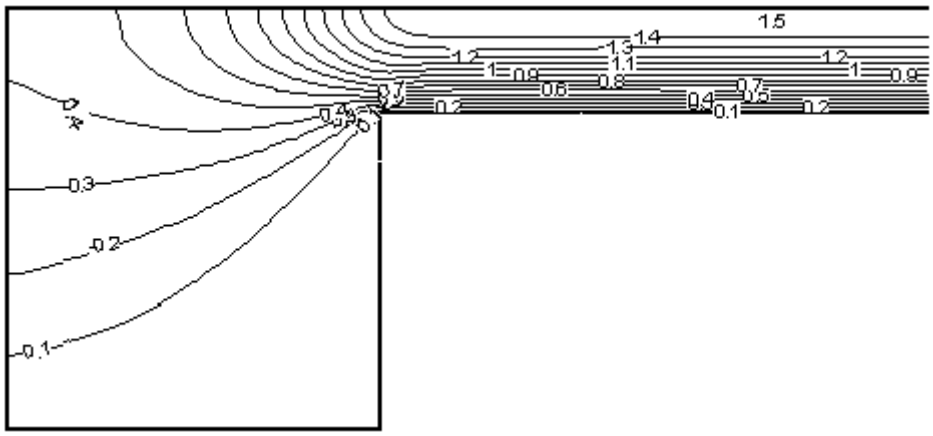

(a) u_x

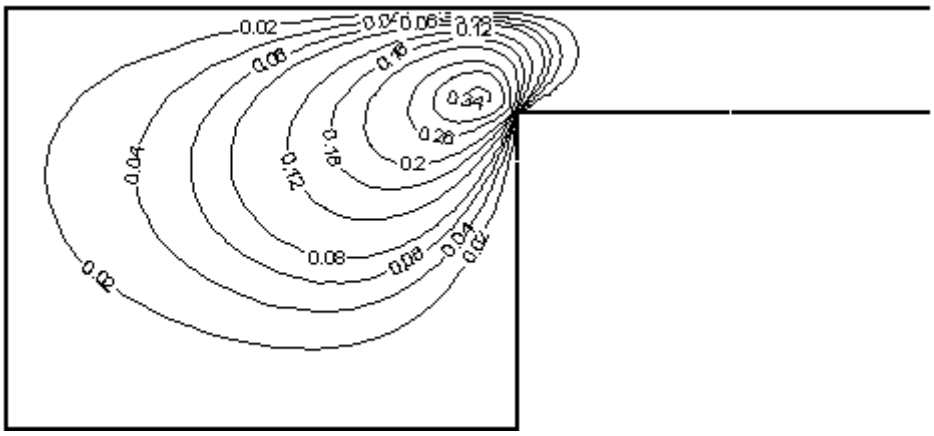

(b) u_y

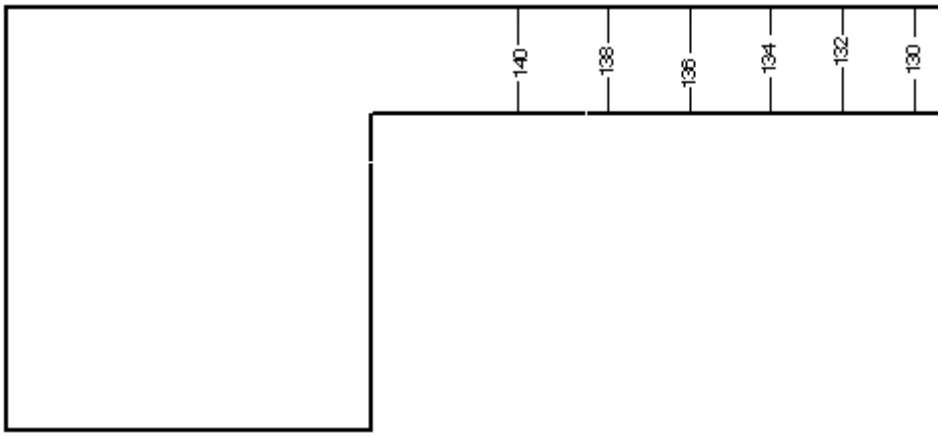

(c) p

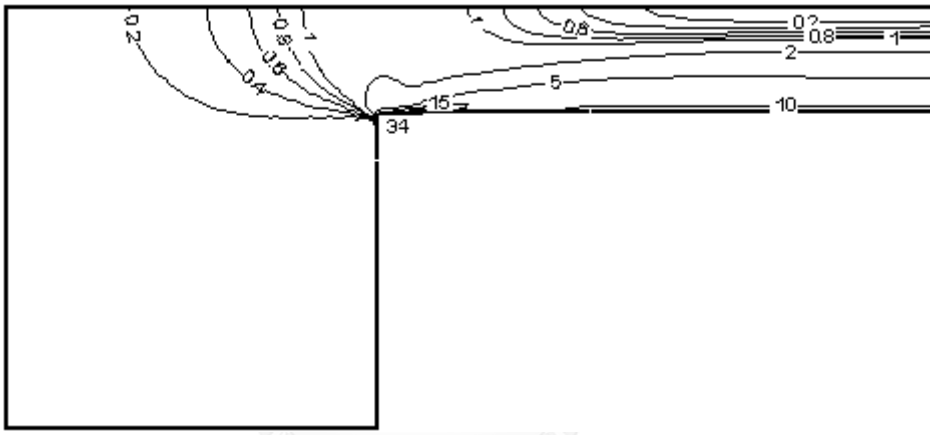

(d) τ_{xx}

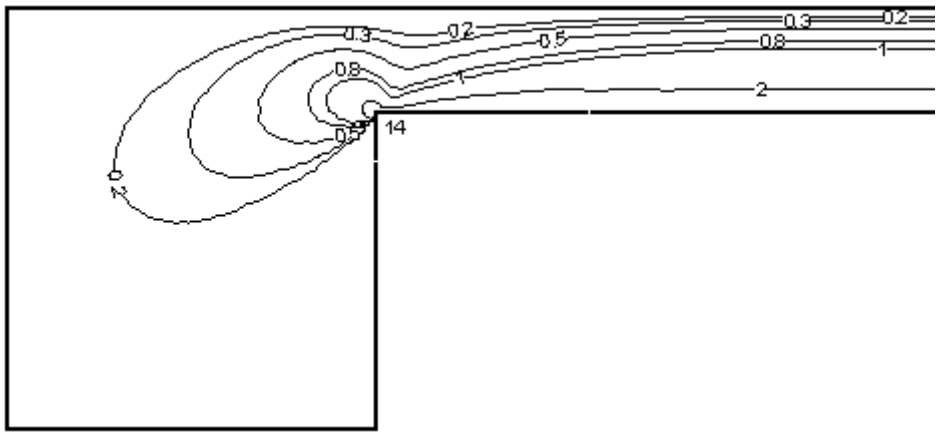

(e) τ_{xy}

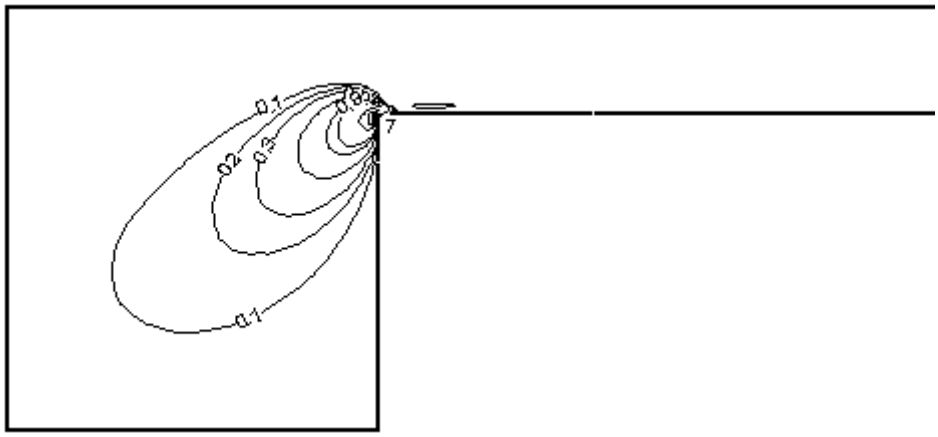

(f) τ_{yy}

Figure 4.25 Line contour with slip along top downstream wall of Oldroyd-B fluid at $\alpha = 0.1$, $\mathrm{II} = 3.3$ and $We = 1.0$

4.5 Results of 4:1 Rounded Contraction Flow

In industrial process especially for 4:1 contraction problem, there are many objections when fluid passes through a part of abrupt contraction so the geometrical domain of this problem for sharp corner has been changed to rounded corner as shown in Figure 4.5. The downstream half channel width of planar 4:1 contraction at entry and exit sections are 27.5L and 49L respectively. At inlet entry, fluid flow is set Poiseuille flow in channel length which is long enough for developing parabolic flow at exit section. At the channel wall, the slip condition is added to compute slip velocity that appeared in real problem.

4.5.1 Feedback of Pressure-Driven Velocity Flow of Newtonain Fluid

The 4:1 rounded corner contraction problem as shown in Figure 4.5 was computed with standard STGFEM to get the outcomes that were taken a large number of time steps to execute the program for these three mesh patterns. The boundary condition at inlet is forced to be parabolic curve but the horizontal velocity contours at the beginning of upstream fluid in Figure 4.26 for all mesh patterns are not the same style as it is imposed onto the boundary. This phenomenon yielded an irregular solution and finally the unexpected outcome is met even if the solution was obtained.

The entrance pattern was distorted so the urgent cure needs to add in the normal procedure by means of FPDVF to drive flow in a good manner. After flow was rectified, the velocity contours look clearly as Poiseuille flow which is displayed in Figure 4.27.

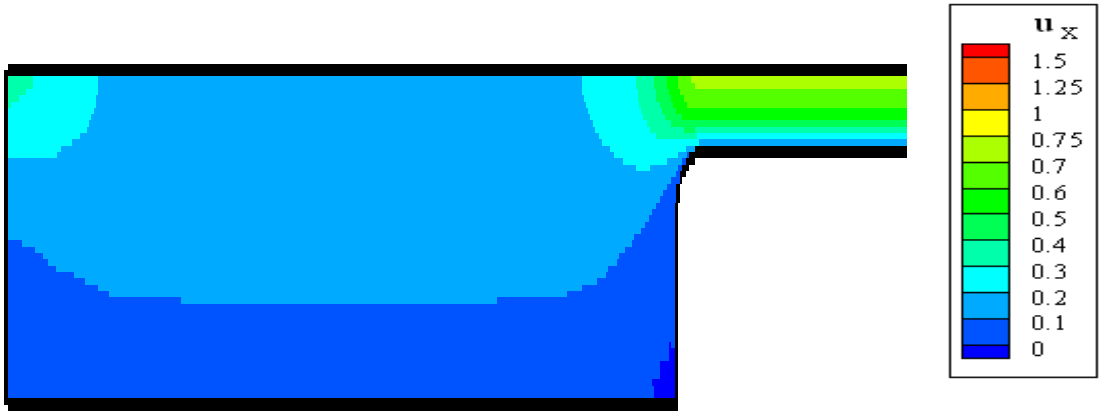

(a) mesh5

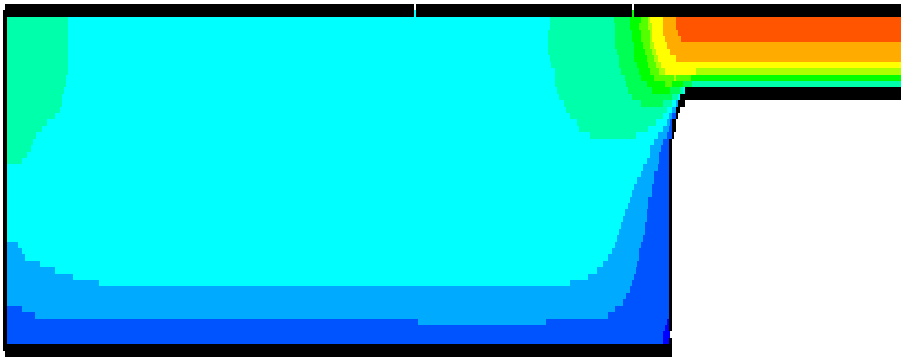

(b) mesh6

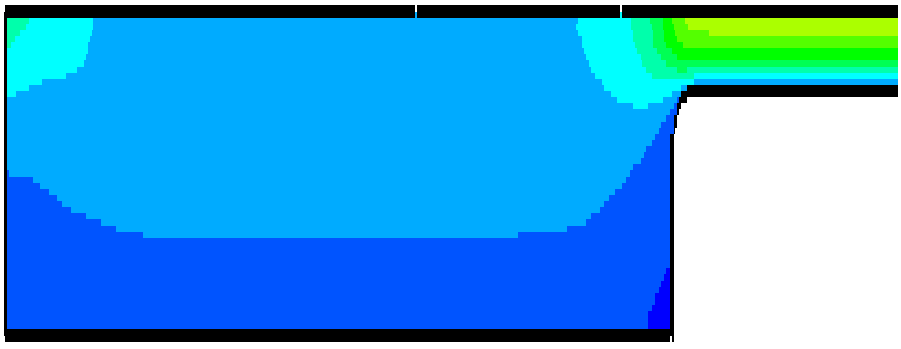

(c) mesh7

Figure 4.26 u_x contour with standard STGFEM

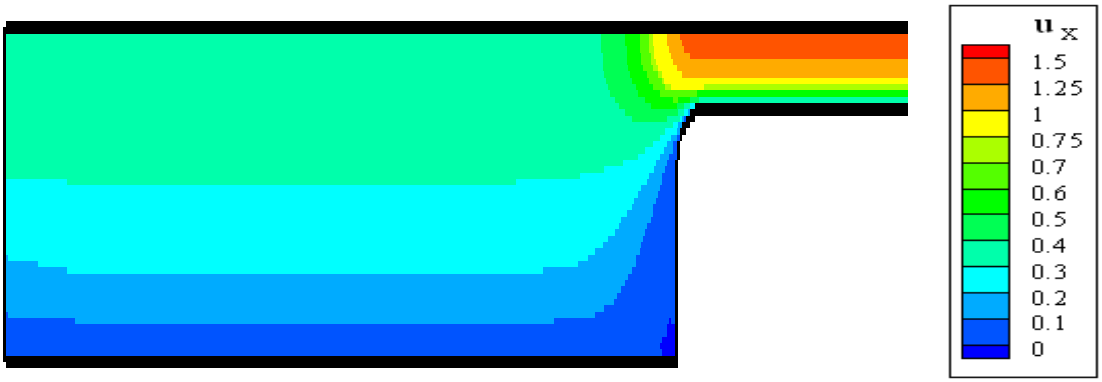

(a) mesh5

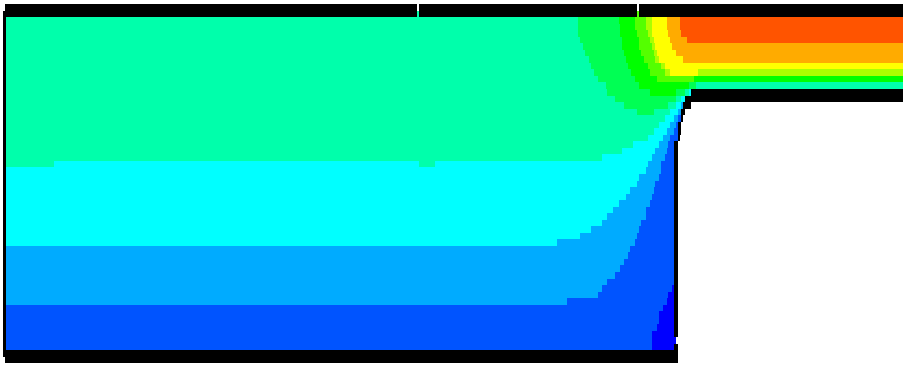

(b) mesh6

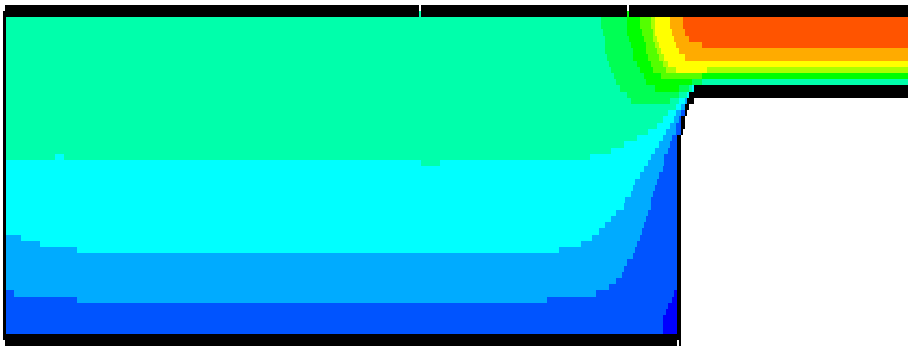

(c) mesh7

Figure 4.27 u_x contour of STGFEM with FPDVF

To find the proper mesh for displaying final solution, the comparison of solutions for all meshes is considered to reduce some repetitive pictures. After the best mesh has been identified, the streamline and pressure line contour will be plotted for Newtonian

fluid under treatment of FPDVF. For comparing STGFEM methods with and without treatment, the flow properties of both cases are depicted. The calculation by STGFEM with remedy can get converging appearance of right contour for velocity field whilst the outcome of normal computation is inconsistent. Table 4.11 compares the peak values of velocity and pressure for normal STGFEM and STGFEM with treatment. The velocity and pressure values of mesh5 and mesh7 are twice those of normal STGFEM because the solution from normal running without driving by pressure does not have enough force to shove liquid in a long channel whilst the velocity and pressure of mesh6 are a bit higher than other options of treatment. In addition, mesh6 indicates a reduced time step of about 27.15% which is the highest reduction amongst the three mesh patterns. These results imply that mesh6 is the best pattern to exhibit final demonstration. Therefore STGFEM with pressure-driven velocity flow can improve characteristic line and correct solution together with the number of time step is cutback.

Table 4.11 The solution comparison of peak value for various mesh patterns

Solution	mesh5		mesh6		mesh7	
	FPDVF	STGFEM	FPDVF	STGFEM	FPDVF	STGFEM
u_x^{max}	1.50	0.75	1.52	1.51	1.52	0.75
u_y^{max}	0.29	0.14	0.29	0.34	0.29	0.14
p_{max}	144.35	74.91	144.38	150.86	144.26	75.34
Time step	2862	3361	2074	2847	3036	4069

Not only velocity and pressure are studied thoroughly but also all stresses and shear rate are considered to check the deformation at contraction point that can occur so the 4:1 rounded corner contraction problem was solved by STGFEM combined with FPDVF and the collection of stresses and shear rates especially for the maximum values recorded. The highest values of normal stress, shear stress and shear rate $\dot{\gamma}$ on

bottom downstream wall are tabulated in Table 4.12. Under uniform mesh pattern, the results make clear that the peak values of all meshes are similar and dependent on element size. The tendency of highest values for stresses and shear rate versus refined mesh in Table 4.11 are similar except for the value of τ_{yy} for mesh6 which is slightly higher than those in mesh5 and mesh7.

Table 4.12 Comparison of the peak values on bottom downstream wall

Mesh	τ_{xx}	τ_{xy}	τ_{yy}	$\dot{\gamma}$
mesh5	7.177	3.542	0.261	3.734
mesh6	7.447	3.698	0.265	3.888
mesh7	7.955	3.905	0.252	4.034

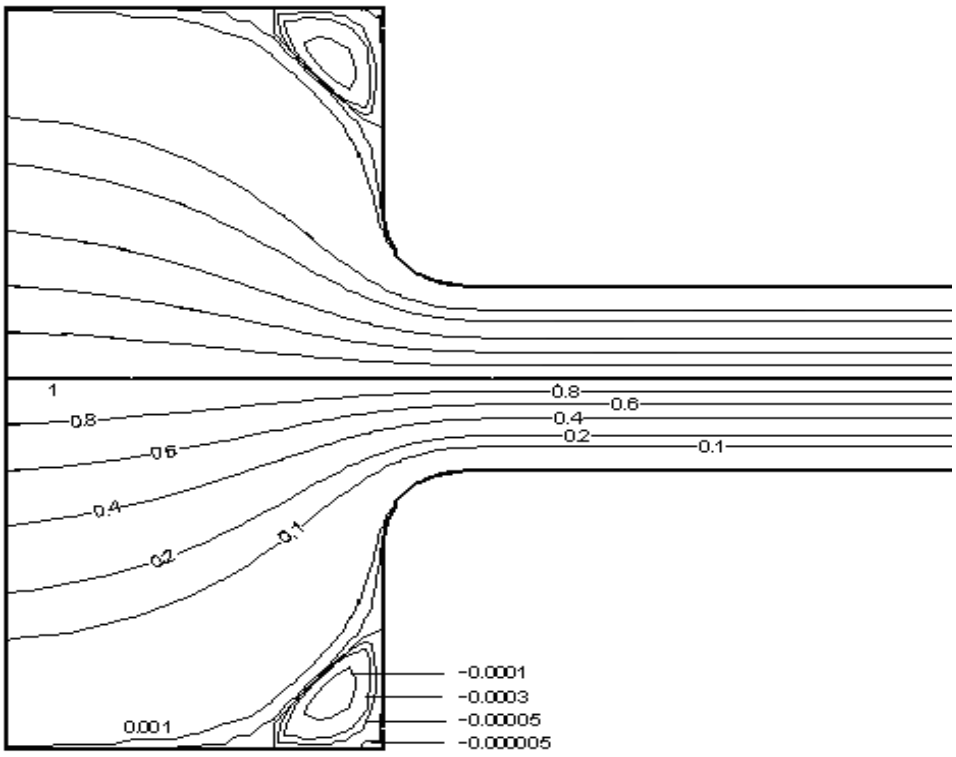

Figure 4.28 Streamline contour of STGFEM with FPDVF for mesh6

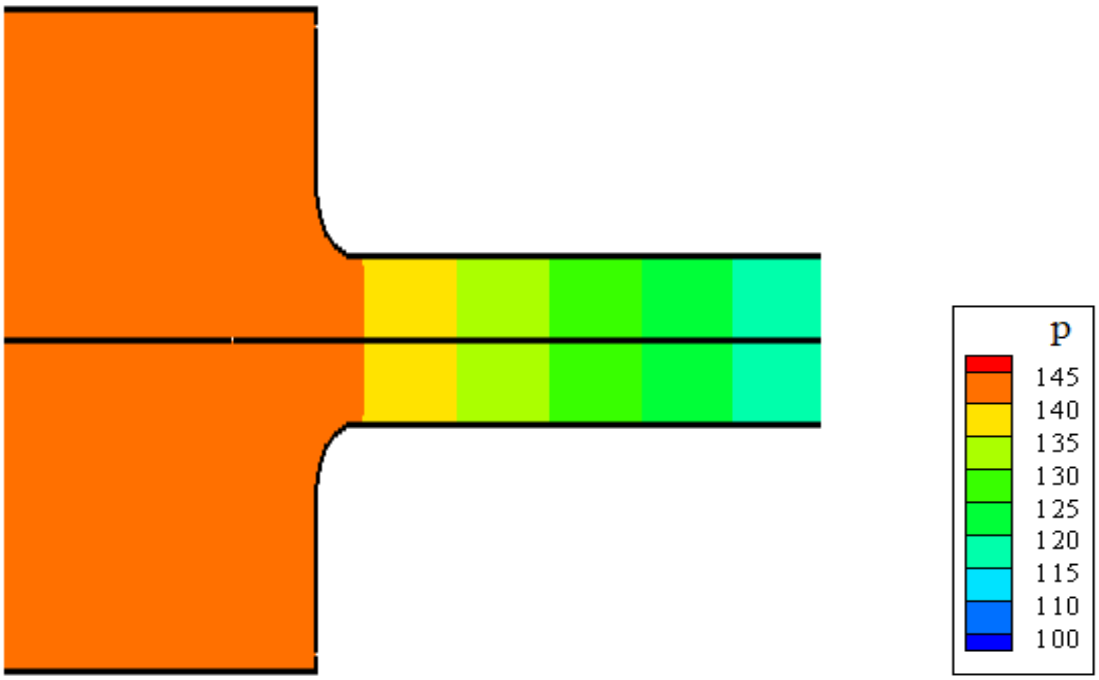

Figure 4.29 p color contour of STGFEM with FPDVF for mesh6

The overlook of the result for all meshes demonstrates that the results of mesh6 are in close conformity with those obtained for mesh7 and the program can access mesh6 comfortably. Thus, mesh6 is chosen as a model of final solution which sustains the above statement. The streamline contour of Newtonian fluid for mesh6 after remedy of FPDVF is shown in Figure 4.28 which displays normal streamline, and indeed looks more stable like virtual experimental pattern and two big vortices at the top and bottom contraction angles. The color contour of pressure for this treatment matches closely the converge solution as presented in Figure 4.29.

4.5.2 Slip Effect of Newtonain Fluid

To find the proper mesh for displaying final solution, the comparison of solutions for all meshes is considered in order to reduce computer times. After the best mesh was chosen, it was applied to operate in Newtonian problem under no slip case and slip condition. A stick or no slip problem has been studied by collecting stresses and shear rate so the highest values of normal stress, shear stress and shear rate $\dot{\gamma}$ on bottom

downstream wall are shown in Table 4.12. It is investigated that the peak values of all meshes are similar and depend on element size. The tendency of highest values for stresses and shear rate versus mesh acuteness in Table 4.12 are similar except for the value of τ_{yy} for mesh6 which is slightly higher than that for mesh7. By overlooking the result for all meshes it is noticed that the result of mesh6 is close to mesh7 and the program can access mesh6 comfortably. Thus, mesh6 is chosen as a model of final solution.

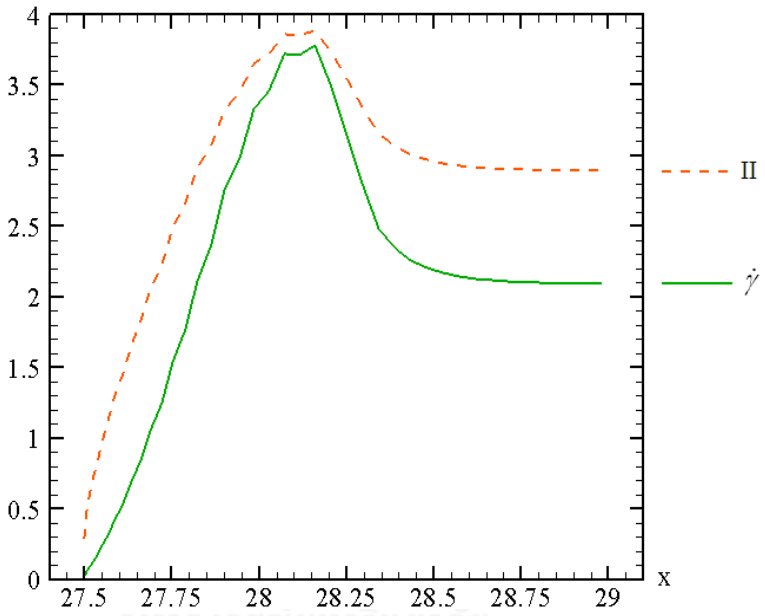

Figure 4.30 II and $\dot{\gamma}$ along downstream wall with no slip, Newtonian fluid

The trend of second invariant (II) and shear rate ($\dot{\gamma}$) look alike as depicted in Figure 4.30. Now, the slip condition is started to observe from critical II to find the optimal slip coefficient (α) by assuming the values of the slip coefficient. First, α is set at 1 in order to find the proper critical II then various choices of II between 2.3 and 3.6 have been determined as depicted in Figure 4.31 so it is exhibited that the critical value of II equals 2.3 made the peak of shear rate grown to 3.857, which is the lowest value when compared with the other peak values of II as shown in Figure 4.32. Using the critical II to decide the optimum α, the minimum shear rate is displayed by $\alpha = 0.1$ as illustrated in Figure 4.33 and the shear rate of α at 0.1, 0.2, 0.4 and 1.0 are widely oscillated. It is found that the trend of shear rate is higher when the second

invariant value increases like the slip coefficient value. As stated above, II = 2.3 is selected to display final solution.

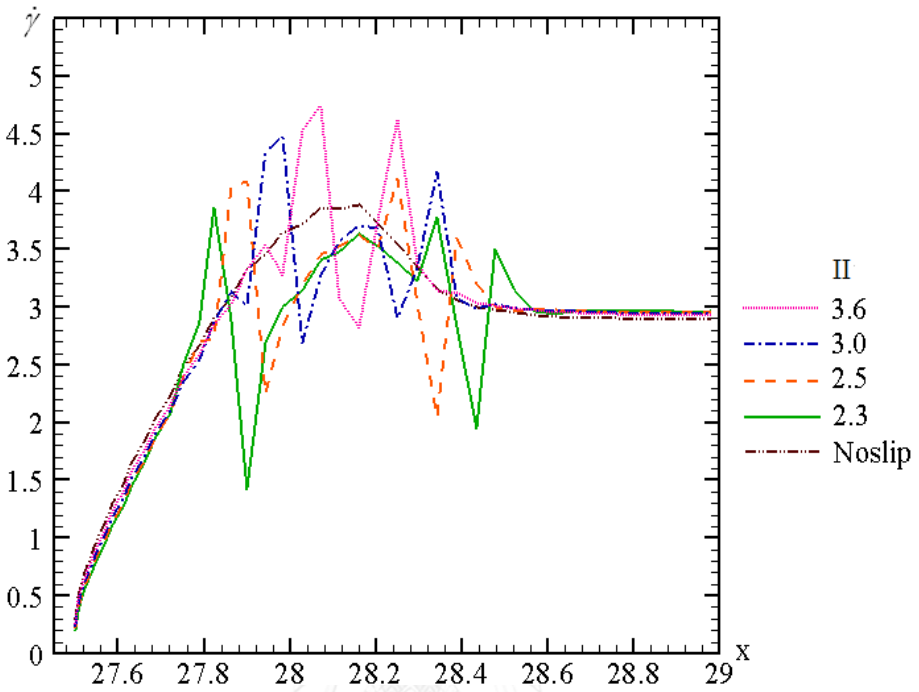

Figure 4.31 $\dot{\gamma}$ with variation of II at $\alpha = 0.1$, Rounded corner, Newtonian fluid

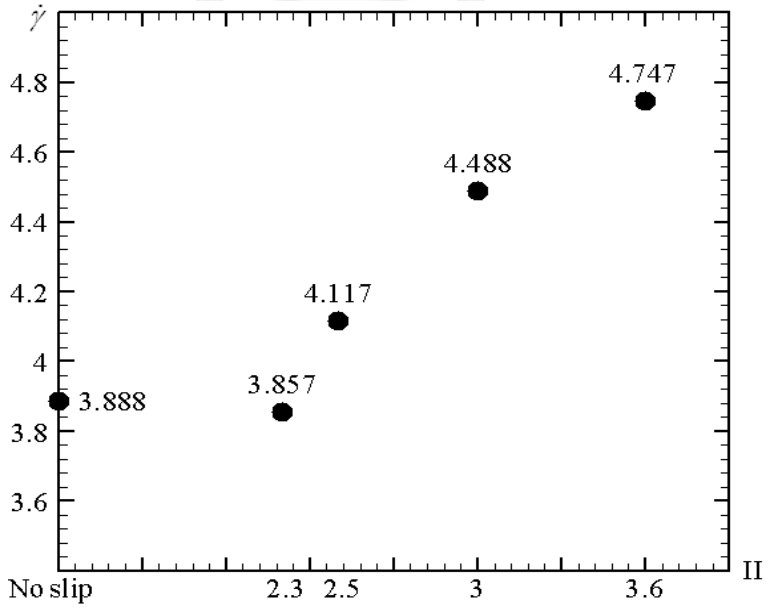

Figure 4.32 The peak of $\dot{\gamma}$ with variation of II at $\alpha = 1.0$, Rounded corner, Newtonian fluid

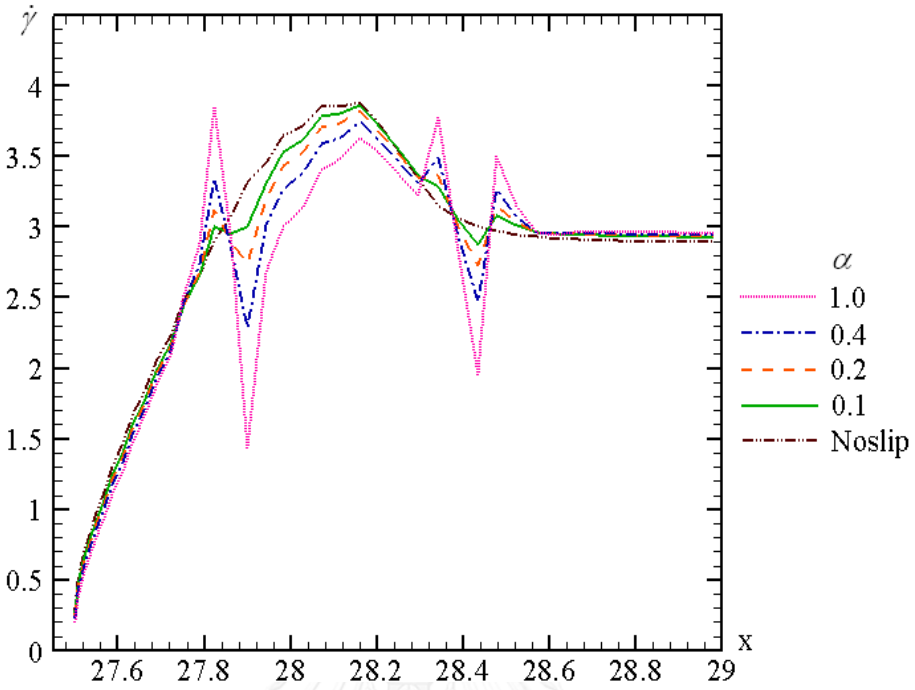

Figure 4.33 The peak of $\dot{\gamma}$ with variation of α at $\mathrm{II} = 2.3$, Rounded corner, Newtonian fluid

The streamline contour of Newtonian fluid for slip instance at $\alpha = 0.1$ and $\mathrm{II} = 2.3$ is shown in Figures 4.34(a). The simple observation of vortex around the corner contraction for no-slip velocity looks more acute than the slip figure. In case of slip condition for $\alpha = 0.1$, Figure 4.34(b) displays the horizontal velocity (u_x) of parabolic line shape, which shows the maximum value at symmetric line while Figure 4.34(c) shows the line contour of vertical velocity (u_y) and the maximum value is near the location of rounded corner contraction position since fluid pass through the sudden changed geometry from 4 unit reduce to 1 unit. Figure 4.34(d) represents line contour of pressure (p) that shows the maximum value at the inlet boundary and then gradually decreased to zero at the end of downstream flow.

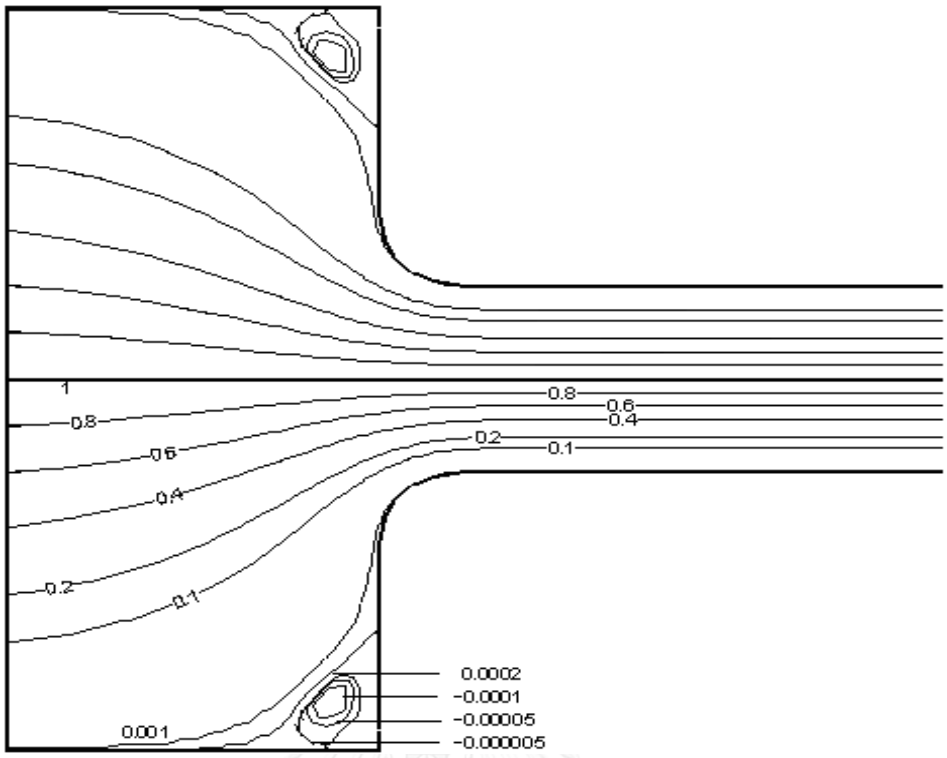
1
0.8
0.6
0.4
0.2
0.1
0.001
0.0002
-0.0001
-0.00005
-0.000005

(a) *S*

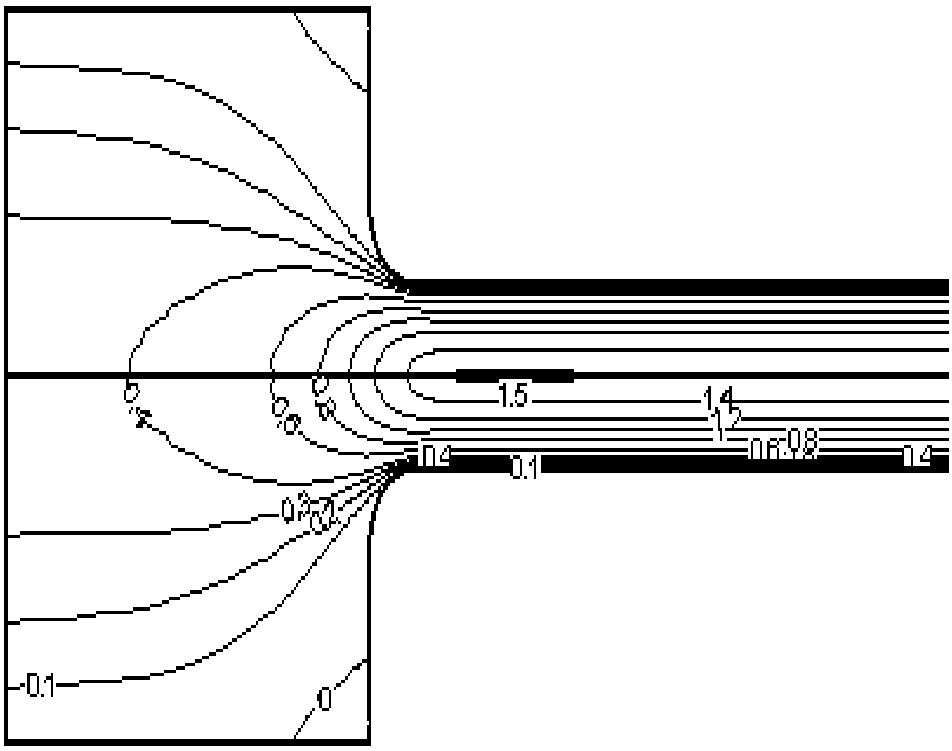
1.5
1.4
1.2
0.8
0.6
0.4
0.1
0.2
0
-0.1

(b) u_x

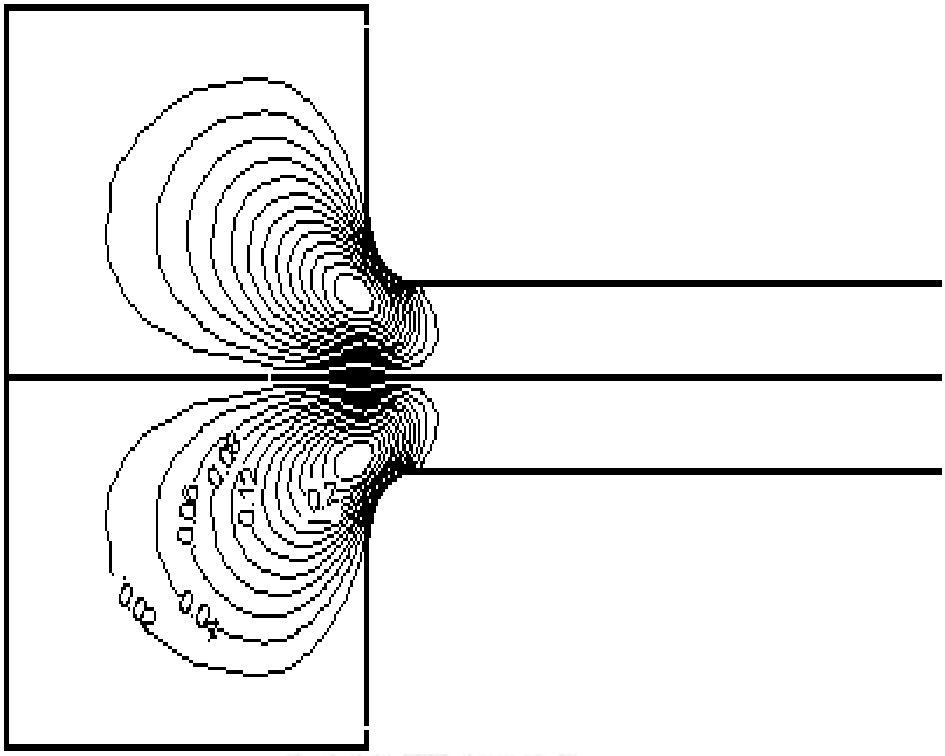

(c) u_y

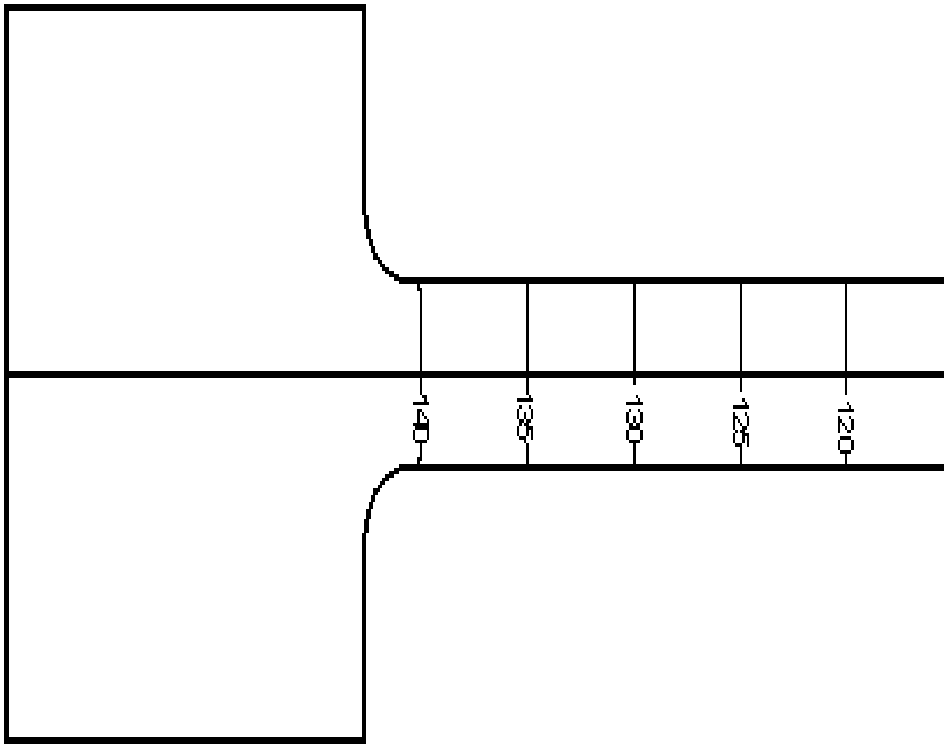

(d) p

Figure 4.34 Line contour of Slip at $\alpha = 0.1$ and $\mathrm{II} = 2.3$, Rounded corner, Newtonian fluid

4.6 Conclusions

For the results of slip effect in 4:1 contraction problem, it is found that the optimum slip coefficient of all *We* is 0.1 if the appropriate critical II is adjusted. The appropriate values of the slip coefficient and the second invariant cause the peak of shear rate lower than no-slip case. Hence it can be concluded that the slip well reduces the stress along the wall. In the same direction, when the small *We* is input, the less effect is appeared and this is reversed with high Weissenberg numbers.

The feedback in velocity and pressure at inlet border is introduced to solve the planar two dimensional isothermal incompressible flow of Newtonian fluid after calculation via semi-implicit Taylor-Galerkin pressure-correction finite element method is completed. This treatment simulation of 4:1 contraction problem was a swift termination to get the complete stable solution when compared with regular method of STGFEM and its error was smoothly approaching zero. The result before treatment revealed a big distortion that made the outcome take many time steps to reach converging solution but the computing after remedy presented the positive manner of pressure and velocity that can be causing flow movement potentially appear like a virtual occurrence. After FPDVF has been implemented and utilized, the obvious improvement suggests an appropriate way to solve such a contraction flow with no irregular effect.

For the slip effect study of 4:1 contraction problem, it is investigated that the optimum slip coefficient for rounded corner meshes of Newtonian fluid is 0.1 for appropriate critical II. The peak of shear rate and vortex size can be reduced in case of choosing right slip coefficient and second invariant. In addition, the higher α and II presented more oscillations that led to the phenomenon of shark skin.

CHAPTER 5
SIMULATION OF DIE-SWELL FLOW

This study is aimed at creeping die-swell flow for Oldroyd-B fluid in two-dimensional axisymmetric coordinate system which is a complicated problem to execute for strong elastic fluid. Hence, the technique of feedback is adapted for fulfillment to access high relaxation time. The governing equations were solved via a combination of semi-implicit Taylor-Galerkin pressure-correction finite element method (STGFEM) and feedback condition which well predicts the velocity field, pressure and free surface paths. Some extra techniques for instant velocity gradient recovery scheme and streamline-Upwind/Petrov-Galerkin (SUPG) method were employed to improve the stability of solutions. For each time step after velocity field is computed, the specific region of die-swell jet is adjusted whilst finite triangle elements in this area were re-meshed. The calculation was terminated with a limit value of Weisenberg number that made the peak of shear stress grown up to infinity at die exit junction. To reduce shear force, the alternative velocity and pressure boundary techniques suitable to control free surface bulge were introduced to modify entrance boundary. Ultimately, the benchmark of swelling ratio with analytical and other literatures was presented in positive direction and it got along well with theoretical prediction.

In this chapter, the die-swell problem of Newtonian fluid and polymer melt is set up for simulation of extrudate process in order to survey physical behavior of flow. The free surface shape is computed with streamline prediction method and some solutions inside die near entrance region are picked up and reinforced at inlet boundary condition. This feedback of pressure-driven velocity flow is taken to support the calculation of free surface path. Since fluid motion shown complex deformation when it confronts with intermediate border between stick and slip boundaries, the diameter of extrudate for viscoelastic problem is varied when the property of liquid gets more flexibility. The calculation of swelling ratio is computed by the semi-implicit Taylor-Galerkin pressure-correction finite element method (STGFEM) and the treatment of pressure-driven velocity feedback.

For die-swell problem of polystyrene samples [39] in extrusion process, the singularity point was measured by capillary viscometer, which presented the effect of molecular weights on swelling ratio but it got no significance when the aspect ratio L/D (length/diameter) was changed. Consequently, the analytic theory [36] of free surface method under integral transforms was studied for extending stick-slip shape in die. When the flow passes a stick boundary to a free surface, the singular point displays a severe shear stress and steep velocity gradients. To reduce this effect, Okabe [40] has illustrated the semi-radial singularity mapping theory with displaying stress and strain near the singularity. The restriction of analytical solution is not solved widely for various liquids due to the limitation of experiment. As such, so many numerical methods were proposed for appraisal of the surface shape through complex flow. The die-swell or short die problem is a state of art study for wire coating flow [94].

To demonstrate the complicated behavior of fluid, the rheological equations and material functions are calculated with the least error approximate solutions such as finite difference (FDM), finite element (FEM) [5, 95, 96], and finite volume methods (FVM) [8, 14, 68, 69]. These numerical schemes are discretizing techniques that transform continuous equations to a system of linear equations. Some constitutive models of viscoelastic fluid are the form of nonlinear partial differential equations that are extremely difficult to solve through analytic methods. Normally, the flow through abrupt surface of die-swell case is deformed rapidly to make shear stress grown up to singularity near the die exit. Thus, one numerical research to improve accuracy convergence of solutions was adopted by boundary singularities of integral equation method [42] with free surface scheme for viscous slow flows whilst a technique of mesh refinement [44] on elements at the singularity was applied. Then Crochet and Keunings [6] have considered slit, circular, and annular dies for Newtonian and Maxwell fluids by a mixed FEM. After exploration of outcome, it showed that the numerical solution gave the result far from real phenomena so Silliman and Scriven [29] have presented a slip condition on die wall to make the result look more real. The same as Phan-Thien [32] who have exhibited the fact of wall slip on extrudate swell and furthermore, the influence of thermal [48] impacted free surface shape. Since the

mathematical model of Navier-Stokes and constitutive equations are spatial and time dimensions for multi-variables in terms of velocity, pressure and stresses the couple mode was applied through fractional step method by means of semi-implicit Taylor Galerkin finite element method (STGFEM) [34, 67] and the positive result of feedback pressure-driven velocity flow [28] has been presented for the Newtonian fluid through the abrupt 4:1 contraction flow of rounded corner geometry.

In this research, the application of die-swell flow on extrusion processes is considered with numerical method of streamline prediction scheme and theoretical approximation. Changing suitable velocity boundary scheme is added to estimate die-swell shape as an acceleration to drive solution fast approaching convergence. The numerical solution of STGFEM has been employed to solve the Navier- Stokes equation of Newtonian and Oldroyd-B fluids. Moreover, the stability of approximated solutions is supported by local gradient recovery and the streamline-upwind Petrov/Galerkin techniques under two dimensional axisymmetric isothermal incompressible flow. The solution is recomputed by gradual increase of Weisenberg number (*We*) to the highest limit. In addition, the pressure-driven velocity flow method is taken to solve the intensive *We* before the final prediction of swelling ratio is compared with other literatures [37, 46, 73, 89, 97, 98].

5.1 Governing Equations

The conservation of mass and momentum under incompressible isothermal viscoelastic flow without gravity is maintained in term of Navier-Stokes equations for two-dimensional axisymmetric system. The dimensionless equations of continuity equation (1), motion equation (2) and constitutive equation of viscoelastic fluid for Oldroyd-B model [55] are written as shown in [67].

5.2 Numerical Scheme

The numerical method for this work is based on semi-implicit Taylor Galerkin pressure-correction scheme, which is a fractional step to solve nonlinear momentum equation due to the coupled mode of velocity and pressure on a finite element standard. The non-dimensional differential equations (2.10), (2.11) and (2.28) are discretised to the system of linear equations for solving velocity field and stress assembly via Jacobi iterative algorithm while pressure was calculated with Cholesky decomposition technique. In addition, the streamline prediction method and alternate velocity boundary condition (Feedback STGFEM) are applied to adjust swelling path precisely.

5.2.1 Semi-implicit Taylor-Galerkin Pressure-Correction Finite Element Method

The Navier-Stokes equation (2.10) and constitutive form of Oldroyd-B equation (2.28) were estimated with the calculation of STGFEM, which is split computing to three stages per time step. The time derivative term is expanded with FDM while the spatial component is transformed by the weight residual of standard Galerkin FEM and then the resultant structure yields partial differential equations (3.32)-(3.37).

To compute the solution of velocity and pressure, steps 1a, 1b and 3 are approximated by Jacobi iterative method whereas step 2 is determined by Cholesky decomposition scheme before the local velocity gradient recovery and the streamline-upwind Petrov/Galerkin techniques are calculated to stabilize the approximate solution. Finally, free surface is predicted by the streamline prediction method and the alternative velocity boundary technique is considered to improve the swelling ratio by feedback condition or Feedback STGFEM.

5.2.2 Feedback of Pressure-Driven Velocity Flow of Die-Swell

In Chapter III, the feedback technique is suitable for adjusting proper boundary condition at inlet flow when pressure forces motion to move smoothly through converge solution. For die-swell problem, the technique how to re-feed nodes is shown in Figure 5.1. This method is well defined for such a problem of viscoelastic fluid since it gradually reduces the differential time step until the swelling ratio approaches to analytic result.

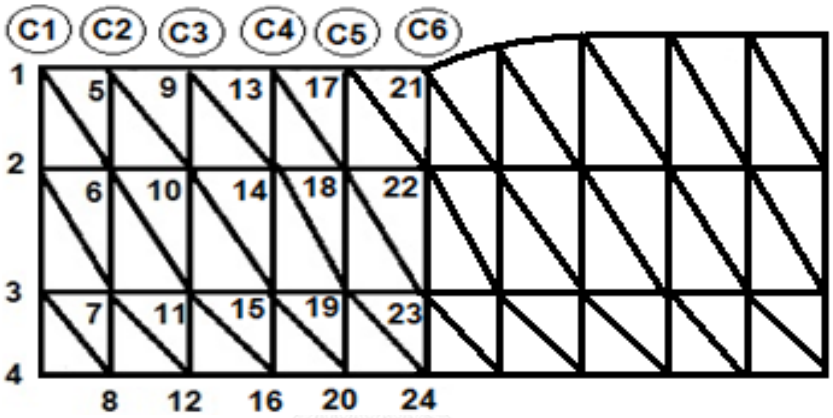

Figure 5.1 Mesh geometry with node number, die-swell flow

5.2.3 Free Surface Prediction

For extrudate swell problem, streamline prediction scheme is employed to predict the free surface path in integration form before it is discretied by Simpson's rule. The numerical computation of swelling ratio (χ) is as good as theoretical technique from Tanner [89]. The unknown surface shape is modified every time step until the least square and the maximum errors are acceptable. The benchmark for swelling ratio of theoretical result, feedback STGFEM and other literature results is explored.

5.3 Problem Specification

There are two specific problems are considered in this chapter, that are stick-slip and die-swell flows. The geometry of full domain as Figure 5.2 is provided to two identical portions that are symmetric shape of top and bottom parts so the half die is represented to generate small finite elements. Both problems have the same boundary condition except the free surface boundary for stick-slip flow is set to zero. The velocity profile at inlet of both cases is still conserved parabolic motion that is known as Poiseuille flow.

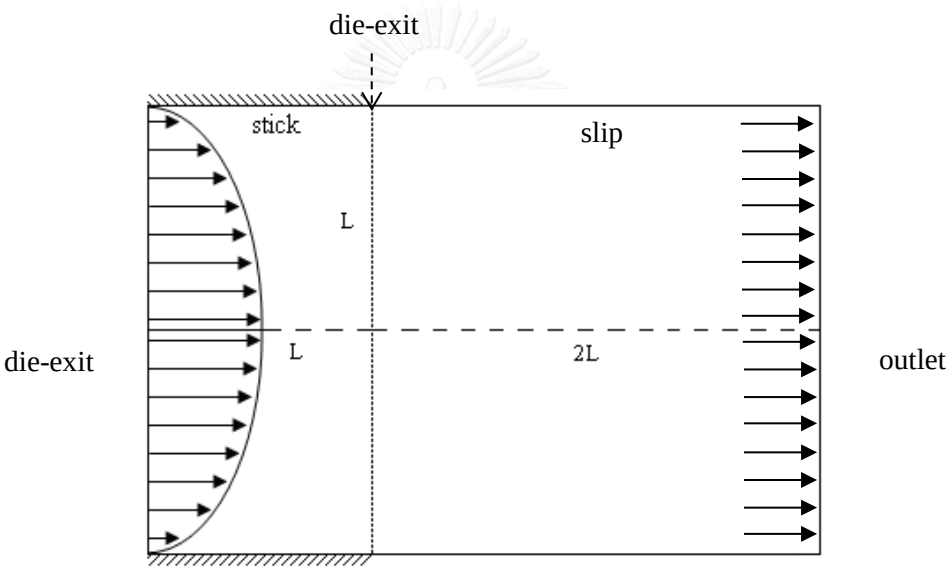

Figure 5.2 Schematic of stick-slip flow

5.3.1 Stick-Slip Flow

The stick-slip problem [37, 67] is first used before the computation keeps going until the final flow is transformed to extrudate shape with the same mesh pattern. Firstly the designation of mesh style for stick-slip geometry was generated to small sub-cells under 1944 elements and 4033 nodes as shown in Figure 5.3 with the smallest size (Δr) of finest element to be 0.025. Before it is run, the boundary conditions are defined as: Poiseuille flow at the inlet, zero pressure at free surface, null radial velocity for all borders and zero shear stress at symmetry line. The standard shape is created with 1L for entry section and 2L for exit portion as displayed in Figure 5.4.

The boundary conditions of stick-slip case are set by imposing Poiseuille flow of equation (5.1) at the inlet. The die length is long enough to complete developing flow so it still maintains parabolic flow pattern. The inlet conditions of stresses are represented in equation (5.2) while the boundary at symmetric line ($r = 0$) are $u_r = 0$ and $\tau_{rz} = 0$.

$$u_z = 1 - r^2 \text{ and } u_r = 0 \tag{5.1}$$

$$\tau_{rr} = 0,\ \tau_{\theta\theta} = 0,\ \tau_{rz} = \mu_1 \frac{\partial u_z}{\partial r}, \text{ and } \tau_{zz} = 2We\mu_1 \left(\frac{\partial u_z}{\partial r} \right)^2 \tag{5.2}$$

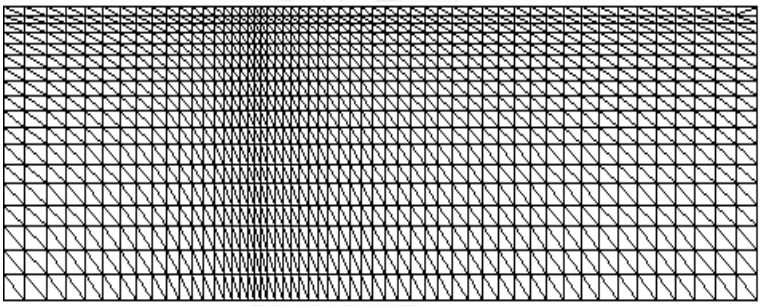

Figure 5.3 Mesh pattern, 1944 elements, 4033 Nodes

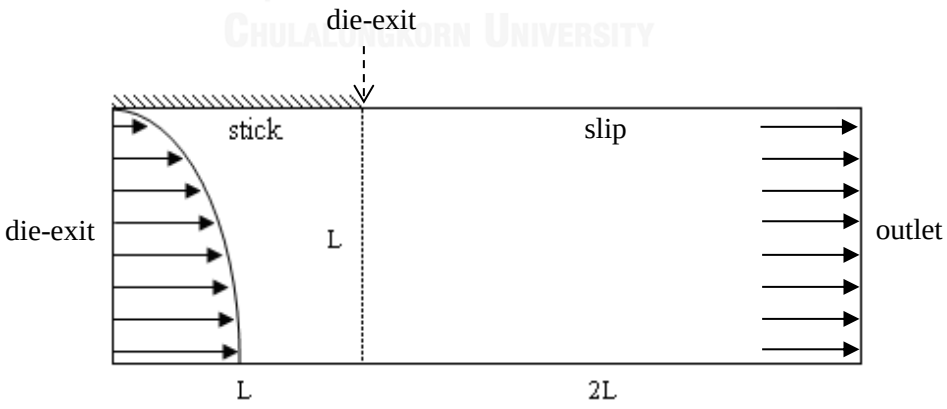

Figure 5.4 The half axisymmetric stick-slip flow

5.3.2 Die-swell Flow

Since die-swell problem has the same inlet boundary conditions as stick-slip case, equation (5.1) and equation (5.2) are appeared as well. The solutions are executed at the top half-plane as Figure 5.5. To gradually improve velocity at inlet, the temporary solution was recalculated by feedback treatment before the swell prediction be effective.

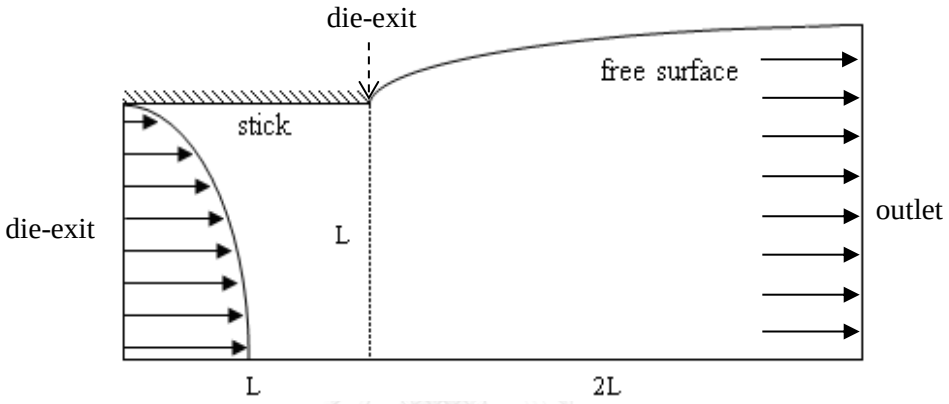

Figure 5.5 The axisymmetric die-swell flow

5.4 Results

5.4.1 Stick-Slip Result

In order to avoid duplication outcome of stick-slip flow, the data of fine mesh is chosen to display the final solution. The program was terminated after *We* = 2 so the line contour plot for upper half plane is shown in Figure 5.6. Figure 5.6(a) shows the velocity contour, which is normalized the maximum value to one unit at the centre of die. The axial velocity (u_z) with no-slip at die wall is Poiseuille flow at inlet and gradually adjusting to plug flow meanwhile the computation. The velocity u_r line plot of Figure 5.6(b) vanishes at all boundary sides and displays closed contours of small value in the neighborhood of the singularity. Figure 5.6(c) shows a contour plot of pressure and the maximum value is illustrated at the inlet boundary, with representation of the pressure drop across the flow. Shear stress τ_{rz} over the top die wall remains negative until it reaches the singularity, where a dramatic jump with the

positive extreme value is observed, before reducing to zero at the top extrudate boundary as depicted in Figure 5.6(d). Axial normal stress τ_{zz} at the lower boundary is much higher than the die exit as shown in Figure 5.6(e). Figure 5.6(f) displays a negative value of radial extra-stress τ_{rr} distributed through whole flow in the mean time the maximum peak stress is located at the singularity. $\tau_{\theta\theta}$ indicates closed contours of small constant value in the neighborhood of the singularity as Figure 5.6(g).

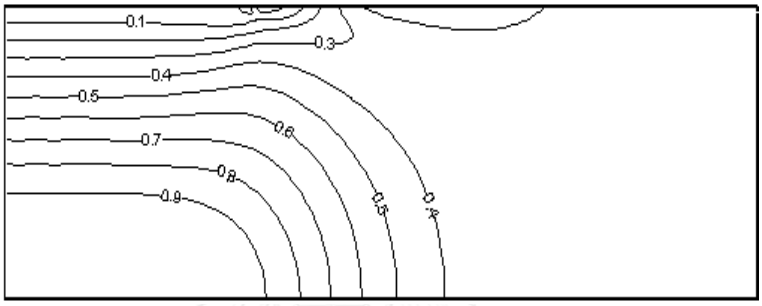

(a) u_z

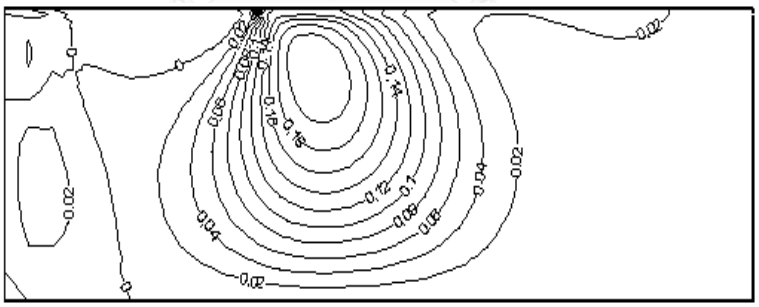

(b) u_r

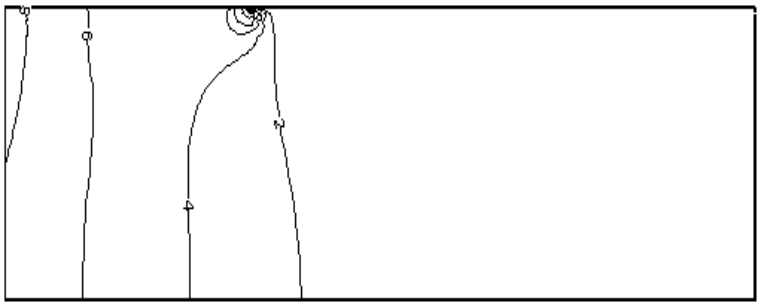

(c) p

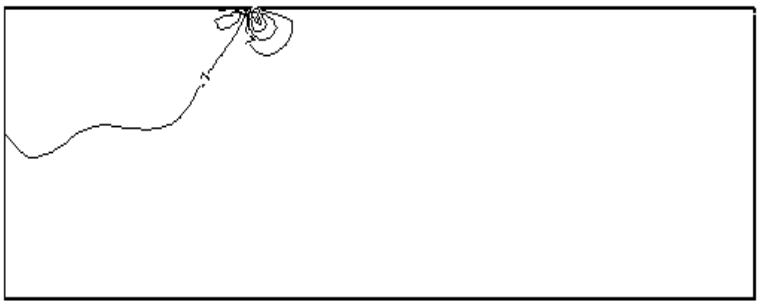

(d) τ_{rz}

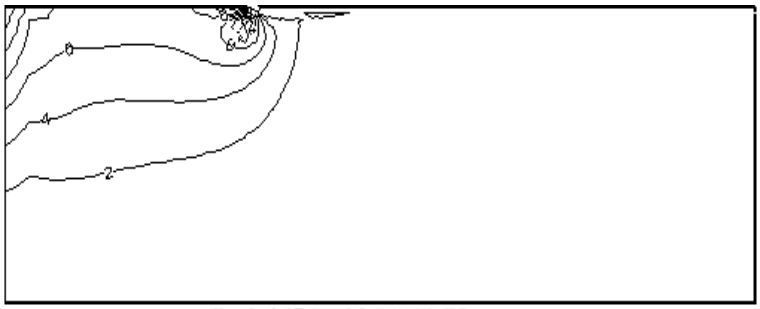

(e) τ_{zz}

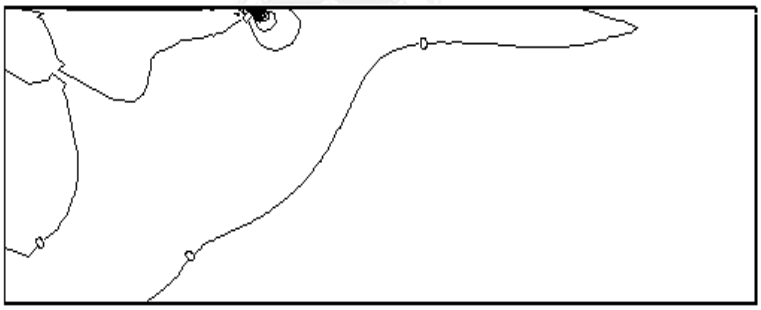

(f) τ_{rr}

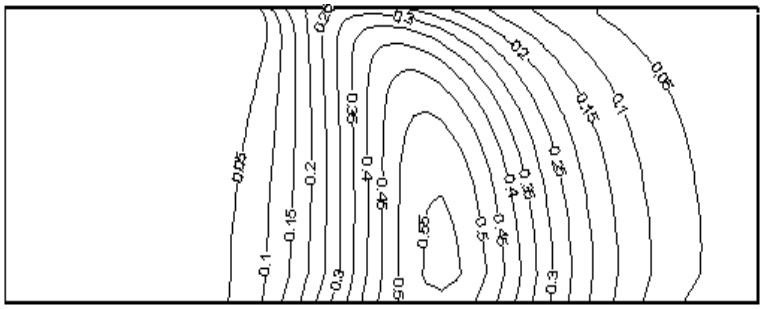

(g) $\tau_{\theta\theta}$

Figure 5.6 Line contour of Oldroyd-B fluid at *We* = 2, Stick-slip problem

5.4.2 Die-Swell Result

The simulation of die-swell problem is evaluated with STGFEM including feedback condition for fine mesh that has been utilised earlier by Ngamaramvaranggul and Webster [67]. This technique is useful for running high *We* of Oldroyd-B fluid. For this flow, it is a complex constitutive model so the termination of numerical process is limited at low *We*. The benchmark of swelling ratio after feedback treatment is approached to theoretical estimation by Tanner [89] and in addition it spends less time step. For Newtonian fluid, the swelling ratio of Feedback STGFEM is identical to analytical prediction and there is no significant disparity when compared with the solution of Ngamaramvaranggul and Webster [67] but the solution of viscoelastic case for STGFEM with and without Feedback was calculated in terms of swelling ratio χ, normal stress (τ_{zz}, τ_{rr}, and $\tau_{\theta\theta}$) and shear stress τ_{rz} that are identical for both versions but the second invariant II of Feedback STGFEM is higher than STGFEM because the pressure driven velocity adjusted more effect for normal stress in axial direction. The program could run *We* twice as many feedback condition as no treatment constraint that one can compare this result with the limit of termination at $We = 1.$

Figure 5.7 shows the swelling ratio that is varied with *We* from Newtonian fluid ($We = 0$) to viscoelastic flow of $We = 2$. STGFEM including feedback condition can predict the swelling ratio up to $We = 2$ when the Weisenberg number increases step by step at increments of 0.25. The swelling ratios along the exit of top free surface are varied with *We* and all curves are gradually climbed up for the same trend.

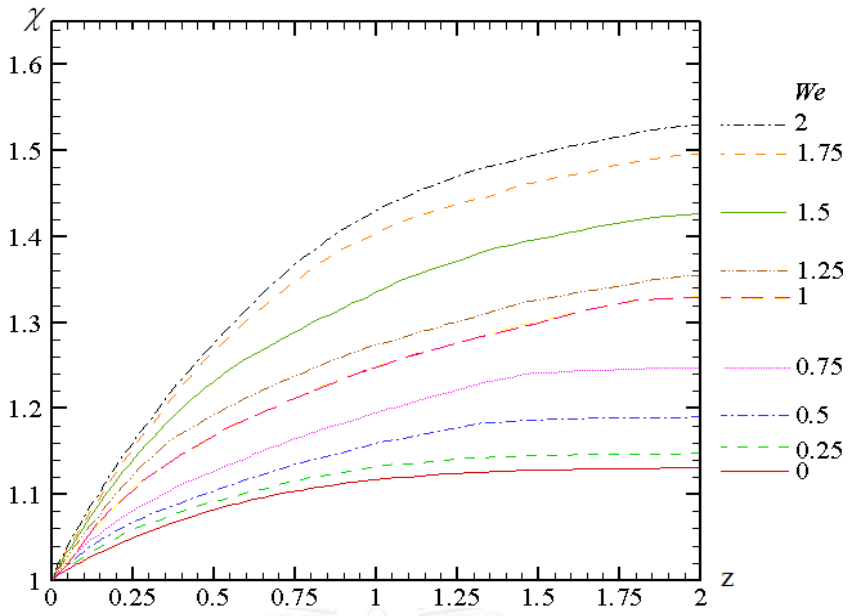

Figure 5.7 The swelling ratio (χ) of Oldroyd-B fluid; variation with *We*

The variation of die-swell geometry with mesh pattern of $0 \le We \le 2$ represents the maximum swell that corresponds to the largest Weissenberg number as display in Figure 5.8. Figure 5.9 and Table 5.1 compares the swelling ratio against other literatures, in terms of increasing Weissenberg number. When feedback scheme is added in STGFEM, the swell ratio is gradually adjusted and reshaped until the free surface is smoother than the basic STGFEM.

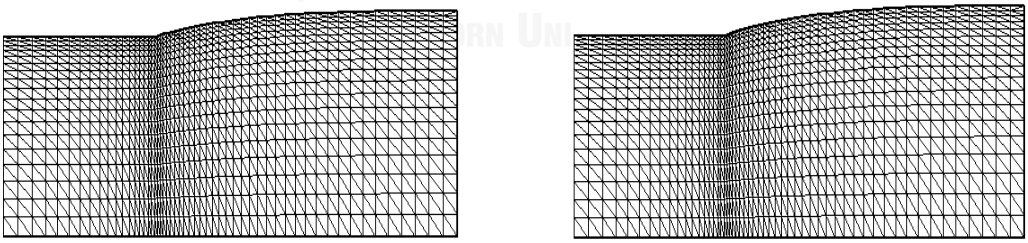

(a) $We = 0$ (b) $We = 0.25$

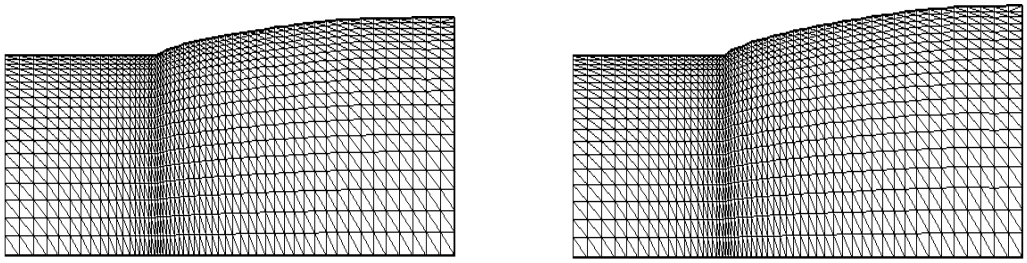

(c) $We = 0.5$ (d) $We = 0.75$

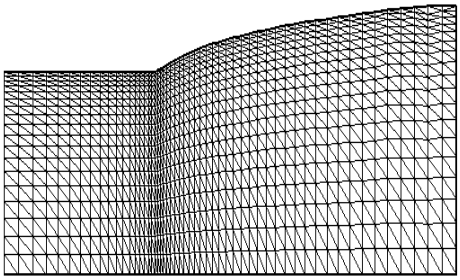

(e) $We = 1$

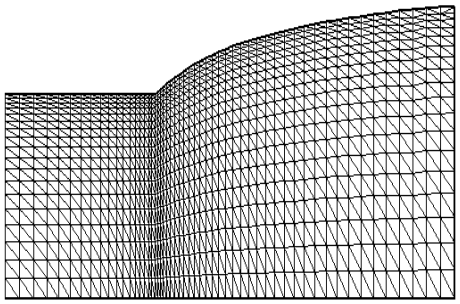

(f) $We = 1.25$

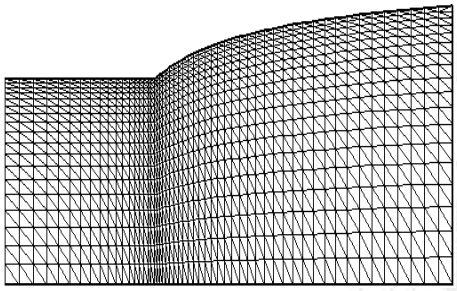

(g) $We = 1.5$

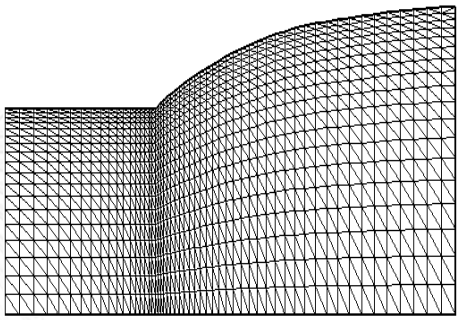

(h) $We = 1.75$

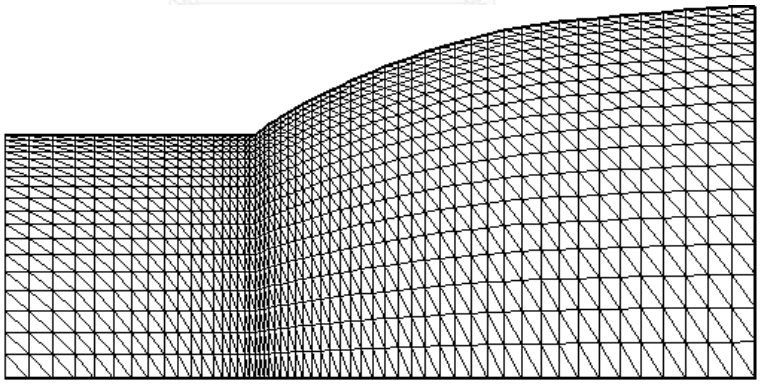

(i) $We = 2$

Figure 5.8 The variation of die-swell geometry; $0 \le We \le 2$

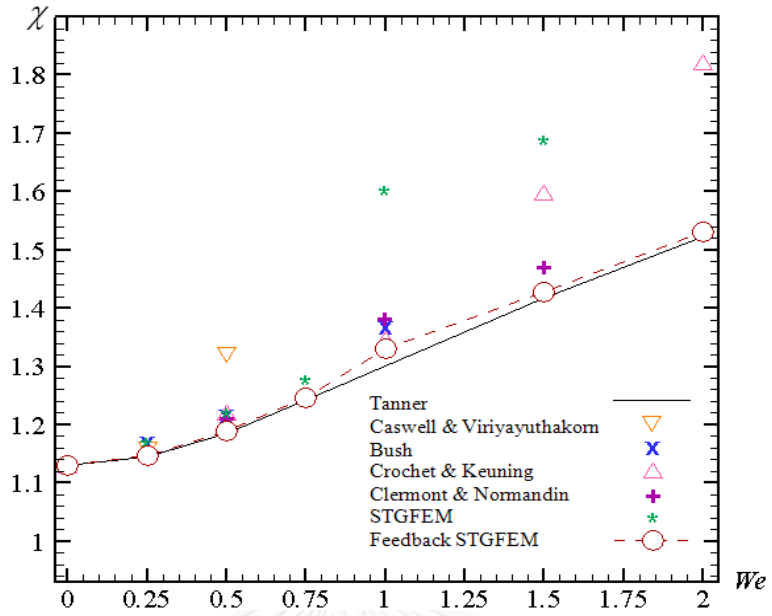

Figure 5.9 The comparison of χ

Since the tendency of swelling ratio for all *We* values has the same trend , the swelling ratio increases when *We* is higher as seen in Table 5.1. As the following result of Feedback STGFEM, the capability of scheme is powerful to get high *We* and gives the best values of swelling ratio when compared with Tanner [89] as illustrated in Table 5.1 and Figure 5.9.

Within the range of $0 \le We \le 2$, all values of pressure, stresses, shear rate and II bear the same inclination that tend to rise up implying that these worth proportion to *We* as shown in Table 5.2. With the increase of *We*, the pressure dragged fluid away to outside with stronger force and resulted in high pressure drop between entry and die exit.

Table 5.1 Benchmark of swelling ratio for various *We*

Swelling ratio	*We*						
	0	0.25	0.5	0.75	1	1.5	2
Tanner [89]	1.131	1.146	1.186	1.242	1.301	1.417	1.523
Caswell& Viriyayuthakorn [97]	1.131	1.161	1.325	-	-	-	-
Butler and Bush [46]	1.134	1.171	1.219	-	1.371	-	-
Crochet & Keuning [6, 56]	1.126	1.147	1.217	-	1.343	1.595	1.817
Clermont & Normandin [98]	-	-	1.210	-	1.380	1.470	1.530
STGFEM [67]	1.130	1.162	1.212	1.268	1.593	1.680	-
Feedback STGFEM [99]	1.131	1.148	1.190	1.247	1.330	1.427	1.530

Table 5.2 The peak values of pressure, stresses, shear rate and II at $0 \le We \le 2$

We	p	τ_{zz}	τ_{rz}	$\dot{\gamma}$	II
0	4.94	12.10	1.06	10.96	28.57
0.25	7.24	12.81	1.95	13.58	46.08
0.5	16.29	13.07	3.85	15.18	60.75
0.75	23.57	13.52	6.09	16.61	71.66
1.0	30.31	13.70	6.83	16.93	71.66
1.25	32.39	14.17	7.72	18.94	89.72
1.5	33.36	14.74	8.05	20.37	104.07
1.75	34.20	17.94	10.16	22.83	130.26
2.0	34.87	18.76	10.91	24.82	153.99

Since the behavior of second invariant (II) and shear rate ($\dot{\gamma}$) of Oldroyd-B fluid for *We* between 0 and 2 are similar to normal distribution. Many figure instances of second invariant and maximum shear rate for $1.25 \le We \le 2$ are presented in Figure 5.10 and Figure 5.11, respectively. II is closely equal to zero and $\dot{\gamma}$ is steady near 5 from z = -1 to -0.01 and then they are overshot to the zenith values at exit die (z = 0) or the singularity point so all curves show the maximum second invariant and the supreme shear rate impact at the singularity location before they sharply reduce to constant value from z = 0.04 to z = 2. Once the fluid has passed exit die, the peak values of shear rate rise immediately and the rate of growth for peak value between $\dot{\gamma}$ and *We* is in linear progression. In addition, the trends of II reduce steeply when fluid passes the stick position to free surface geometry and then II is steady near zero for all *We*. When the Weissenberg numbers increase, the positive extream values of II and $\dot{\gamma}$ rise sharply.

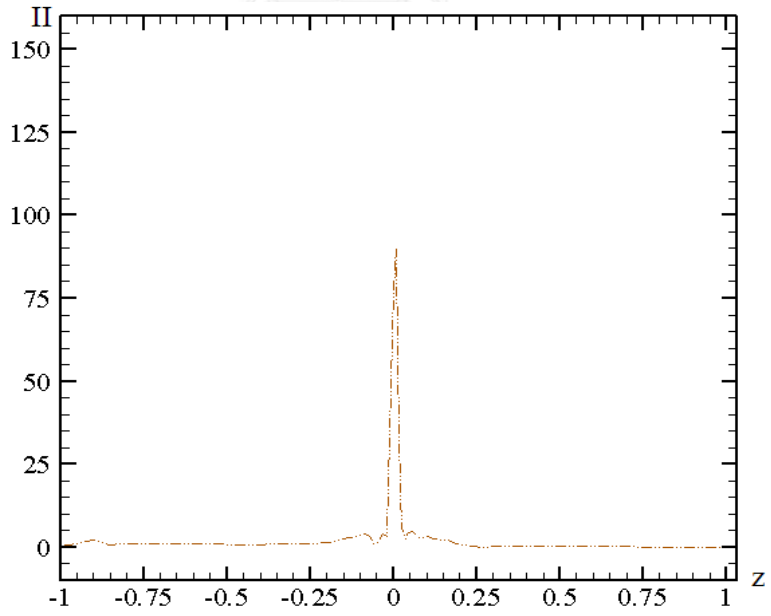

(a) *We* = 1.25

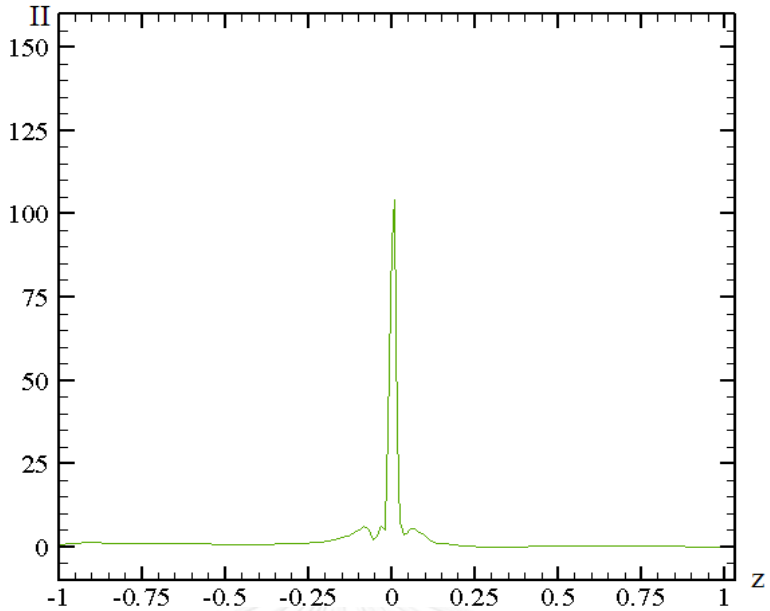

(b) *We* = 1.5

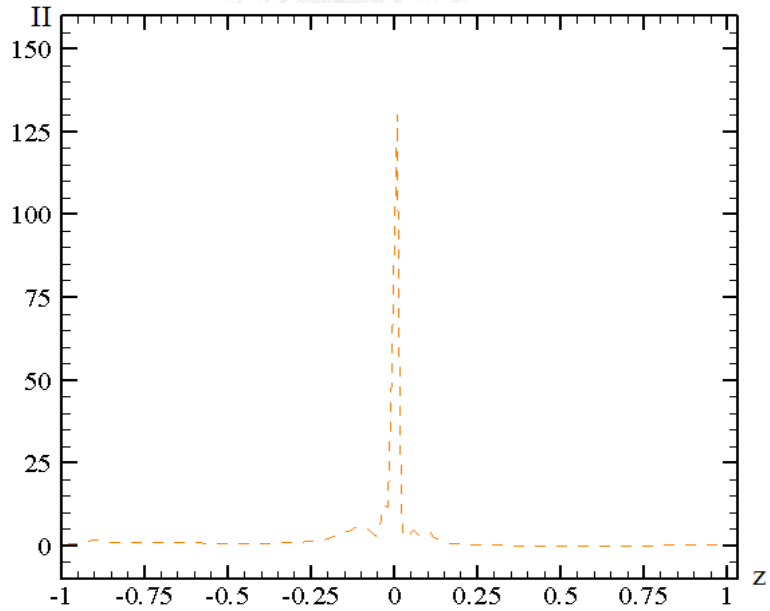

(c) *We* = 1.75

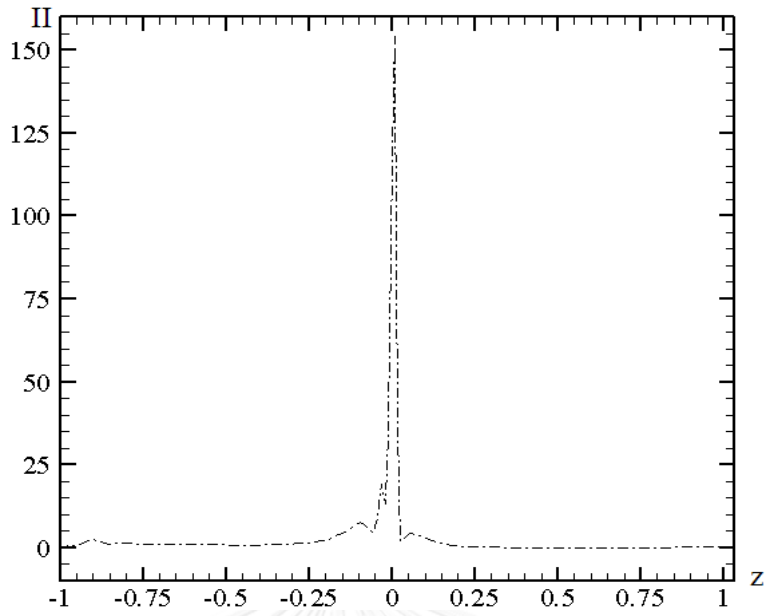

(d) $We = 2$

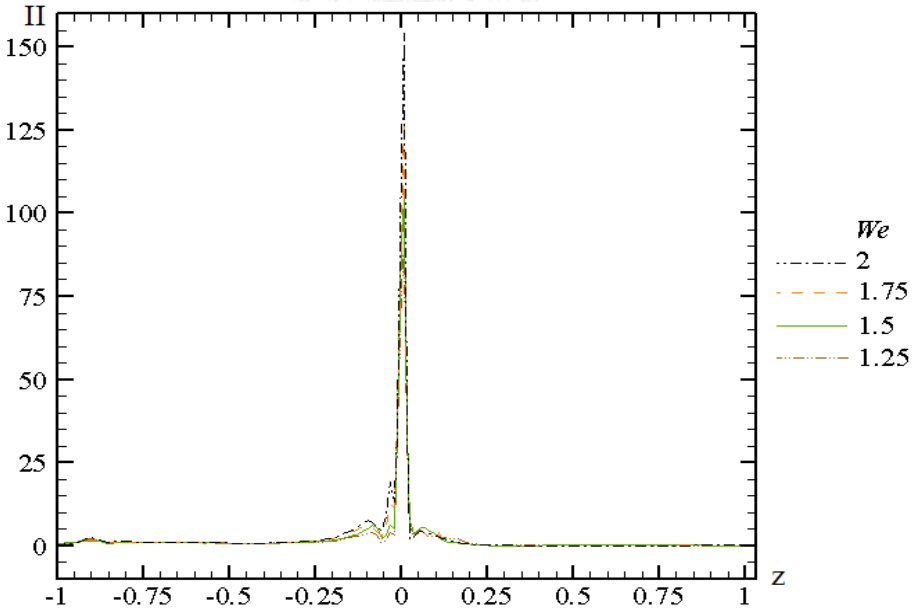

(e) $1.25 \leq We \leq 2$

Figure 5.10 II along the wall

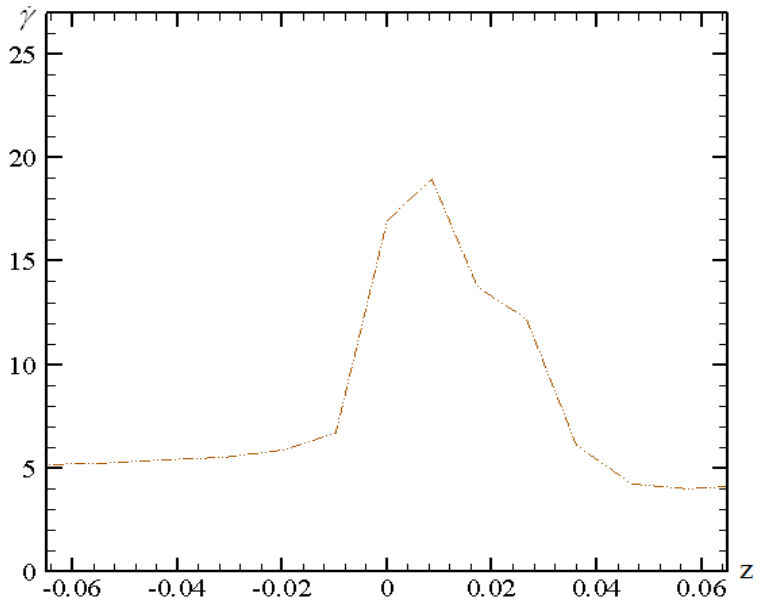

(a) *We* = 1.25

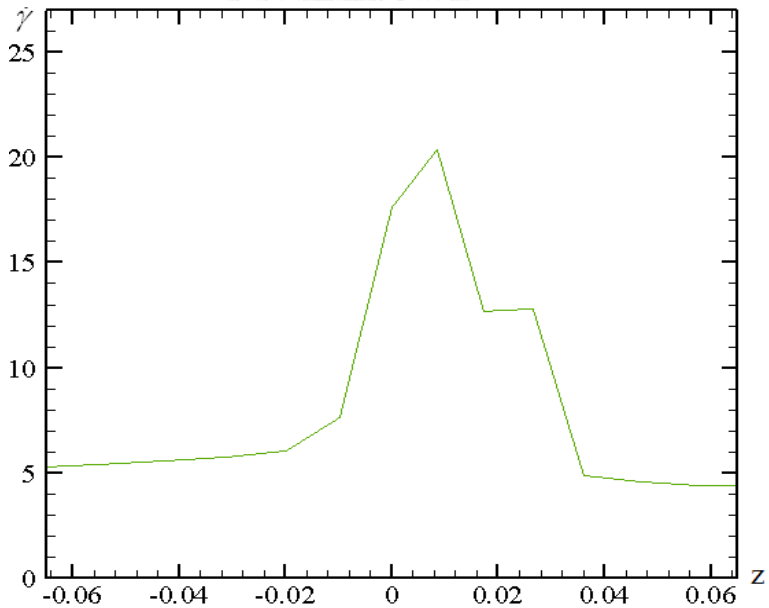

(b) *We* = 1.5

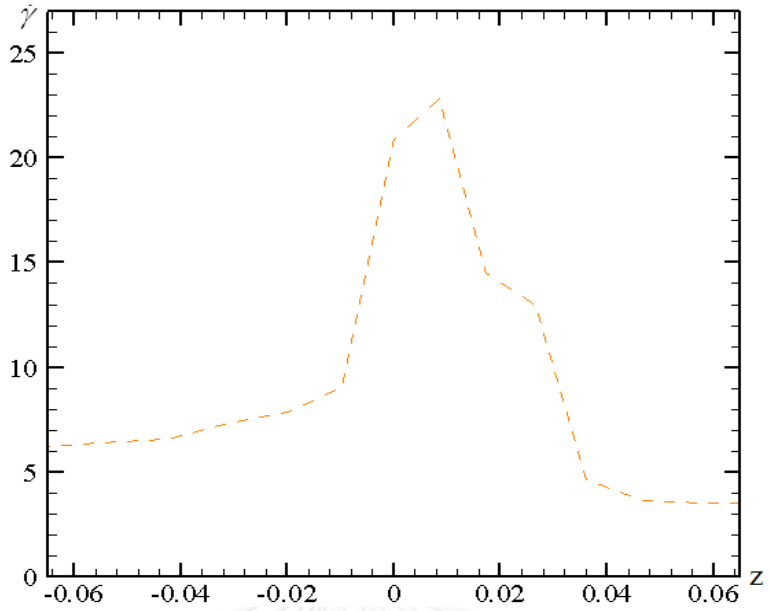
$\dot{\gamma}$
25
20
15
10
5
0
-0.06
-0.04
-0.02
0
0.02
0.04
0.06
z

(c) *We* = 1.75

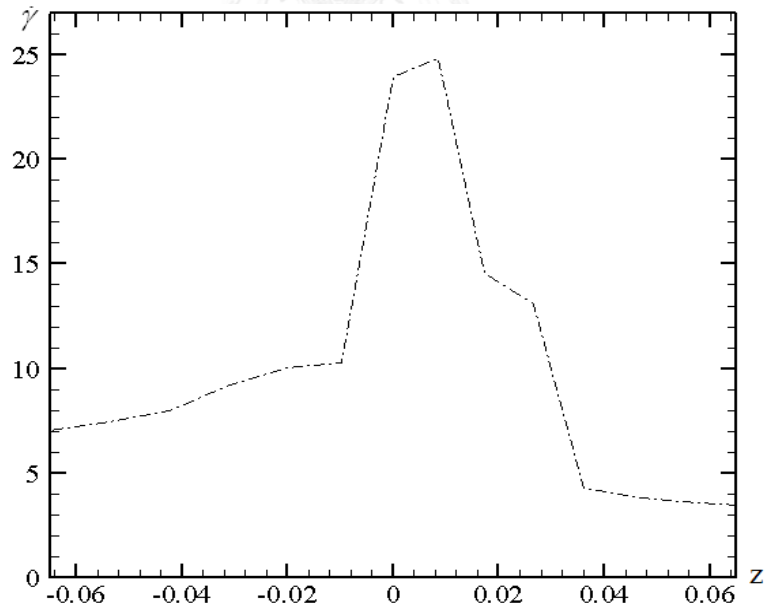
$\dot{\gamma}$
25
20
15
10
5
0
-0.06
-0.04
-0.02
0
0.02
0.04
0.06
z

(d) *We* = 2

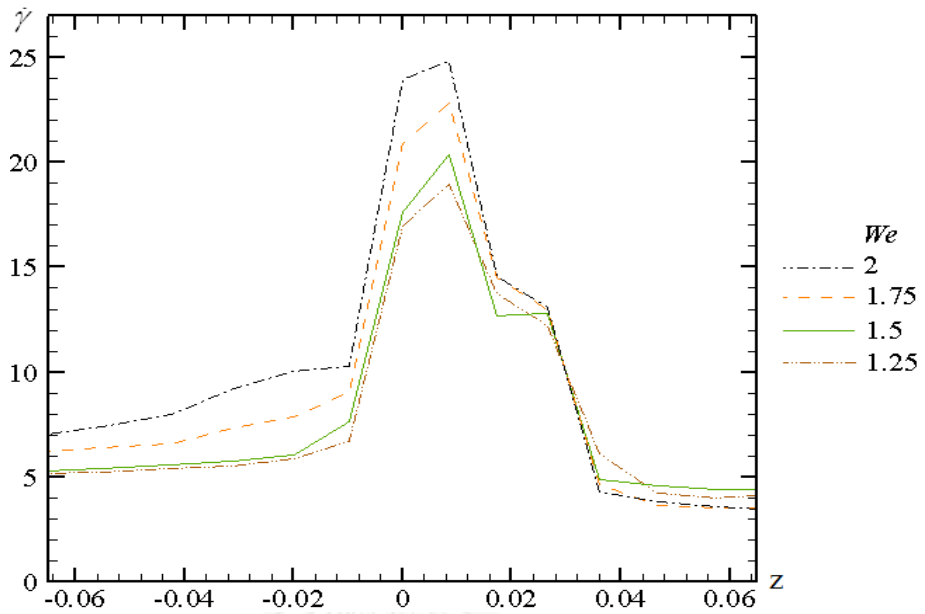

(e) $1.25 \le We \le 2$

Figure 5.11 $\dot{\gamma}$ along the wall

The velocity profiles for die-swell in axial direction and radial axis along the wall are shown in Figure 5.12 and Figure 5.13, respectively. The peak of u_z increases due to the enlargement of *We* as same as for u_r with maxima placed near z = 0.1. According to the viscoelastic fluids, the properties of both viscous and elastic flows are noticed in mode of relaxation time representing the memory of stress behavior. The more relaxation time or larger *We* is concerned, the more retention of flow path is observed affecting the peak relocation of axial velocity and shift-aways. When $We = 1.25$ and 1.5, the settle points are placed near z = 0.35 while the place of peak shifts to z = 0.6 at $We = 1.75$ and 2 as high viscoelatic fluid gathers up velocity and force.

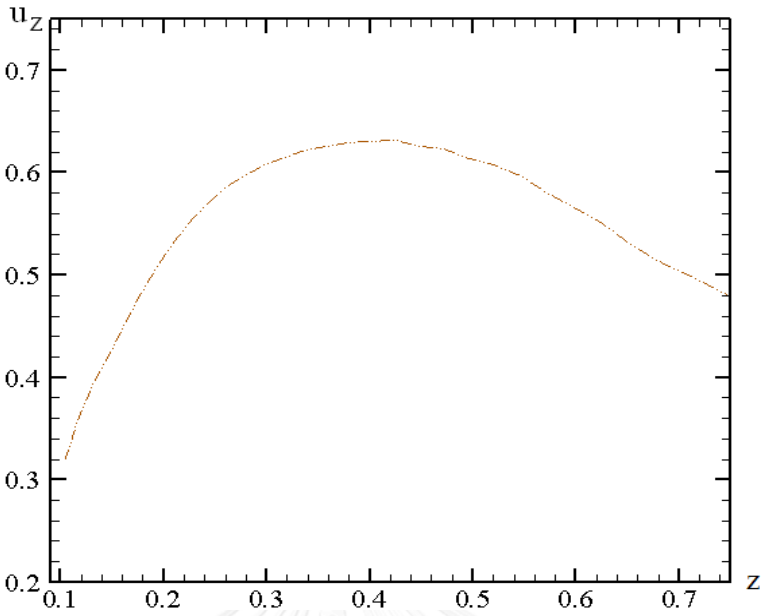

(a) *We* = 1.25

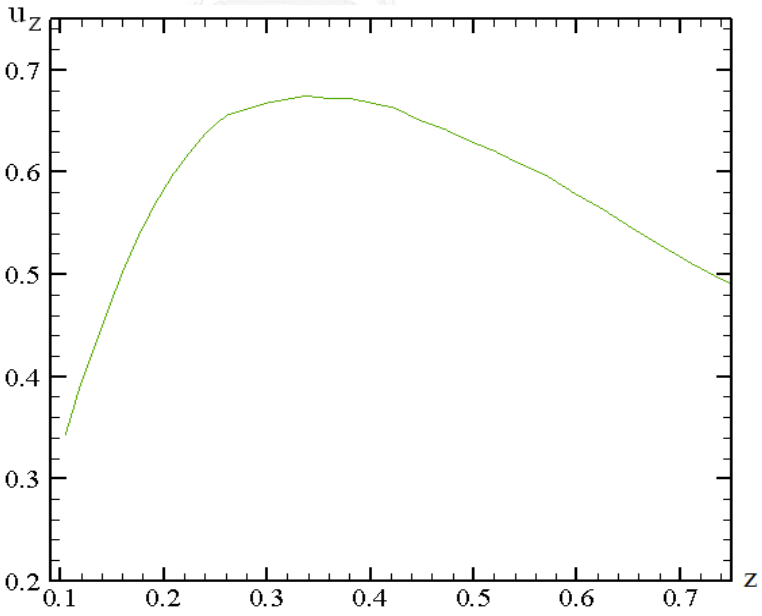

(b) *We* = 1.5

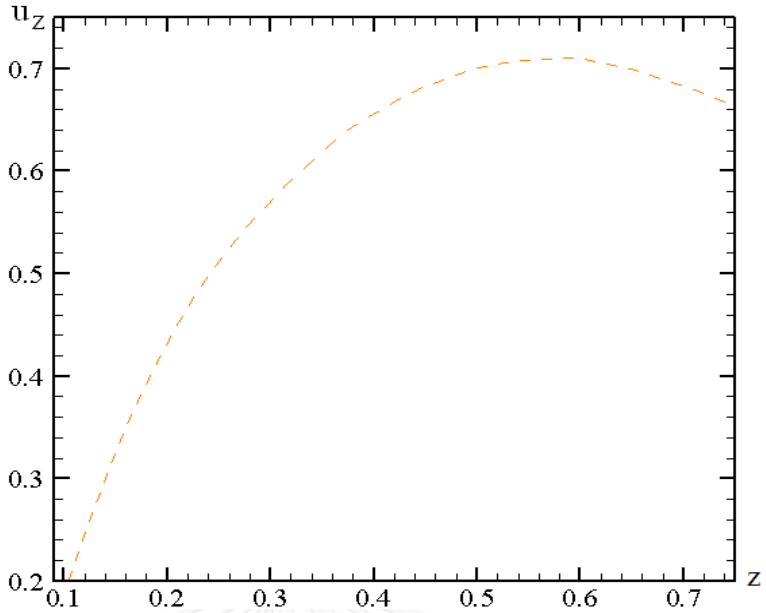
uz
0.7
0.6
0.5
0.4
0.3
0.2
0.1
0.2
0.3
0.4
0.5
0.6
0.7
z

(c) *We* = 1.75

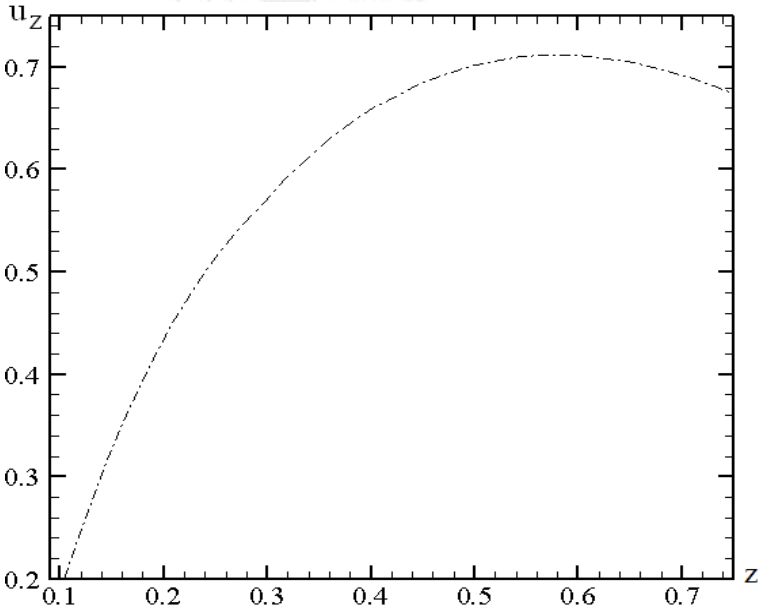
uz
0.7
0.6
0.5
0.4
0.3
0.2
0.1
0.2
0.3
0.4
0.5
0.6
0.7
z

(d) *We* = 2

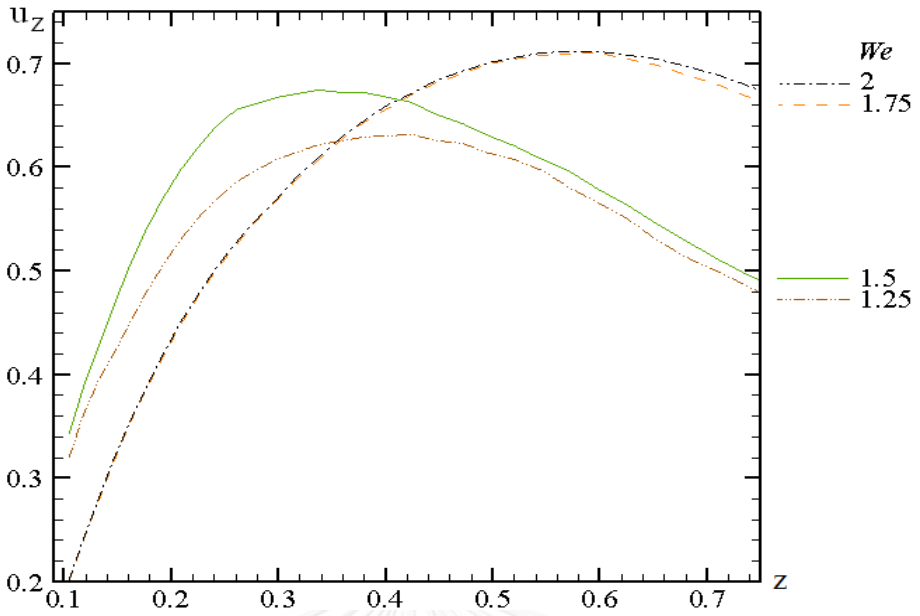

(e) $1.25 \le We \le 2$

Figure 5.12 u_z along the wall

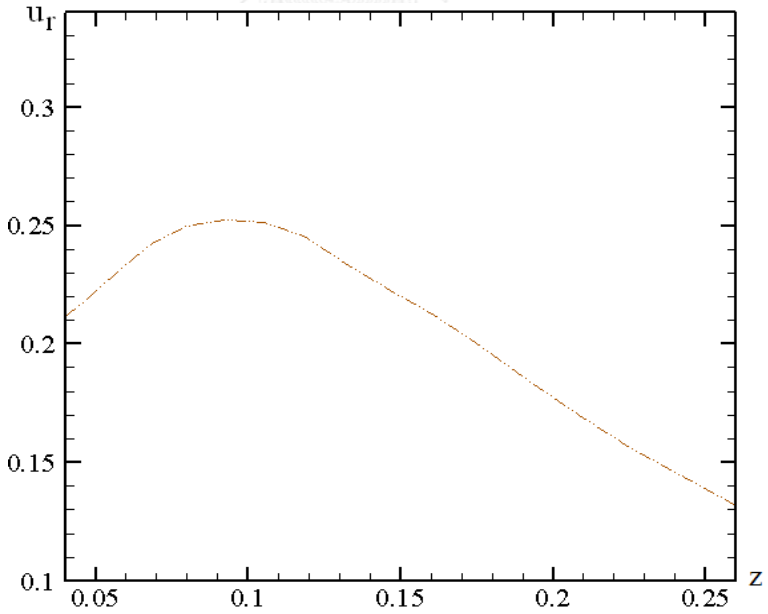

(a) *We* = 1.25

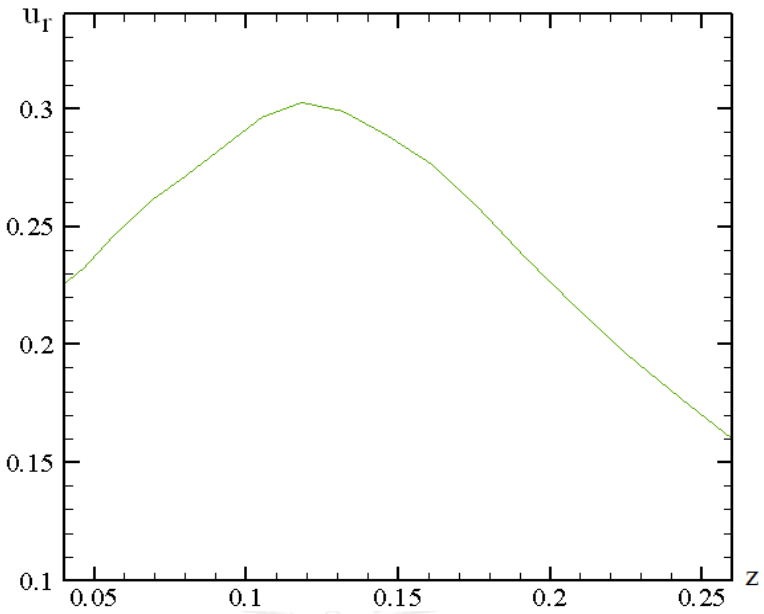

(b) *We* = 1.5

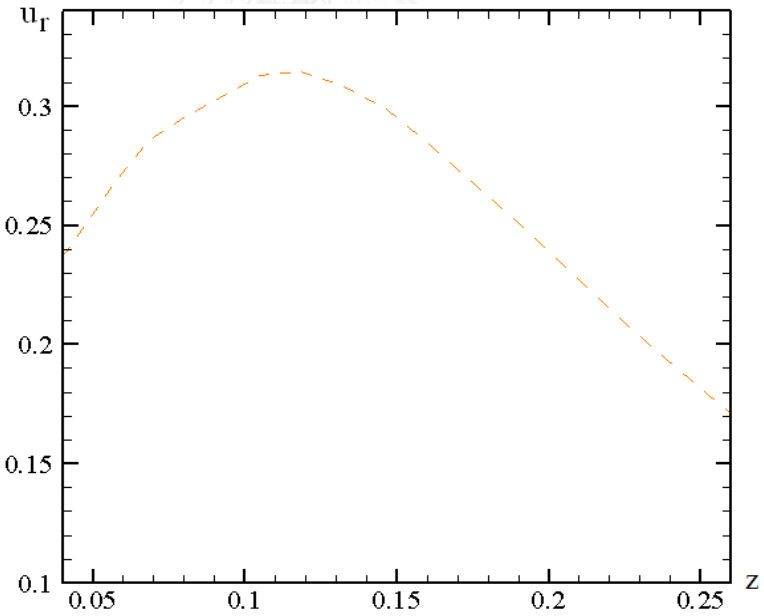

(c) *We* = 1.75

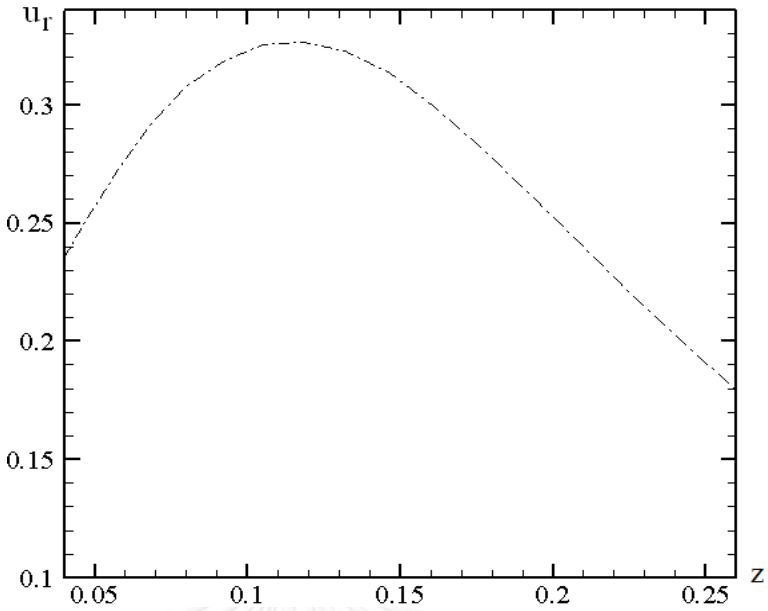

(d) $We = 2$

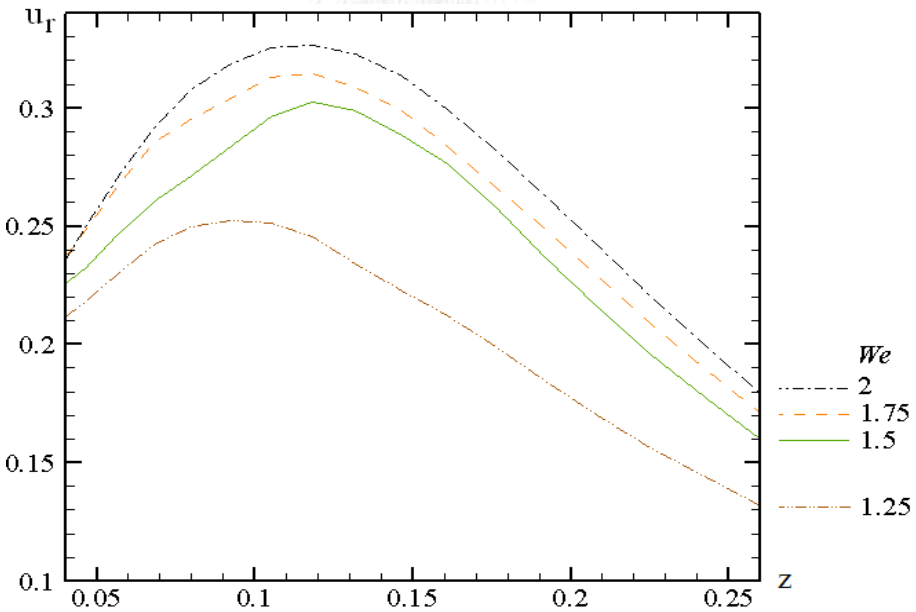

(e) $1.25 \le We \le 2$

Figure 5.13 u_r along the wall

The peak values of shear stress τ_{rz} for all *We* lie near die exit ($-0.03 \le z \le -0.02$) even if *We* is increased but the location of zenith values is the same as seen in Figure 5.14. The shear stress grows up and then drops near z = - 0.25 and the peak values

shoot up for higher *We* values. To reduce similar graphs of other *We*, only one normal stress τ_{zz} along upper die wall is presented in Figure 5.15, which reveals the highest value at z = -0.2 and the peak values of these normal stresses for various *We* are given in Table 5.2.

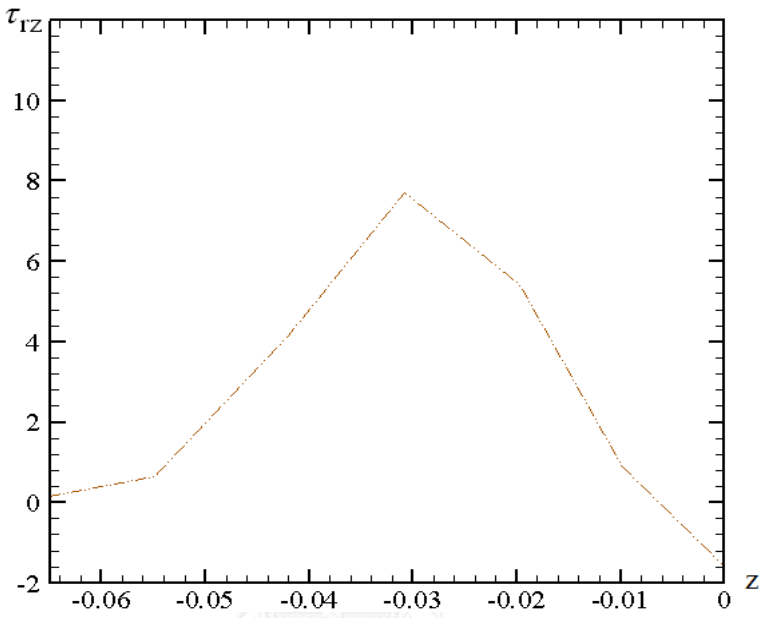

(a) *We* = 1.25

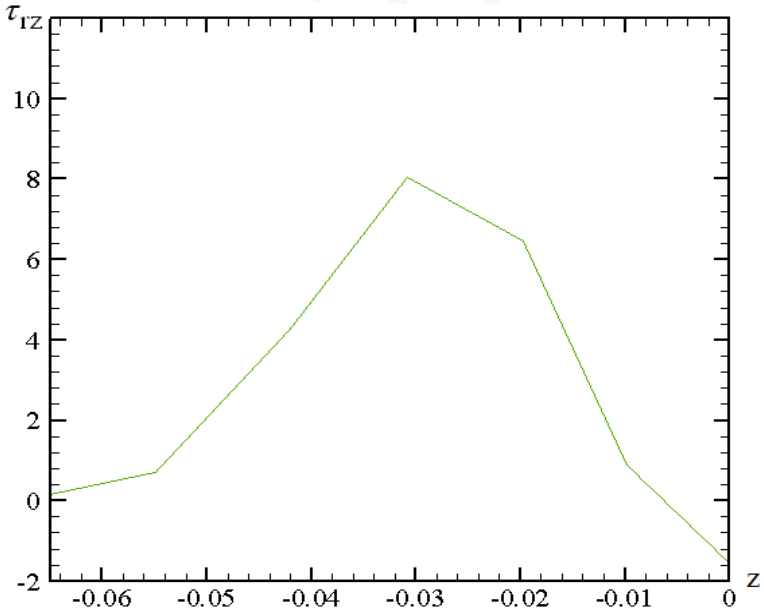

(b) *We* = 1.5

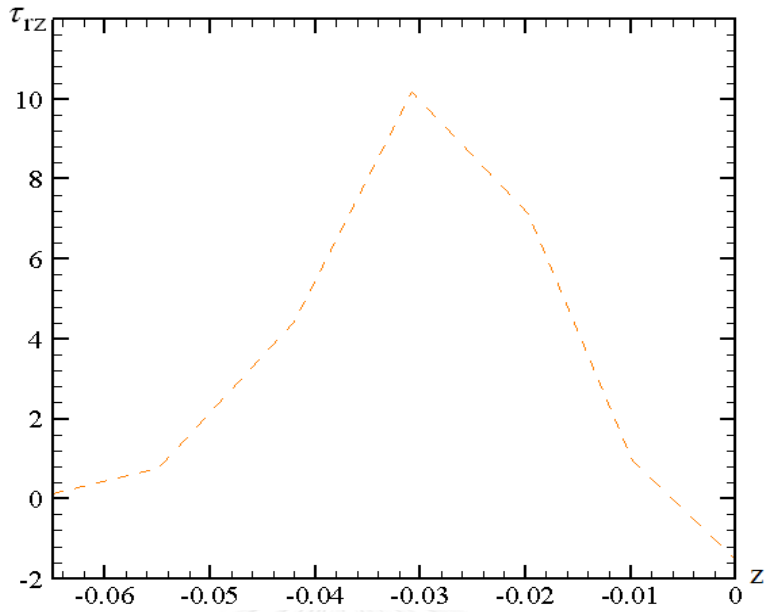
τ_{rz}
10
8
6
4
2
0
-2
-0.06
-0.05
-0.04
-0.03
-0.02
-0.01
0
z

(c) *We* = 1.75

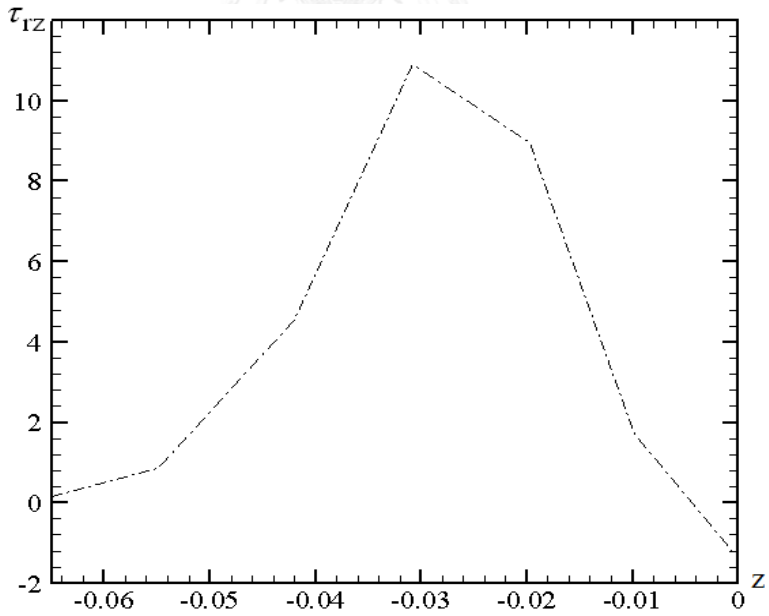
τ_{rz}
10
8
6
4
2
0
-2
-0.06
-0.05
-0.04
-0.03
-0.02
-0.01
0
z

(d) *We* = 2

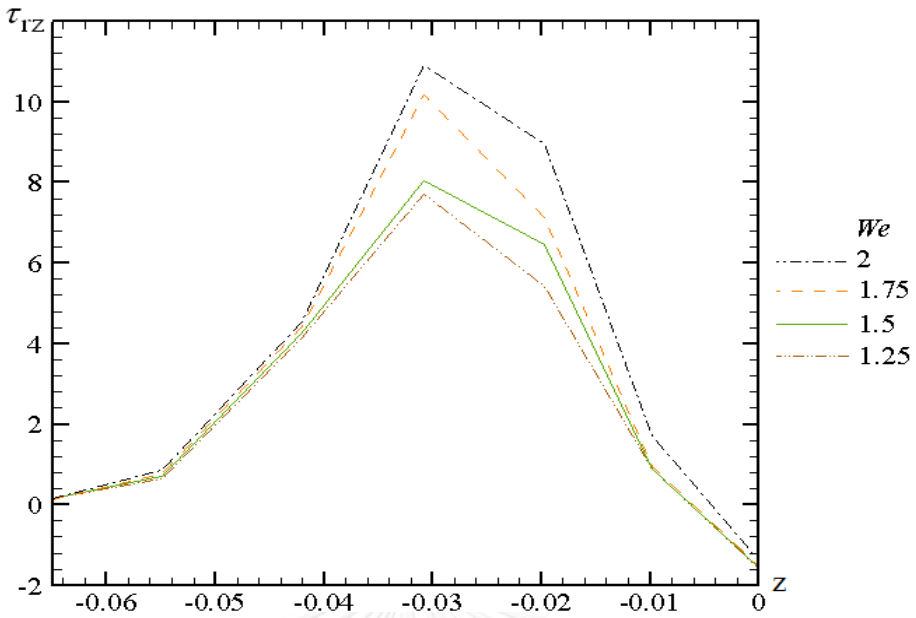

(e) $1.25 \le We \le 2$

Figure 5.14 τ_{rz} along the wall

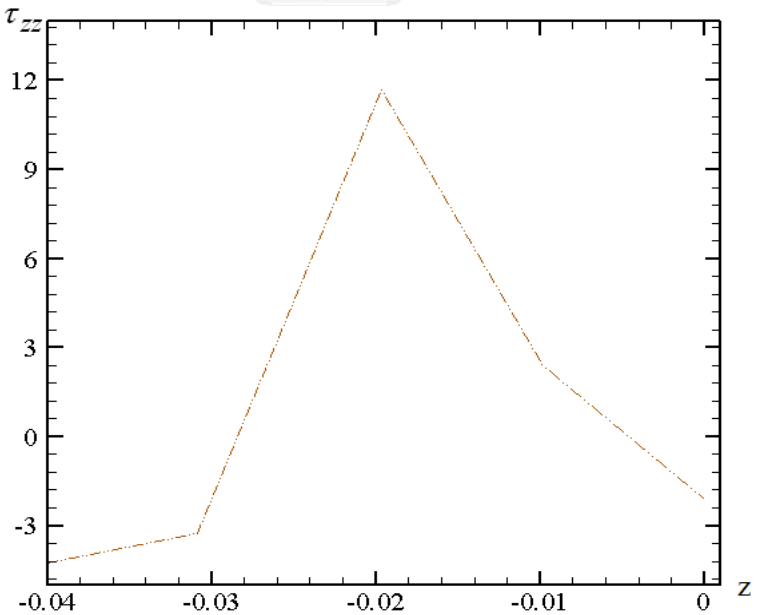

(a) *We* = 1.25

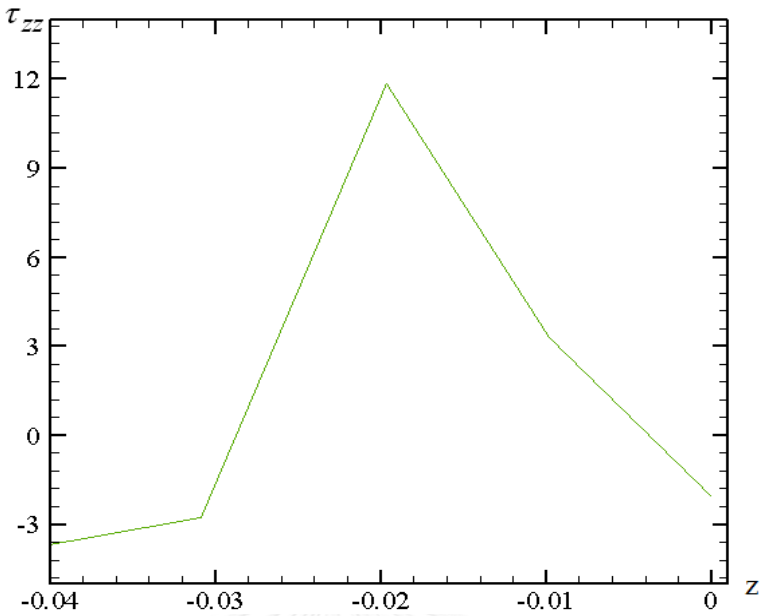

(b) *We* = 1.5

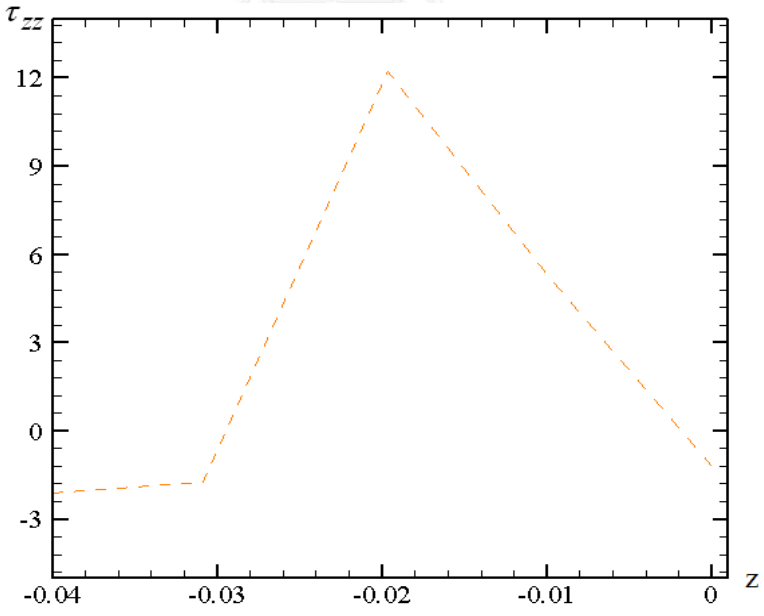

(c) *We* = 1.75

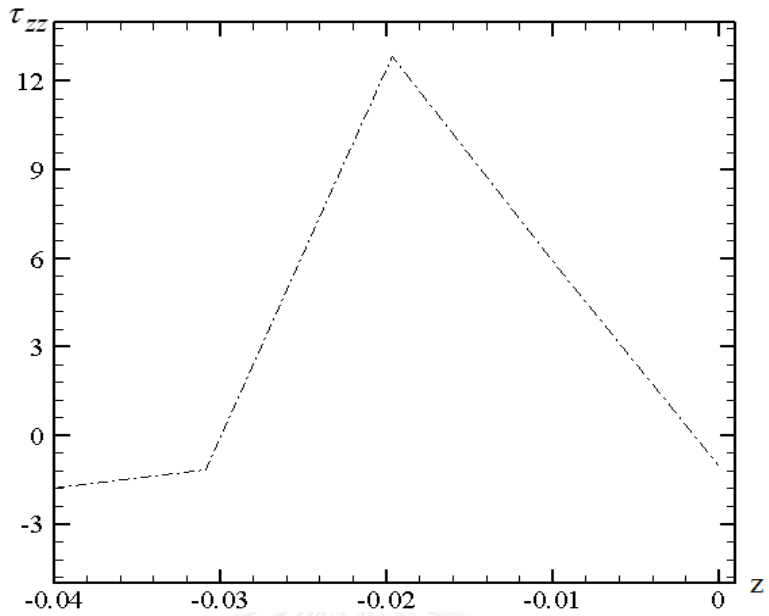

(d) $We = 2$

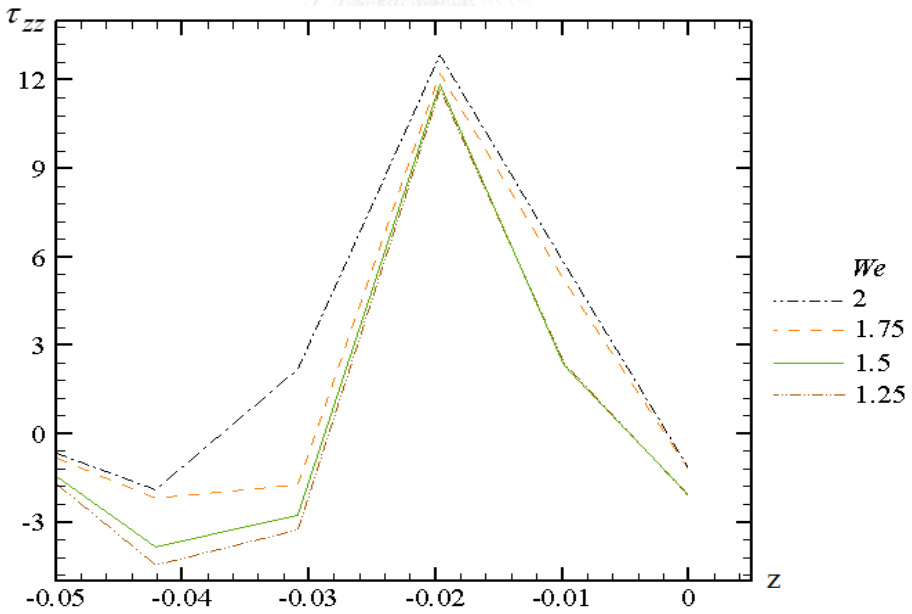

(e) $1.25 \le We \le 2$

Figure 5.15 τ_{zz} along the wall

A small negative value of radial extra-stress τ_{rr} is started at inlet and then climbed up to positive before free surface section except a small area near die exit that oscillation is appeared violently as shown in Figure 5.16. For the trend of $\tau_{\theta\theta}$ as Figure 5.17, it

displays the extreme value in the neighborhood of the singularity. A maximum pressure along the wall is illustrated at the exit die and the pressure drops to zero as in Figure 5.18.

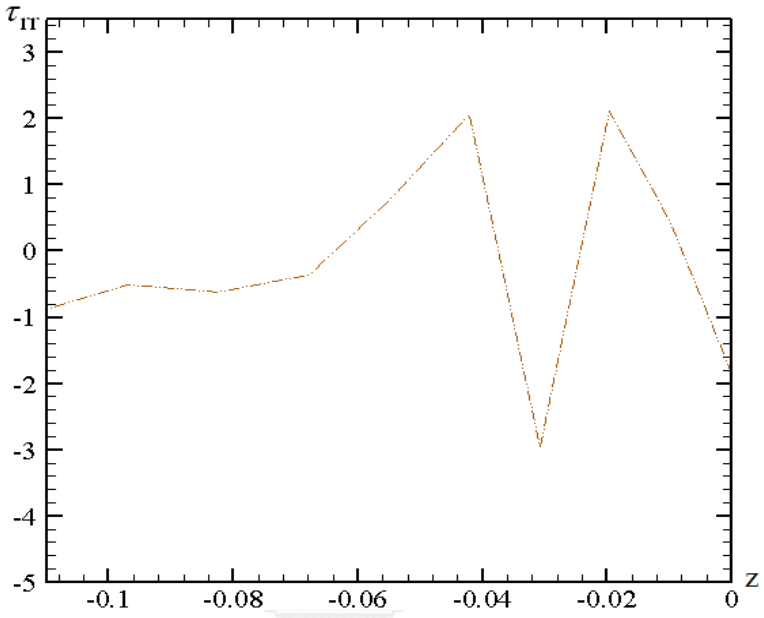

(a) *We* = 1.25

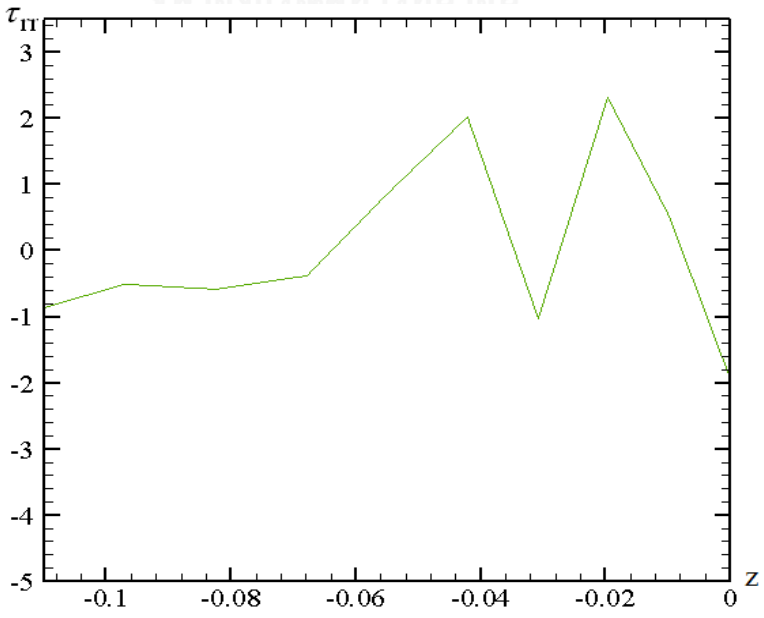

(b) *We* = 1.5

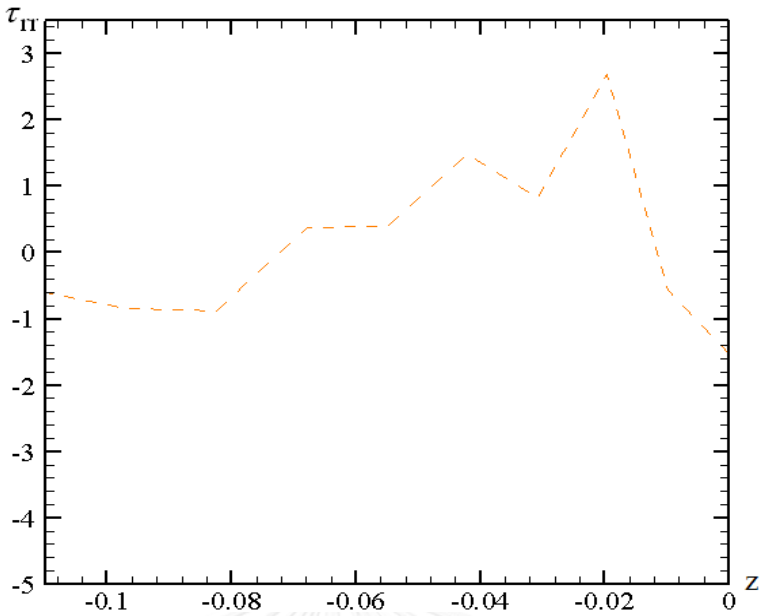
τ_{rr}
3
2
1
0
-1
-2
-3
-4
-5
-0.1
-0.08
-0.06
-0.04
-0.02
0
z

(c) *We* = 1.75

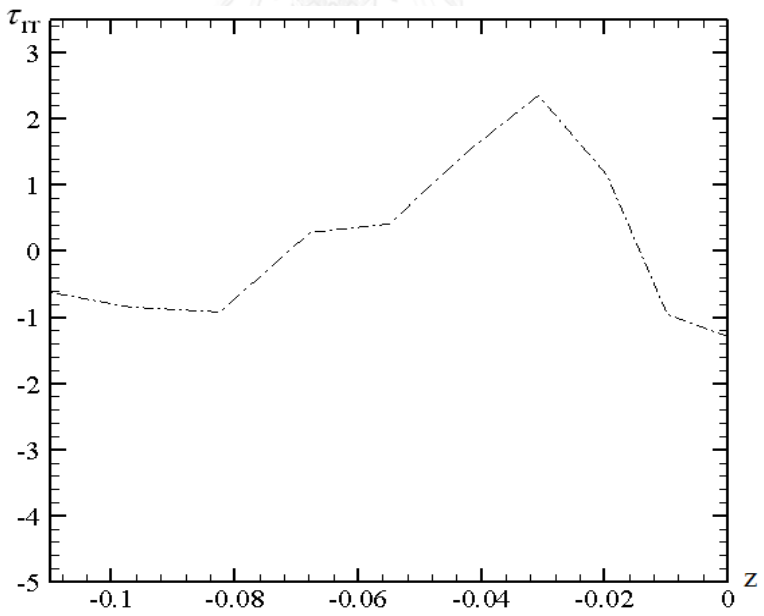
τ_{rr}
3
2
1
0
-1
-2
-3
-4
-5
-0.1
-0.08
-0.06
-0.04
-0.02
0
z

(d) *We* = 2

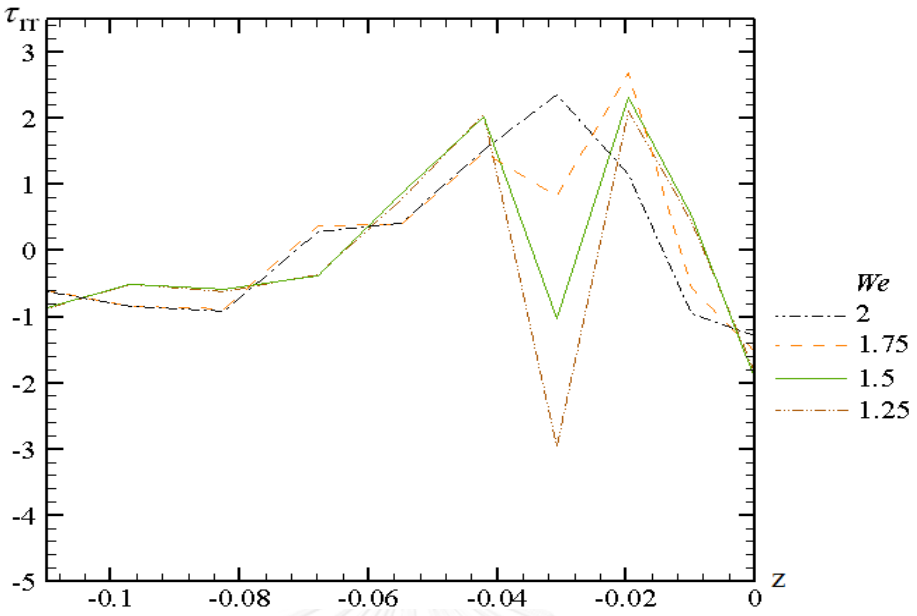

(e) $1.25 \le We \le 2$

Figure 5.16 τ_{rr} along the wall

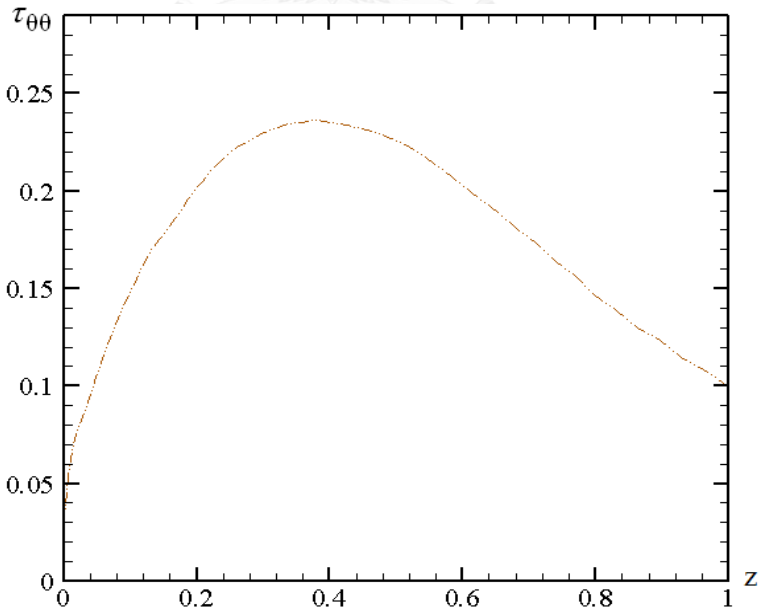

(a) *We* = 1.25

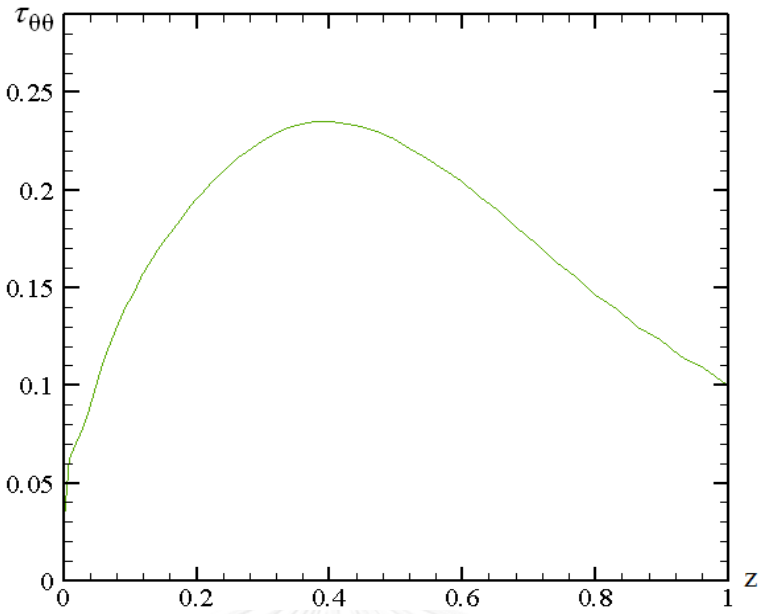

(b) *We* = 1.5

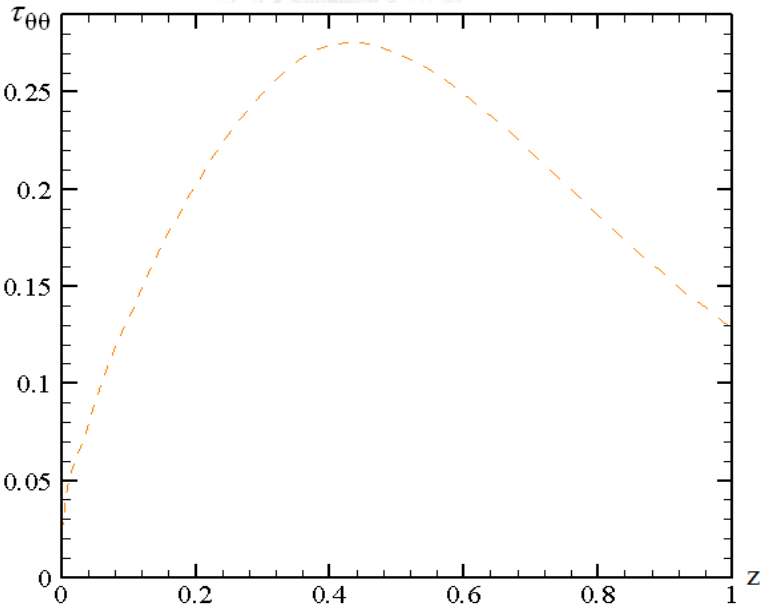

(c) *We* = 1.75

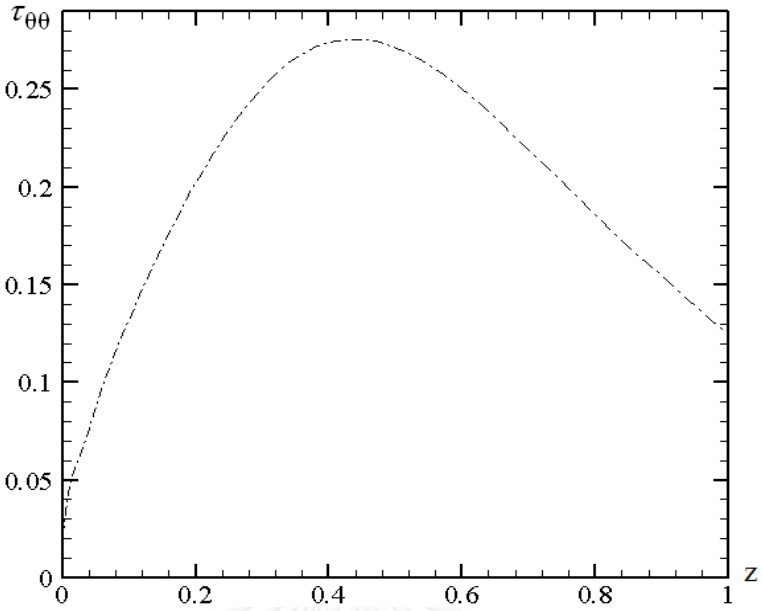

(d) $We = 2$

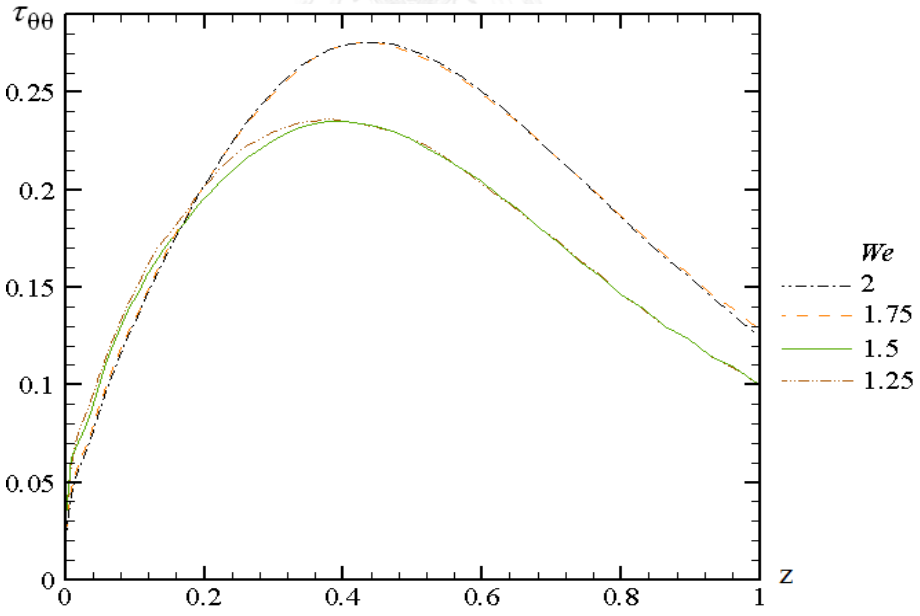

(e) $1.25 \le We \le 2$

Figure 5.17 $\tau_{\theta\theta}$ along the wall

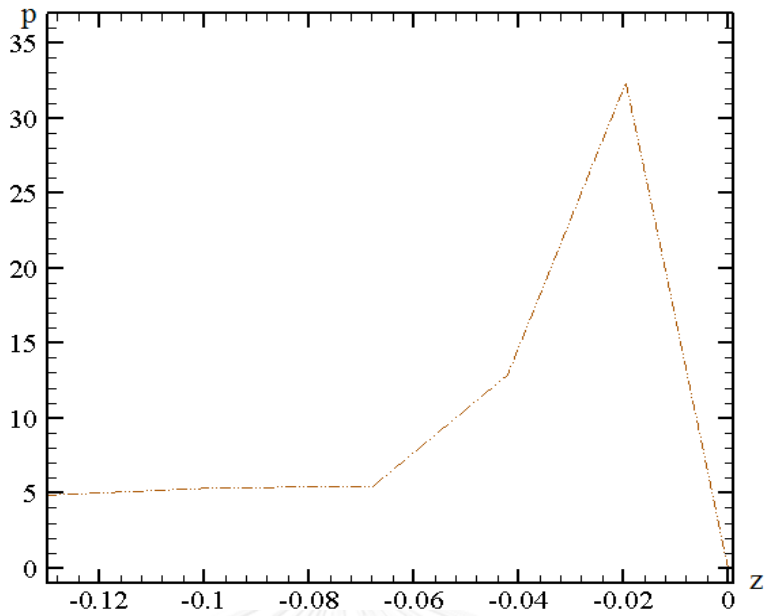

(a) *We* = 1.25

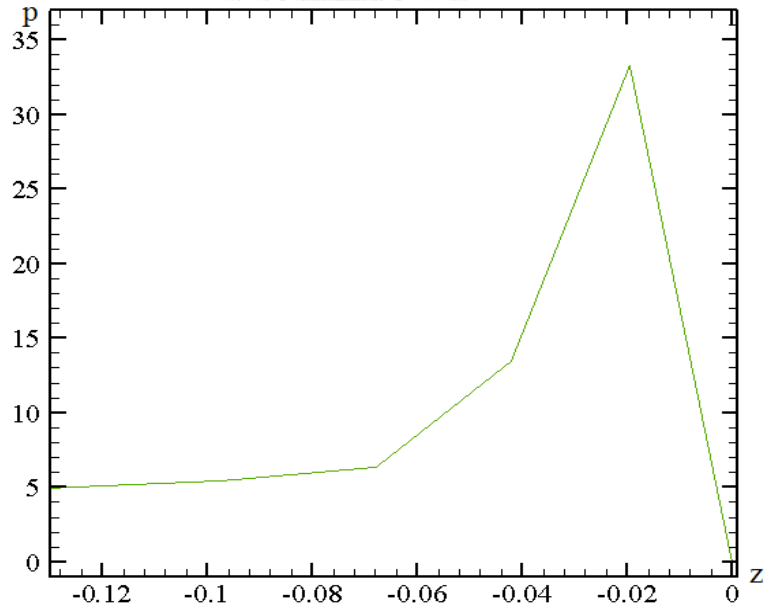

(b) *We* = 1.5

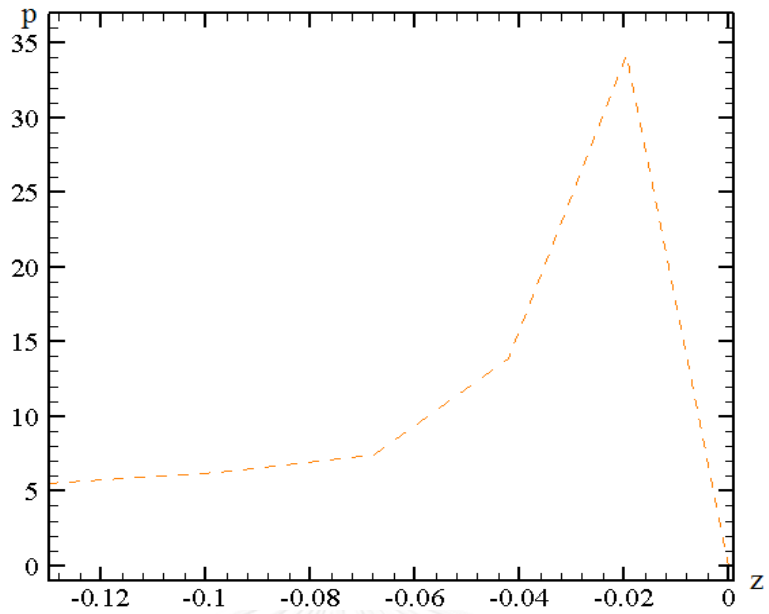
p
35
30
25
20
15
10
5
0
-0.12
-0.1
-0.08
-0.06
-0.04
-0.02
0
z

(c) *We* = 1.75

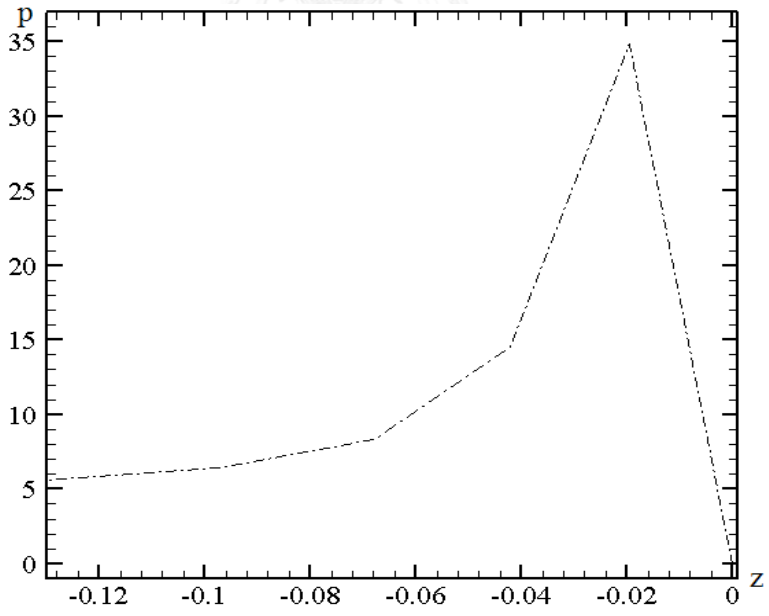
p
35
30
25
20
15
10
5
0
-0.12
-0.1
-0.08
-0.06
-0.04
-0.02
0
z

(d) *We* = 2

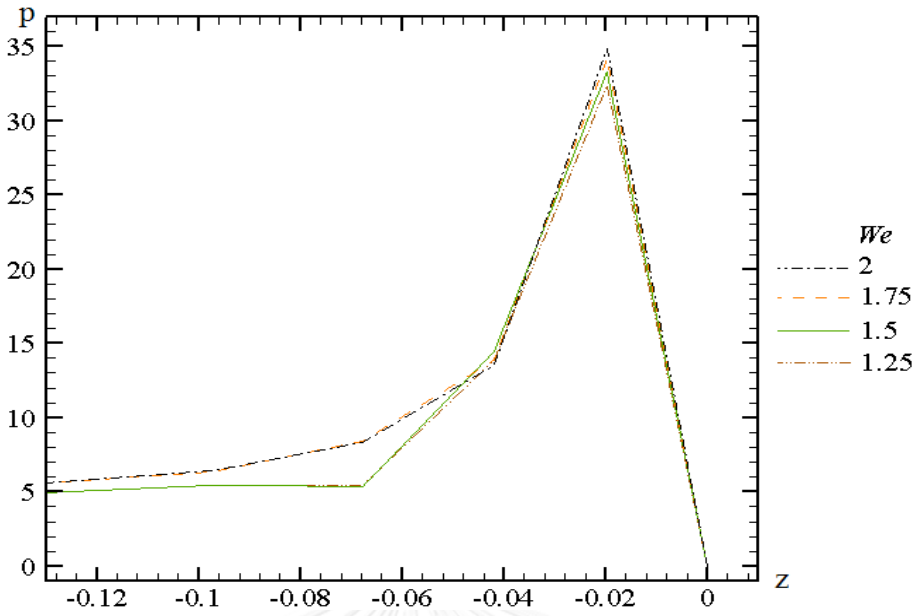

(e) $1.25 \le We \le 2$

Figure 5.18 p along the wall

To reduce the duplication of many figures, the die-swell shape with mesh pattern of highest *We* is selected to represent in Figure 5.19. The line contour of Oldroyd-B fluid at $We = 2$ is displayed with conspicuous swelling geometry. The maximum value of velocity u_z still lies on symmetry line as Figure 5.19(a) but the maximum value of u_r is located at exit point as seen in Figure 5.19(b) whilst Figure 5.19(c) demonstrates pressure contour that is supreme at entrance and vanished downstream the die region. The maxima of τ_{rz}, τ_{zz} and τ_{rr} at exit die are displayed in Figure 5.19(d) - Figure 5.19(f) respectively whilst for $\tau_{\theta\theta}$ the maxima appear at swell area as can be seen in Figure 5.19(g).

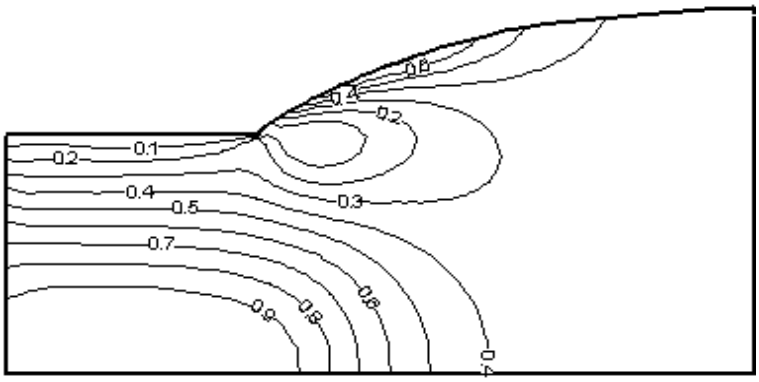

(a) u_z

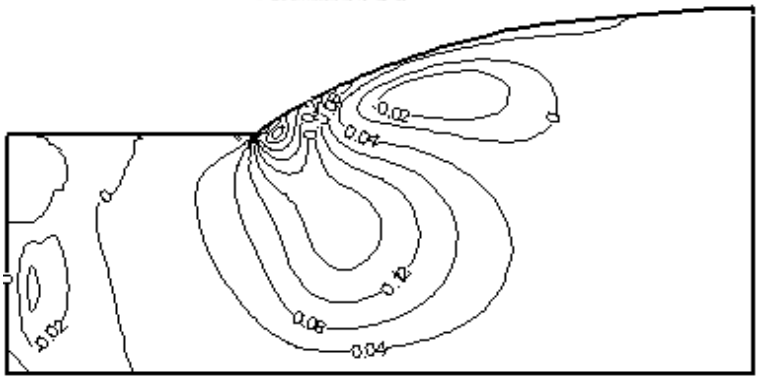

(b) u_r

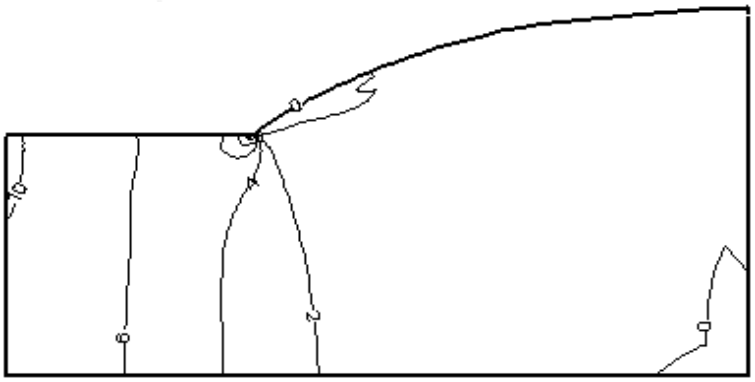

(c) p

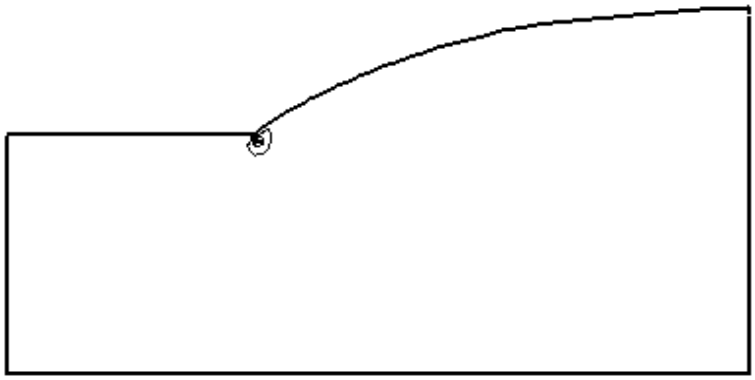

(d) τ_{rz}

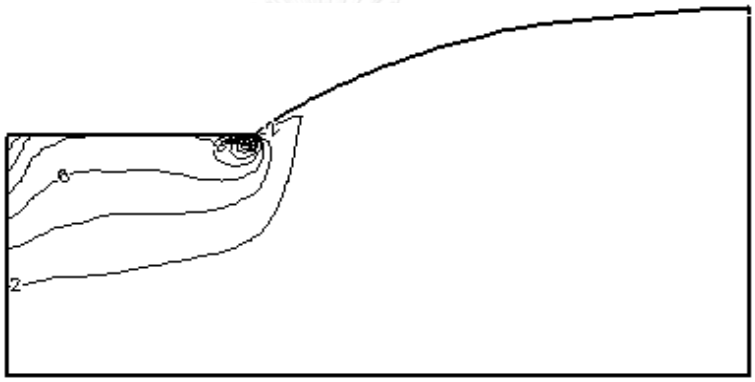

(e) τ_{zz}

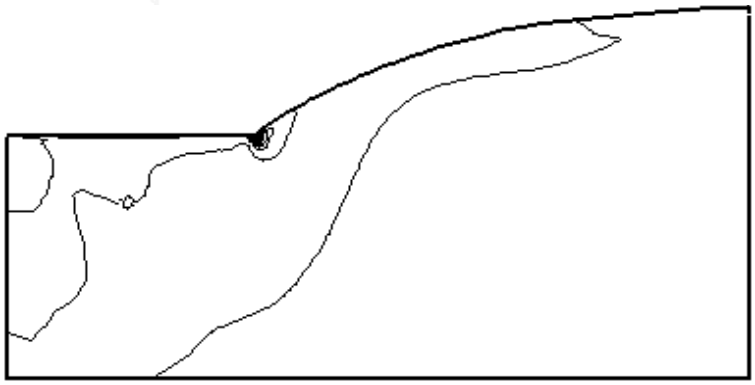

(f) τ_{rr}

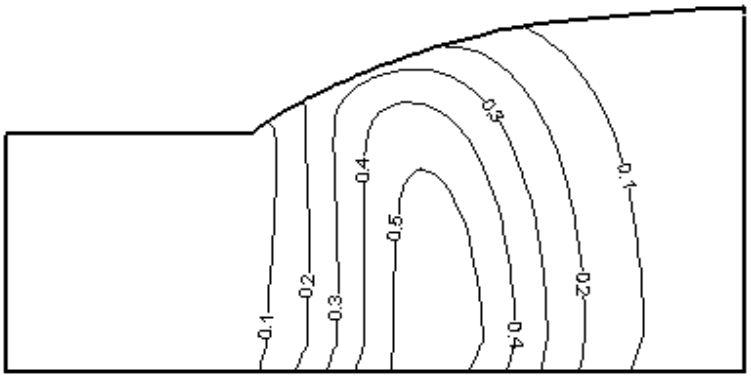

(g) $\tau_{\theta\theta}$

Figure 5.19 Line contour of Oldroyd-B fluid at *We* = 2, Die-swell problem

5.5 Conclusions

The simulation of die-swell problem was evaluated with efficiency procedure of feedback semi-implicit Taylor Galerkin finite element method whilst the algorithm without feedback can execute only half value of restricted standard Weisenberg number for Oldroyd-B fluid. By means of feedback pressure-driven velocity flow, all stresses, swelling ratios and pressures are enlarged when *We* is increased to the upper limit of two. The well solution is close to real problem that is the reason from the re-force of velocity and pressure fields at the inlet boundary in order to improve the swelling ratio that is slightly different to the theoretical prediction. The swelling line of free surface has reached steadiness faster than non-treatment method that took further time steps and its solution of fixing initial condition closely matches analytical adjustment.

CHAPTER 6
FINAL REMARKS

A semi-implicit Taylor-Galerkin method is used to simulate steady two-dimensional isothermal incompressible creeping fluid to describe flow behaviors and properties of 4:1 contraction and die-swell problems including slip velocity. The main accomplishments of this research state that the slip effect condition for Newtonian and Oldroyd-B fluids reduces the stresses of 4:1 contraction regions (sharp and rounded corner) and also die swell. The feedback of pressure-driven velocity flow scheme is properly applied with STGFEM to treat unstable and diverged solution. In addition, this treatment is efficient to adjust free surface with swelling ratio in die swell problem. These approximate solutions (velocity, stress and pressure) of complex flows are stabilized by streamline upwind Petrov-Galerkin scheme and velocity gradient recovery technique.

The 4:1 contraction problem is considered to study the behaviors of viscoelastic fluids, such as LDPE and polymer melt, since the strong elongation and violent shear stress at contraction position are exhibited apparently. The effects of increase in Weissenberg number have been illustrated via the size of vortices. In this work, STGFEM has led to the study of planar Poiseuille flows in both sharp and rounded corners. Mesh structure and refinement near contraction region significantly influenced solution accuracy. First sharp corner geometry has been considered of no-slip and slip conditions for Newtonian fluid.

Many researchers found that fluid particle move with velocity at wall. In this thesis, the slip velocity on the channel wall has been added by Phan-Thien rule which yields the result close to real solution. The peaks of the shear rate and the second invariant of the rate of strain tensor clearly appear at the severity contraction point. The slip coefficient values are varied coupled with second invariant II values in order to find the best of the slip velocity by Phan-Thien slip function. These appropriate components will decrease the stress maxima at the channel exit. The reflection of the slip condition obviously reduces the size of vortices in Newtonian fluid. In subsequent

work, switching to viscoelastic Oldroyd-B models, the slip effects of increase in Weissenberg number for Oldroyd-B models are influential in reduction of vortex size and stresses like Newtonian fluid. The comparison of slip condition against analytic solution is satisfied to shear stress values close to J&S theory.

Calculating rounded corner, the sharp corner is reshaped to curve angle at contraction. Basic STGFEM is reused to calculate rounded geometry with slip and without condition but the outcome of rounded corner failed to converge to the real solution. Feedback of pressure-driven velocity flow is employed to adjust inlet boundary condition step by step after the numerical solution is converged gradually. This technique is efficient to calculate critical levels of *We* and it also gives smooth results, unlike the oscillatory behavior of viscoelastic model that causes sharkskin phenomena and the crack of polymer product. After feedback of pressure-driven velocity flow scheme treats with STGFEM, the numerical solution will converge to possible result of Newtonian and Oldroyd-B models. In slip case, the outcomes of no-slip condition will lead the trial parameter to choose the proper slip velocity by Phan-Thien slip rule, like sharp corner. Comparison between geometries (shape and rounded corners) for 4:1 contraction flow revealed that the influence of slip effect is decreasing stresses and vortex sizes.

Die-swell flow is a common phenomenon in polymer extrusion that a fluid is compressed by entrance into a die and then a partial recovery back to the former shape and volume of fluid when fluid passes die exit. In this work Weissenberg number is representative in elastic property (especially relaxation time) that high levels of *We* affects the size of the swelling shape. Poiseuille axisymmetric die swell flows are considered to study the swelling at free surface. In case of die swell the divergence of the numerical result of Oldroyd-B model is eliminated by feedback of pressure-driven velocity flow technique the same as 4:1 planar contraction flow.

Stick-slip flows are still an important factor to deal with for die-swell because the numerical solution of Stick-slip flow has been let to the trial parameters (velocity, stress and pressure) of die swell flows. Stick-slip flow is firstly studied under an axisymmetric frame of Poiseuille flows in Newtonian and Oldroyd-B fluids. It is

found that stick-slip flows at high ($We > 1$) are difficult to calculate the approximate converge solution. The STGFEM with feedback of pressure-driven velocity flow is utilized as apparatus to solve these flows.

For predicting the swelling, the proper free surface method has been considered to get the right swelling for viscoelastic flows from dies. The solution of stick-slip flow is employed to calculate the swelling ratio of die-swell flow. Due to the fact that the growth of Weissenberg number for Oldroyd-B model effects to the reduction of pressure drop and the increase of swelling ratio, die-swell flow is hard to adjust free surface region. Feedback of pressure-driven velocity flow technique will operate this problem by increasing time stepping and changing inlet boundary as same as stick-slip case. Consequently, these streamline upwind Petrov-Galerkin scheme and velocity gradient recovery technique are provided to encounter unstable solution to approaching to the right result of high *We* ($We > 1$).

The solutions of Newtonian and Oldroyd-B fluids by solving STGFEM with feedback of pressure-driven velocity flow technique are close with theoretical and analytical results. Feedback of pressure-driven velocity flow technique is used to find appropriated inlet initial boundary. This scheme is efficient to compute on planar and axisymmetric systems. In addition, it is achievable to adjust flow gradually until steady state and also the outcome satisfy when compared against the theory and other simulation results.

In the area of fluid dynamic flows, future prolific ways of research may state the following aspects:

-Improvement of numerical solver as FEM to hybrid FV/FEM to reduce a great number of computer times that occurs in complex flows and domains.

-Three-dimensional (3D) flow simulation that is extended from two-dimensional flows to close the real problem.

-Transient flow can be monitoring velocity and pressure that change all time until the system is steady state.

-Variation of viscoelastic models, such as Phan-Thien/Tanner (PTT) and Pom Pom models in contraction and die-swell problems.

-Non-isothermal modeling by incorporating energy equation in governing equations of fluid flows because heating affects the viscosity and stresses.

-Biological Engineering field, such as blood flow and cardiovascular. That is important to understand human life and make diagnosis of disease.

Chapters four and five of this thesis form the basis of journal publications in press to appear in the International Journal under the respective titles:

“ Simulation of slip effects with 4:1 contraction flow for Oldroyd-B fluid ”, N. Thongjub, B. Puangkird and V. Ngamaramvaranggul [34].

“ Slip Effect Study of 4:1 Contraction Flow with Rounded Corner Geometry for Newtonian Fluid ”, N. Thongjub, B. Puangkird and V. Ngamaramvaranggul [35].

“ Newtonian fluid through the abrupt 4:1 contraction flow of rounded corner geometry with feedback pressure-driven velocity flow ” , V. Ngamaramvaranggul and N. Thongjub [28].

“ Simulation of die swell flow for Oldroyd-B model with feedback semi-implicit Taylor Galerkin finite element Method ”, N. Thongjub and V. Ngamaramvaranggul [99].

REFERENCES

1. Hinton, E. and D.R.J. Owen, *An introduction to finite element computations*. 1979, Swansea, UK: Pineridge Press.
2. Daily, J.W. and D.R.F. Harleman, *Fluid dynamics*. 1966: Addison-Wesley Publishing Company, Inc.
3. Paddon, D. and H. Holstein, *Technical report.*, 1980: New York.
4. Bathe, K.J., *Finite element procedures*. 1996, New Jersey: Prentice-Hall, Inc.
5. Chandrupatla, T.R. and A.D. Belegundu, *Introduction to finite elements in engineering*, ed. 4. 2011: Prentice Hall.
6. Crochet, M.J. and R. Keunings, *Die swell of a Maxwell fluid : Numerical prediction.* J. Non-Newtonian Fluid Mech., 1980. **7**: p. 199-212.
7. Reddy, J.N., *An introduction to the finite element method*. 1984, New York: McGraw-Hill.
8. Aboubacar, M. and M.F. Webster, *A cell-vertex finite volume/element method on triangles for abrupt contraction viscoelastic flows.* J. Non-Newtonian Fluid Mech., 2001. **98**: p. 83-106.
9. Phillips, T.N. and A.J. Williams, *Viscoelastic flow through a planar contraction using a semi-Lagrangian finite volume method.* J. Non-Newtonian Fluid Mech., 1999. **87**: p. 215-246.
10. Phillips, T.N. and A.J. Williams, *Comparison of creeping and inertial flow of an Oldroyd B fluid through planar and axisymmetric contractions.* J. Non-Newtonian Fluid Mech., 2002. **108**: p. 25-47.
11. Ngamaramvaranggul, V., *Numerical simulation of non-Newtonian free surface flows*, 2000, University of Wales Swansea.
12. Ngamaramvaranggul, V. and M.F. Webster, *Simulation of pressure-tooling wire-coating flow with Phan-Thien/Tanner models.* Int. J. Num. Meth. Fluids., 2002. **38**: p. 677-710.
13. Puangkird, B., *Numerical simulations of complex viscoelastic flows*, 2007, Swansea University.
14. Puangkird, B., F. Belblidia, and M.F. Webster, *Numerical simulation of viscoelastic fluids in cross-slot devices.* 2009. **162**: p. 1-20.
15. Afonso, A., et al., *The log-conformation tensor approach in the finite-volume method framework.* J. Non-Newtonian Fluid Mech., 2009. **157**: p. 55-65.
16. Fattal, R. and R. Kupferman, *Constitutive laws for the matrix-logarithm of the conformation tensor.* J. Non-Newtonian Fluid Mech., 2004. **123**: p. 281-285.
17. Kwon, K., *Finite element analysis of planar 4:1 contraction flow with the tensor-logarithmic formulation of differential constitutive equations.* Korea-Australia Rheology Journal., 2004. **16**(4): p. 183-191.

18. Evans, R.E. and K. Walters, *Flow characteristics associated with abrupt changes in geometry in the case of highly elastic liquids.* J. Non-Newtonian Fluid Mech., 1986. **20**: p. 11-29.

19. Walters, K. and D.M. Rawlinson, *On some contraction flows for Boger fluids.* Rheol. Acta., 1982. **21**: p. 547-522.

20. Boger, D.V., *Viscoelastic flows through contractions.* Ann. Rev. Fluid Mech., 1987. **19**: p. 157-182.

21. Evans, R.E. and K. Walters, *Further remarks on the lip-vortex mechanism of vortex enhancement in planar-contraction flows.* J. Non-Newtonian Fluid Mech., 1989. **32**: p. 95-105.

22. Rothstein, J.P. and G.H. McKinley, *A comparison of the stress and birefringence growth of dilute semi-dilute and concentrated polymer solutions in uniaxial extensional flows.* J. Non-Newtonian Fluid Mech., 2002. **108**: p. 275-290.

23. Alves, M.A., P.J. Oliverira, and F.T. Pinho, *Numerical simulation of viscoelastic contraction flows*, in *Second MIT Conference on Computational Fluid and Solid Mechanics*2003.

24. Alves, M.A., P.J. Oliverira, and F.T. Pinho, *Benchmark solutions for the flow of Oldroyd-B and PTT fluids in planar contractions.* J. Non-Newtonian Fluid Mech., 2003. **110**: p. 45-75.

25. Alves, M.A., et al. *Visualization studies of viscoelastic flow in a 4:1 square/square contraction*. in *COBEM*. 2003.

26. Alves, M.A., et al. *Viscoelastic flow in axisymmetric contractions : The effect of contraction ratio*. in *the 10th Brazilian Congress of Thermal Sciences and Engineering*. 2004.

27. Alves, M.A., et al., *On the effect of contraction ratio in viscoelastic flow through abrupt contractions.* J. Non-Newtonian Fluid Mech., 2004. **122**: p. 117-130.

28. Ngamaramvaranggul, V. and N. Thongjub, *Newtonian fluid through the abrupt 4:1 contraction flow of rounded corner geometry with feedback pressure-driven velocity flow*. Int. J. Inf. Tech. Comp. Sc., 2014. **15**(2): p. 1-10.

29. Silliman, W.J. and L.E. Scriven, *Separating flow near a static contact Line : Slip at a wall and shape of a free surface.* J. Comp. Phys., 1980. **34**: p. 287-313.

30. Ramamurthy, A.V., *Wall slip in viscous fluids and influence of materials of construction.* J. Rheol., 1986. **30**: p. 337-357.

31. Jiang, T.Q. and A.C. Young, *The rheological characterization of HPG gels : Measurement of slip velocities in capillary tubes.* Rheol. Acta., 1986. **25**: p. 397-404.

32. Phan-Thien, N., *Influence of wall slip on extrudate swell : A boundary element investigation.* J. Non-Newtonian Fluid Mech., 1988. **26**: p. 327-340.

33. Ngamaramvaranggul, V. and M.F. Webster, *Simulation of coating flows with slip effects.* Int. J. Num. Meth. Fluids., 2000. **33**: p. 961-992.

34. Thongjub, N., B. Puangkird, and V. Ngamaramvaranggul, *Simulation of slip effects with 4:1 contraction flow for Oldroyd-B fluid.* AIJSTPME., 2013. **6**(3): p. 19-28.

35. Thongjub, N., B. Puangkird, and V. Ngamaramvaranggul, *Slip effect study of 4:1 contraction flow with rounded corner geometry for Newtonian fluid.* TIJSAT., 2015. **20**(2).

36. Richardson, S., *A stick-slip problem related to the motion of a free jet at low Reynolds numbers.* Proc. Camb. Phil., 1970. **67**: p. 477-489.

37. Georgiou, G.C., et al., *A singular finite element for Stokes flow : The stick-slip problem.* Int. J. Num. Meth. Fluids., 1989. **9**: p. 1353-1367.

38. Georgiou, G.C., L.G. Olson, and W.W. Schultz, *The integrated singular basis function method for the stick-slip and the die-swell problems.* Int. J. Num. Meth. Fluids., 1991. **13**: p. 1251-1265.

39. Vlachopoulos, J., M. Horie, and S. Lidorikis, *An evaluation of expressions prediction die swell.* Trans. Soc. Rheol., 1972. **16**(4): p. 669-685.

40. Okabe, M., *Fundamental theory of the semi-radial singularity mapping with applications to fracture mechanics.* Comp. Meth. App. Mech. Eng., 1981. **26**: p. 53-73.

41. Tanner, R.I., *Engineering rheology*. 1985, London: Oxford University Press.

42. Ingham, D.B. and M.A. Kelmanson, *Boundary integral equation analyses of singular potential and biharmonic problems*. Springer-Verlag. 1984, Berlin.

43. Cuvelier, C., A. Segal, and A.A. vanSteenhoven, *Finite element methods and Navier-Stokes equations*. 1986, Holland: D. Reidel Publishing Company.

44. Nickell, R.E., R.I. Tanner, and B. Caswell, *The solution of viscous incompressible jet and free surface flows using finite elements.* J. Fluid Mech., 1974. **65**: p. 189-206.

45. Chang, P.W., T.W. Patten, and B.A. Finlayson, *Collocation and Galerkin finite element methods for viscoelastic fluid flow-II.* Comp. and Fluids, 1979. **7**: p. 285-293.

46. Butler, C.W. and M.B. Bush, *Extrudate swell in some dilute elastic solutions.* Rheol. Acta., 1989. **28**: p. 294-301.

47. Baloch, A., P. Townsend, and M.F. Webster, *On two- and three-dimensional expansion flows.* Comp. and Fluids, 1995. **24**: p. 863-882.

48. Karagiannis, A., A.N. Hrymak, and J. Vlachopoulos, *Three-dimensional non-isothermal extrusion flows.* Rheol. Acta., 1989. **28**: p. 121-133.

49. Beverly, C.R. and R.I. Tanner, *Numerical analysis of three-dimensional Newtonian extrudate swell.* Rheol. Acta., 1991. **30**: p. 341-356.

50. Ahmed, R., R.F. Liang, and M.R. Mackley, *The experimental observation and numerical prediction of planar entry flow and die swell for molten polyethylenes.* J. Non-Newtonian Fluid Mech., 1995. **59**: p. 129-153.

51. Hooke, R., *A description of helioscopes and some other instruments*. 1676, London.

52. Maxwell, J.C., *On the dynamical theory of gases.* Phil. Trans. Roy. Soc., 1967. **157**: p. 49-89.

53. Maxwell, J.C., *A treatise on electricity and magnetism*. 1973, New York.

54. Newton, I., *Philosophiae naturlis principia mathematica*, ed. F. Caori. Vol. 1. 1962, Berkerley and Los Angels: University of California Press.

55. Oldroyd, J.G., *On the formulation of rheological equation of state.* Proc. Roy. Soc., 1950. **200**: p. 523-541.

56. Crochet, M.J. and R. Keunings, *Finite element analysis of die swell of a highly elastic fluid.* J. Non-Newtonian Fluid Mech., 1982. **10**: p. 339-356.

57. Phan-Thien, N., *A non-linear network viscoelastic model.* J. Rheol., 1978. **22**(3): p. 259-283.

58. Phan-Thien, N. and R.I. Tanner, *A new constitutive equation derived from network theory.* J. Non-Newtonian Fluid Mech., 1977. **2**: p. 353-365.

59. Barnes, H.A., *A handbook of elementary rheology*. 2000, UK: University of Wales.

60. Han, C.D., *Rheology in polymer processing*. 1976, New York: Academic press.

61. Bird, R.B., R.C. Armstrong, and O. Hassager, *Dynamics of polymeric liquids: Fluid mechanics*. Vol. 1. 1987, New York: John Wiley & Sons.

62. Morrison, F.A., *Understanding rheology*. 2001, NewYork: Oxford University Press, Inc.

63. Reiner, M., *A mathematical theory of dilatancy.* Amer. J. Math., 1945. **67**: p. 350-362.

64. Rivlin, R.S., *The hydrodynamics of non-Newtonian fluids, I.* Proc. Roy. Soc., 1948. **193**: p. 260-281.

65. Lamb, H., *Hydrodynamics*, ed. 6. 1932: Cambridge University Press.

66. Batchelor, G.K., *An introduction to fluid dynamics*. 1967: Cambridge University Press.

67. Ngamaramvaranggul, V. and M.F. Webster, *Viscoelastic simulation of stick-slip and die swell flows.* Int. J. Num. Meth. Fluids, 2001. **36**: p. 539-595.

68. Belblidia, F., et al., *Alternative subcell discretisations for viscoelastic flow : Stress interpolation.* J. Non-Newtonian Fluid Mech., 2007. **146**: p. 59-78.

69. Keshtibana, I.J., et al., *Generalised approach for transient computation of start-up pressure-driven viscoelastic flow.* J. Non-Newtonian Fluid Mech., 2008. **151**: p. 2-20.

70. Baker, A.J., *Finite element computational fluid mechnics*. 1985: McGraw-Hill.

71. Burnett, D.S., *Finite element analysis from concepts to applications*. 1988, Reading, MA.

72. Baaijens, F.P.T., *Numerical analysis of unsteady viscoelastic flow.* Comp. Meth. App. Mech. Eng., 1992. **94**: p. 285-299.

73. Carew, E.O., P. Townsend, and M.F. Webster, *A Taylor-Petrov-Galerkin algorithm for viscoelastic flow.* J. Non-Newtonian Fluid Mech., 1993. **50**: p. 253-287.

74. Pearson, J.R.A. and S.M. Richardson, *Computational analysis of polymer processing*. 1983: Applied Science Publishers Ltd.

75. Brooks, A.N. and T.J.R. Hughes, *Streamline upwind/Petrov-Galerkin formulations for convection dominated flows with particular emphasis on the incompressible Navier-stokes equation.* Comp. Meth. App. Mech. Eng., 1982. **32**: p. 199-259.

76. Luo, X.L. and M.J. Tanner, *A decoupled finite-element streamline-upwind scheme for viscoelastic flow problems.* J. Non-Newtonian Fluid Mech., 1989. **31**: p. 143-162.

77. Marchal, J.M. and M.J. Crochet, *A new mixed finite element for calculating viscoelastic flow.* J. Non-Newtonian Fluid Mech., 1987. **26**: p. 77-114.

78. Mendelson, M.A., et al., *Approximation error in finite element calculation of viscoelastic fluid flows.* J. Non-Newtonian Fluid Mech., 1982. **10**: p. 31-54.

79. Matallah, H., *Numerical simulation of viscoelastic flows*, 1998, University of Wales: Swansea.

80. Burden, R.L. and J.D. Faires, *Numerical analysis*. 1985, Boston: Prindle, Weber & Schmidt.

81. Gresho, P.M., et al., *The comsistent Galerkin FEM for computing derived boundary quantities in thermal and-or fluids problems.* International Journal for Numerical Methods in Fluids, 1987. **7**: p. 371-394.

82. Hawken, D.M., P. Townsend, and M.F. Webster, *A comparison of gradient recovery methods in finite-element calculations.* Communications in Applied Numerical Method, 1991. **7**: p. 195-204.

83. H. Matallah, P.T., M.F. Webster, *Recovery and stress-splitting schemes for viscoelastic flows.* J. Non-Newtonian Fluid Mech., 1998. **75**: p. 139-166.

84. Levine, N., *Stress sampling poins for linear in triangles the finite element method*, in *Num. Anal. Rep.*1982, University of Reading.

85. Levine, N., *Superconvergent estimation of the gradients from finite element approximation of triangle elements*, 1985, University of Reading.

86. Christie, I., et al., *Finite element methods for second-order differential equations with significant first derivatives.* Int. J. Num. Meth. Eng., 1976. **10**(6): p. 1389-1396.

87. Henrich, J.C., et al., *An upwind finite element scheme for two-dimensional convective transport equation.* Int. J. Num. Meth. Eng., 1977. **11**: p. 134-143.

88. Crochet, M.J., A.R. Davies, and K. Walters, *Numerical simulation of non-Newtonian fluid flow*. 1984: Elsevier.

89. Tanner, R.I., *A theory of die-swell.* J. Polymer. Sci. Part A-2: Polymer Physics, 1970. **8**(12): p. 2067-2078.

90. Johnson, M.W. and D. Segalman, *A model for viscoelastic fluid behavior which allows non-affine deformation.* J. Non-Newtonian Fluid Mech., 1977. **2**: p. 255-270.

91. Boger, D.V. and A.V. Ramamurthy, *Flow of viscoelastic fluids through an abrupt contraction.* Rheol. Acta., 1972. **11**: p. 61-69.

92. Boger, D.V. and M.M. Denn, *Capillary and slit methods of normal stress measurements.* J. Non-Newtonian Fluid Mech., 1980. **6**: p. 163-185.

93. Aboubacar, M., H. Matallah, and M.F. Webster, *Highly elastic solutions for Oldroyd-B and Phan-Thien/Tanner fluids with a finite volume/element method : planar contraction flows.* J. Non-Newtonian Fluid Mech., 2002. **103**: p. 65-103.

94. Ngamaramvaranggul, V. and S. Thenissara, *The contraction point for Phan-Thien/Tanner model of tube-tooling wire-coating flow.* Int. J Math. Comp Phys Quan. Eng., 2010. **4**(4): p. 627-631.

95. Larson, M.G. and F. Bengzon, *The finite element method : Theory, implementation, and application*. Vol. 10. 2013: Springer Berlin Heidelberg.

96. Zienkiewicz, O.C., R.L. Taylor, and J.Z. Zhu, *The finite element method : Its basis and fundamentals*. 7 ed. 2013: Butterworth-Heinemann.

97. Caswell, B. and M. Viriyayuthakorn, *Finite element simulation of die swell for a maxwell fluid.* J. Non-Newtonian Fluid Mech., 1983. **12**: p. 13-29.

98. Clermont, J.R. and M. Normadin, *Numerical simulation of extrudate swell for Oldroyd-B fluid using the stream-tube analysis and a streamline approximation.* J. Non-Newtonian Fluid Mech., 1993. **50**: p. 193-215.

99. Thongjub, N. and V. Ngamaramvaranggul, *Simulation of die swell flow for Oldroyd-B model with feedback semi-implicit Taylor Galerkin finite element Method.* KMUTNB Int J Appl Sci Technol., 2015. **8**(1): p. 55-63.

VITA

Name	Miss Nawalax Thongjub
Place of Birth	Samutsongkhram, Thailand
Education	B.Sc.(Mathematics) Thammasat University, 2000
	M.Sc.(Computational Science), Chulalongkorn University, 2003
Scholarship	National Science and Technology Development Agency (NSTDA)